DISSERTATION

Deterministic and robust optimization of complex nanoscale photonic structures

ausgeführt zum Zwecke der Erlangung des akademischen Grades
eines Doktors der technischen Wissenschaften unter der Leitung von

Associate Prof. Dipl.-Ing. Dr. techn. Clemens Heitzinger
E101 – Institut für Analysis und Scientific Computing, TU Wien

eingereicht an der Technischen Universität Wien
Fakultät für Mathematik und Geoinformation

von

Boaz Blankrot, M.Sc.
Matrikelnummer: 1635842

Diese Dissertation haben begutachtet:

1. **Prof. Dr. Clemens Heitzinger**
   Institut für Analysis und Scientific Computing, TU Wien
2. **Prof. Dr. Henri Benisty**
   Institut d'Optique, Université Paris-Saclay
3. **Prof. Dr. Steven G. Johnson**
   Massachusetts Institute of Technology

Wien, am 10.09.2020

Kurzfassung

Dank ihrer vielseitigen Fähigkeiten zur Lichtmanipulation sind photonische Strukturen in einer Vielzahl von Bereichen wie optische Datenverarbeitung, Bildgebung und Tarnung vielversprechend. Das optische Verhalten dieser Strukturen ist das Ergebnis komplexer Wechselwirkungen zwischen vielen Variablen, was eine bedeutende Hürde bei der Suche nach optimalen Designs darstellt. In dieser Arbeit ist es unser Ziel, einen automatisierten Ansatz für die nominelle und robuste Optimierung einer großen Klasse zusammengesetzter photonischer Strukturen bereitzustellen. Die Dissertation ist kumulativ und besteht aus fünf veröffentlichten oder eingereichten Arbeiten.

Die erste Arbeit (Chapter 2) enthält das Rückgrat unseres Ansatzes. Wir beginnen mit der Spezifizierung des schnellen elektromagnetischen Lösers, der zur Modellierung einer gegebenen Struktur verwendet wird, welcher die Diskretisierung von Integralgleichungen für jeden Einschluss, die Mehrfachstreutheorie zur Berechnung von Einschlusswechselwirkungen und die Fast-Multipole-Method zur Beschleunigung des Lösers kombiniert. Dann werden die Parameter jedes Einschlusses mit einer gradientenbasierten Methode optimiert, wobei der Gradient mit der adjungierten Methode berechnet wird. Wir demonstrieren unsere Methode, indem wir zwei Strukturen entwerfen, die die Feldintensität an gegebenen Punkten maximieren. Die resultierenden Designs waren auffallend unregelmäßig, was den Einsatz der Optimierung unterstützt.

Wir veröffentlichten den Julia-Quellcode, der zur Ausführung unserer Simulationen verwendet wurde, als Open-Source-Forschungssoftwarepaket mit einem begleitenden Software-Journal-Papier (Chapter 3). Dieses Paket bietet den Benutzern die Möglichkeit, die in Chapter 2 besprochene Klasse von Problemen zu lösen und zu optimieren. Nach der Veröffentlichung wurde die Software erweitert, um die in späteren Kapiteln behandelten Probleme zu unterstützen. Das Konferenzpapier in Chapter 4 erweitert die Optimierung auf Mehrfrequenzprobleme und stellt einen vorläufigen Ansatz für den Entwurf von Demultiplexern auf der Basis photonischer Kristalle vor.

Unser vierter Beitrag (Chapter 5) verallgemeinert die Zielfunktionen in unserem Ansatz, um den Leistungsfluss einzubeziehen und so die Optimierung von praktischen Strukturen zu ermöglichen, deren Verhalten nicht allein durch die punktweise Feldstärke spezifiziert werden kann. Mit dieser Möglichkeit waren wir in der Lage, ein bestehendes Zweifrequenz-Demultiplexer-Design zu verbessern und eine Struktur zu entwerfen, die eine erhebliche asymmetrische Lichtdurchlässigkeit aufweist, die auch als optische Diode bekannt ist.

Während unserer Arbeit stellten wir fest, dass viele dieser optimierten Bauelemente empfindlich auf Änderungen der Parameter reagieren, was sie in der Praxis, wo Herstellungsfehler zu erwarten sind, unwirksam machen. Diese Erkenntnis motivierte uns zur Aufnahme von zwei robusten Optimierungsstrategien in unseren Ansatz (Chapter 6), so dass die resultierenden Designs auch bei Vorhandensein solcher Fehler weiterhin funktionieren würden. Insbesondere entwarfen wir photonische Strukturen, die, selbst bei unabhängigen zufälligen

Störungen an jedem Stabradius, eine asymmetrische Lichtdurchlässigkeit aufwiesen.

Abstract

Thanks to their versatile light-manipulation abilities, photonic structures show considerable promise in a variety of fields such as optical computing, imaging, and cloaking. The optical behaviors of these structures are a result of complex interactions between many variables, which poses a significant hurdle to finding optimal designs. In this work, our goal is to provide an automated approach for the nominal and robust optimization of a large class of composite photonic structures. The thesis is cumulative and consists of five published or submitted papers.

The first paper (Chapter 2) contains the backbone of our approach. We begin by specifying the fast electromagnetic solver used to model a given structure, which combines integral equation discretization for each inclusion, multiple scattering theory to compute inclusion interactions, and the Fast Multipole Method in order to accelerate the solver. Then, the parameters of each inclusion are optimized with a gradient-based method, where the gradient is calculated by the adjoint-state method. We demonstrate our method by designing two structures that maximized the intensity of the electric field at given points. The resulting designs were noticeably irregular, which supports the use of optimization.

We published the Julia source code used to run our simulations as an open-source research software package with an accompanying software journal paper (Chapter 3). This package provides users with the ability to solve and optimize the class of problems discussed in Chapter 2. After publication, the software was expanded to support problems discussed in later chapters. The conference paper in Chapter 4 extends the optimization to multi-frequency problems, and presents a preliminary approach for designing photonic crystal-based demultiplexers.

Our fourth paper (Chapter 5) generalizes the objective functions in our approach to include power flow, thus enabling optimization of practical structures whose behavior cannot be specified solely by pointwise field amplitude. With this capability, we were able to improve upon an existing two-frequency demultiplexer design as well as design a structure that exhibits substantial asymmetric light transmission, which is also known as an optical diode.

During our work, we noticed that many of these optimized devices are sensitive to changes in the parameters, rendering them ineffective in practice, where fabrication errors are to be expected. This realization motivated the incorporation of two robust optimization strategies into our approach (Chapter 6), such that resulting designs would continue to perform in the presence of such errors. Specifically, we designed photonic structures that exhibited asymmetric light transmission even with independent random perturbations applied to each rod radius.

Acknowledgments

First and foremost, I would like to express my gratitude to my advisor, Prof. Clemens Heitzinger, for his excellent guidance over the past 4 years. Without his support, knowledge, and feedback, this PhD would not have been achievable. I would also like to acknowledge the generous support of the Austrian Science Fund (FWF) under the START Prize, Project Y660 *PDE Models for Nanotechnology*.

Additionally, I want to thank Prof. Henri Benisty and Prof. Steven G. Johnson for serving on my dissertation committee, and for their valuable feedback on this work.

Special thanks go to Ms. Ursula Schweigler for going out of her way to help me navigate TU Wien bureaucracy, and for being a constant source of solid advice. I am also grateful to all those who made me feel at home in the Institute of Analysis and Scientific Computing: Prof. Jens Markus Melenk, Prof. Dirk Praetorius, Ms. Brigitte Ecker, Maximilian Bernkopf, Markus Faustmann, Gregor Mitscha-Baude, José Alberto Morales Escalante, Gudmund Pammer, Stefan Rigger, Benjamin Stadlbauer, and Leila Taghizadeh.

I deeply appreciate the support, encouragement, and motivation my parents and siblings – Leon, Betsy, Yishai, Yoav, and Kayla – have given me over the past few years. I can finally answer the question "When will you be finished?" with "Now!"

I cannot begin to express my appreciation, love, and respect for my wife, Nadia, who somehow found the time to listen to me drone on about electromagnetics and optimization while she was pursuing a PhD of her own. I could not have done it without you!

Finally, I would like to thank my son, Raphael (Rafi) Blankrot, without whom this work would have been finished sooner – but it would have been a far less enjoyable experience.

This dissertation is dedicated to the memory of my grandfather, Aron Blankrot.

Eidesstattliche Erklärung

Ich erkläre an Eides statt, dass ich die vorliegende Dissertation selbstständig und ohne fremde Hilfe verfasst, andere als die angegebenen Quellen und Hilfsmittel nicht benutzt bzw. die wörtlich oder sinngemäß entnommenen Stellen als solche kenntlich gemacht habe.

Wien, am 10.09.2020

Boaz Blankrot

Contents

1 Introduction

1.1 Background and motivation

Photonic structures are present in a wide variety of areas ranging from the natural world to the artificial. They provide iridescent color to certain insects [1] and peacock feathers [2], can be found in ancient colored glass [3], and of course are present in many modern applications. Opinions differ on the precise delineation between metamaterials, photonic crystals, and other nanoscale light-manipulating structures. When speaking generally, in this chapter we will use the umbrella term *photonic structure*.

The scientific study of photonic structures experienced two breakthroughs towards the end of the nineteenth century. In 1887, Rayleigh started the study of one-dimensional photonic crystals by analyzing the reflectivity of periodic dielectric stacks [4], and discovered the existence of a band gap, that is, waves with frequencies within a certain range do not propagate into the crystal. In 1898, Bose demonstrated an artificial chiral material in the microwave regime [5] by twisting sections of jute, thereby rotating the plane of polarization of an incident electric field. These works set off two lines of research, namely what we now refer to as photonic crystals and metamaterials.

Notable milestones in the research of photonic crytals include the 1975 paper by Bykov [6]. There he studied theoretical spontaneous emission in one-dimensional photonic crystals and hypothesized about a possible extension to three dimensions for optical sources. Yablonovitch [7] and John [8] each theorized in 1987 about the possibility of photonic band gaps in three dimensional photonic crystals. Following these papers, both theoretical and experimental research efforts intensified, culminating in the fabrication of the first three-dimensional photonic crystal with a complete band gap [9]. The existence of a two-dimensional band gap was demonstrated in [10], both numerically and with microwave transmission experiments. Several years thereafter, Krauss et al. [11] fabricated a two-dimensional photonic crystal for infrared light with a standard lithography process, thus enabling integration with other optical components.

In the metamaterials line of research, during the first decade of the twentieth century, papers by Garnett [12] and Mie [13] provided models for calculating the electromagnetic scattering of small metallic spheres, thus giving a mathematical description for the optical behavior of glass colored by nanoparticles. Similarly to Bose, Lindman researched artificial chiral media, creating several composite structures with this characteristic [14]. In 1948, Kock [15] created microwave lenses by setting metallic building blocks of various shapes in a periodic pattern. Furthermore, he showed that the overall medium behaved as an artificial dielectric medium with tunable effective permittivity and permeability. The idea of artificial materials with simultaneously negative permittivity and permeability was suggested in 1967 by Veselago [16], and it was only in 2000 that such a metamaterial was realized for microwaves [17]. Soon thereafter, Pendry showed that such a metamaterial for optical

wavelengths would enable imaging beyond the diffraction limit [18]. These developments triggered widespread interest in metamaterials and vigorous research efforts.

For our purposes, we consider the following class of photonic structures: a large number of dielectric subwavelength inclusions with arbitrary smooth cross sections. The inclusions are suspended in a dielectric medium or vacuum, and can be approximated by their behavior in two dimensions. We note that if this structure is periodic, it is often referred to as a photonic crystal, such as the one illustrated in Fig. 1.1. Since our goal will be to optimize the inclusion parameters, the resulting structures herein may not be strictly considered photonic crystals, as they may be aperiodic. By appropriately choosing inclusion shape and material, photonic crystals can be designed to restrict light flow in some or all directions for a desired wavelength range. For example, the photonic crystal in Fig. 1.1 prevents transverse magnetic light propagation in any direction for wavelengths in the $2.25a - 3.65a$ range highlighted in yellow, where a is the lattice constant (for more details on this diagram, see Chapter 5).

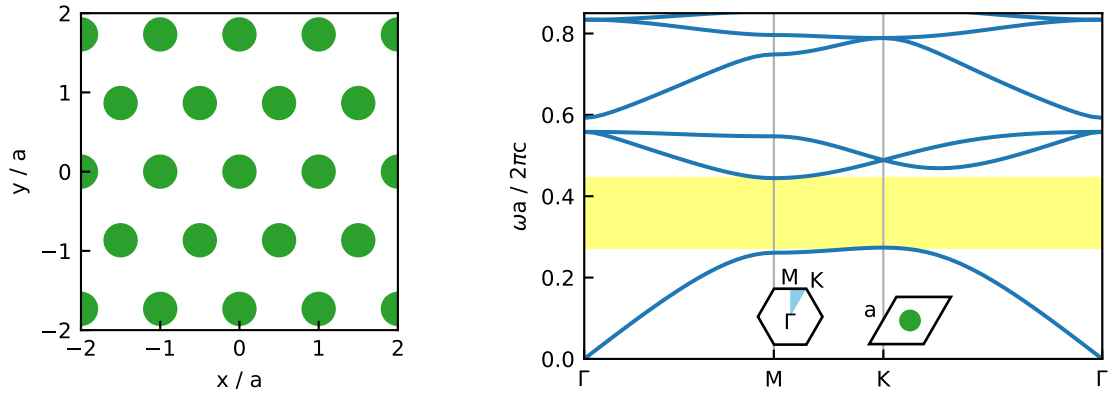

Fig. 1.1: Photonic crystal comprised of a triangular array of dielectric rods with radius $r/a = 0.2$ in air (left). Photonic band structure for this crystal (right).

We list several applications of photonic structures, many of which belong to our class of interest. Waveguides may be constructed by introducing defects to photonic crystals, which can then guide light along a path with very low losses, and these can be combined with bends, splitters, and filters [19]. Thus, they show great promise for integrated optical communication [20], and they have also been used to implement modulators for optical interconnects [21]. Large-scale integration of all-optical RAM has been demonstrated by combining these waveguides with photonic crystal nanocavities [22]. Optical computing [23], where light also replaces the electrical signals inside the processing unit, has recently seen significant progress with the implementation of photonic crystal-based arithmetic units [24] as well as electronic-photonic arithmetic units [25], and continues to show promise of faster and power-efficient processors, although it presents its own challenges. Achieving an all-optical processor requires the reinvention of all classical processor components as optical devices, and it is therefore highly desirable to develop a versatile design process for such components.

One example of a dielectric metamaterial is the metalens [26] – a device that matches

or supersedes traditional lenses – which has applications in traditional imaging as well as chiral imaging [27], nano-optic endoscopes [28], and light-field imaging [29]. These metalenses, often constructed by a large number of subwavelength building blocks arranged on a substrate, can be substantially thinner than their traditional glass counterparts. The size, shape, rotation, and material of each building block collectively dictate the optical behavior of the metalens. Zero-index metamaterials have been sought after due to their many prospective applications including cloaking [30] and radiation focusing [31] but these initially contained metallic inclusions, and thus exhibited large losses [32]. More recently, such metamaterials have been fabricated using all-dielectric unit cells, such as silicon rods [33], thus alleviating that problem. Fig. 1.2 presents several examples of fabricated dielectric photonic structures.

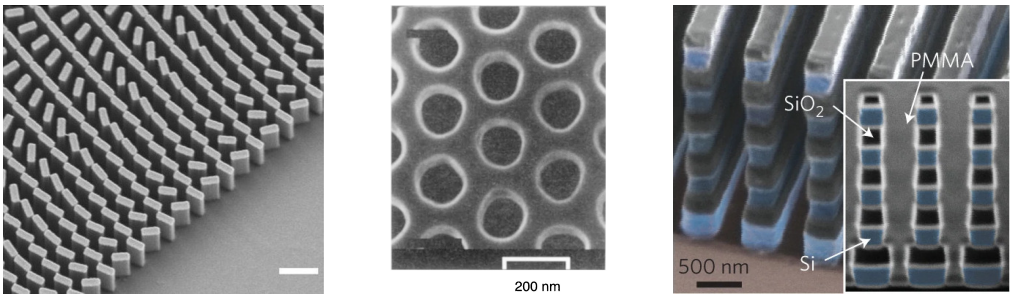

(a) (b) (c)

Fig. 1.2: Examples of fabricated photonic structures. (a) Metalens for chiral imaging, adapted from [27] with permission from ACS[1]. (b) Two-dimensional photonic crystal [11] and (c) all-dielectric zero-index metamaterial [33], both adapted by permission from Springer Nature.

The design process for photonic structures, such as the ones discussed above, can be fairly complex as their parameters introduce many interplaying degrees of freedom. Analytical considerations provide both a good starting point for optimizing a design, and an invaluable tool for understanding the underlying physics of how a structure responds, but often cannot lead to optimal designs on their own. Optimal designs can be highly irregular, as we will see throughout this work, in which case they are even less likely to be found manually. Therefore, automating parts of the design process can discover better-performing designs that might have been overlooked otherwise, while often requiring less time.

The need for optimization has been recognized by the photonics community over the past two decades and addressed with various successful approaches, see [34, 35] and the discussion in Chapter 2 for a general review of different approaches and results. In particular, one notable approach to nanophotonic design is that of topology optimization, which has been utilized to reduce losses in photonic crystal waveguide bends [36], design demultiplexers [37], and design wideband power splitters [38]. This approach is known for its flexibility, since arbitrary devices can be constructed by optimizing over a very large parameter space. Another important field in nanophotonic design is that of photonic crystal

[1]Source: `https://pubs.acs.org/doi/10.1021/acs.nanolett.6b01897`. Further permissions related to the material excerpted should be directed to the ACS.

cavity optimization, where a general aim is to increase the quality factor Q while reducing the cavity volume. One approach pursued in [39] optimized over air hole locations using a genetic algorithm, and resulted in significantly higher Q-values than contemporary designs. Recently, a machine learning technique was employed in [40] to optimize air hole locations for high-Q photonic crystal cavities. By limiting the number of costly field calculations, this method allowed scaling of the optimization problem to a larger parameter space. The aforementioned applications, many of which are facilitated by structures within our class of interest, further motivate the development of an efficient automated procedure that yields high-performing designs. Specifically, we focus on rotation angle optimization for arbitrarily shaped inclusions, and radius optimization for circular rods (for a simple example of such an optimization problem see Fig. 2.1).

Whether designs are achieved via analytical considerations or automated optimization, it is valid to question how useful they will be in a real world setting. All fabrication processes, including those used to etch photonic structures, suffer from uncertainties which can severely impact device performance [41]. These uncertainties can manifest not only in the shape and location of the structures, but also in the electromagnetic properties of the material. There is an assortment of measures by which we can quantify the effects of these uncertainties on device performance, including probabilistic measures such as mean and variance, and deterministic ones such as worst-case robustness [42], which we focus on in this work. Specifically, we use worst-case robustness to implementation uncertainty, which replaces a traditional function $f(\mathbf{x})$ with a robust function $f_\mathrm{w}(\mathbf{x}) = \max_{\Delta\mathbf{x}} f(\mathbf{x}+\Delta\mathbf{x})$, given bounds on the uncertainty of every design variable $\pm\Delta x_i$. While running an optimization process on f_w adds significant complexity and run time, particularly for large numbers of variables, we are guaranteed at least a certain level of performance regardless of the precise uncertainties present in a specific implementation. Therefore, it seems natural to couple this approach of *robust optimization* to the aforementioned class of photonic structures.

Robust optimization has been widely studied over the past two decades, with a variety of methods proposed to handle different types of functions and constraints [43]. However, many of these methods restrict the objective and/or constraints to specific classes in order to reformulate the robust optimization problem as a standard optimization problem. Thus, they are not applicable to photonic design problems, which are generally nonlinear and depend on simulation results. Several methods for robust optimization of nonlinear problems have been introduced over the past few years. One class of such methods uses a nested approach to solve the resulting minimax problem, where an outer optimizer uses a local search [44] or simulated annealing [45] to solve the minimization problem, and an inner maximizer aims to calculate f_w with an approximate global optimizer. Another algorithm, based on cutting-plane methods, alternates between the minimization and maximization steps and considers sequentially larger uncertainty sets [46]. As opposed to these methods, which rely on potentially expensive function evaluations in every step, surrogate-based modeling, used in [47] to perform robust optimization, reduces function evaluations by replacing them with cheaper meta-model evaluations. Most recently, a robust optimization algorithm was proposed [48] that also aims to reduce the number of expensive function calls, but without building an approximate model. This algorithm explores regions of the variable domain far from any previously visited non-robust points, and has since been extended with particle swarm optimization [49].

Despite the stated benefits of robust optimization, relatively few works have focused on applying it to photonic structures (see Chapter 6 for a survey of this literature). One previously-studied research avenue was that of robustness to under- and over-etching of photonic crystals [50]. Applying distinct radius perturbations to different rods had not been considered in this context, although in our experience it proves more detrimental to desired behavior.

1.2 Objectives of this work

The main goal of this work was to construct a method for the fast and automated design of a large class of dielectric structures. The first step towards our goal was to optimize these structures with respect to a function of the electric field intensity (or squared amplitude) at an arbitrarily chosen set of points. An essential tool for that was a way to evaluate those objective functions quickly, and in a manner that takes advantage of the repetitive nature of our structures; this is crucial for keeping the computational complexity of the optimization process in check given the high dimensionality of our problems. Therefore, we needed to implement an integral equation-based approach which would allow changing inclusion rotation and radius with ease. Next, we aimed to extend our method to also handle power flow optimization in the presence of multiple incident fields of different frequencies. Finally, and spurred by our results, we felt it important to address the robustness of the structures achieved by nominal optimization, or lack thereof. Therefore, we wished to build upon our approach to enable robust optimization, where the optima would be more resistant to implementation errors. As much as possible, we maintained the goal of making our code public with an open source license.

1.3 Outline

This work is presented as a cumulative thesis which is comprised of four peer-reviewed papers, listed in order of writing (1–4). An additional paper, (5), has been submitted for publication. We briefly describe the contents and main takeaways from each paper.

(1) B. Blankrot and C. Heitzinger, "Efficient Computational Design and Optimization of Dielectric Metamaterial Structures," *IEEE Journal on Multiscale and Multiphysics Computational Techniques*, vol. 4, pp. 234–244, Oct. 2019.

First we give a precise definition of the class of structures our approach applies to, where we intend to optimize over the radii of circular inclusions and the rotation angles of non-circular inclusions. We implement an electromagnetic solver which is tailored to these structures, provides an analytical gradient for gradient-based optimization and relies on precomputations as much as possible in order to reduce time spent in each iteration of the optimization loop. To this end, we transform each inclusion to a cylindrical harmonics representation which allows simple replication and movement as well as a gradient computation with respect to rotation angle. Circular inclusions are trivially differentiable with respect to their radius using this representation. The cylindrical harmonics representation also allows for a dramatic

decrease in the degrees of freedom necessary to compute the scattered field from each inclusion for a given error. While this representation introduces another error term, we discuss and demonstrate how it can be computed and reduced for a given inclusion.

As in [51], this representation is combined with multiple scattering theory in order to calculate the electromagnetic interactions between inclusions. Notably, the resulting system of equations separates the dependency of these interactions on location from shape, thus allowing optimization without recalculating the entire system matrix. Furthermore, we describe the process of speeding up the solution of the system matrix using the Fast Multipole Method [52].

We then move on to describing how to optimize functions of the electric field intensity at a desired set of points and use the adjoint-state method [53] to calculate all derivatives with a single system matrix solution. We apply our approach to two examples. In the first, we show that the field transmitted by a disordered collection of inclusions can be substantially increased by optimizing their rotation angles. For the second example, we discuss the photonic crystal implementation of the Luneberg lens which focuses a plane wave to a single point. We show that by optimizing the inclusion radii, we can increase the field amplitude at the focal point by 55%.

Finally, we discuss the irregularity of the optimized structures which conforms to previous observations about the functionality of aperiodic vs. periodic structures.

(2) B. Blankrot and C. Heitzinger, "ParticleScattering: Solving and optimizing multiple-scattering problems in Julia," *Journal of Open Source Software*, vol. 3, no. 25, p. 691, May 2018.

We discuss the typical use-case for the ParticleScattering package and give an overview of the optimization and solution process, as well as the visualization features of the package. This peer-reviewed Julia package contains documentation including examples with tutorials as well as tests covering most solver functionality.

(3) B. Blankrot and C. Heitzinger, "Automated Design of Photonic Crystal Demultiplexers," *Proc. of the 2018 12th International Congress on Artificial Materials for Novel Wave Phenomena (Metamaterials'2018)*, Espoo, Finland, 27–30 Aug. 2018, pp. 55–57.

We apply the approach from Chapter 2 to the more general setting of optimizing multi-frequency behavior. We aim to focus two incoming plane waves of different frequencies to different locations in the structure. As we had not yet applied the adjoint-state method at this point in our work, the optimization process had a runtime which is longer by an order of magnitude than we would otherwise expect. Nonetheless, the process achieved a structure with strong amplification for both wavelengths, as well as low crosstalk.

(4) B. Blankrot and C. Heitzinger, "Design of aperiodic demultiplexers and optical diodes by optimizing photonic crystals," *OSA Continuum*, vol. 2, no. 7, pp. 2244–2252, Jul. 2019.

Motivated by the many applications of photonic crystals to optical communication and computing, we shift our focus from functions of the electric field to power flow, which

can better capture optical device specifications. After providing the mathematical treatment for this setting, we optimize a two-wavelength demultiplexer as well as a structure which exhibits asymmetric light transmission. For the demultiplexer, we improve upon the performance of an already-optimized design by optimizing over all inclusions, whereas the optical diode (or, more precisely, the asymmetric light transmitter) was obtained by optimizing over the radii of a photonic crystal with a band gap at the frequency of interest. Choosing a current filament vs. a plane wave as the incident field resulted in different optimal diode structures. These had transmission ratios of 46 dB and 58 dB and were very narrow-banded, as opposed to the demultiplexer, where no obvious narrowing was observed. As with previous results, the optimized structures were irregular.

(5) B. Blankrot and C. Heitzinger, "On the robust optimization of photonic structures for asymmetric light transmission," *Submitted for publication*, Jul. 2020.

Here we take the step from nominal or traditional optimization of photonic structures to their robust optimization, which is important for real world applications, with our focus being on structures that exhibit asymmetric light transmission. We begin by examining a nominally optimized structure and identify a seemingly harmless and visually imperceptible perturbation which leads to a complete loss of its functionality. In fact, the perturbed device allowed more light in the reverse direction than in the forward direction. Next, we select and implement two strategies for robust optimization of circular inclusion radii. The first strategy, Robust Simulated Annealing [45], is a nested approach while the second strategy, Largest Empty Hypercube [48], reduces the number of function evaluations by moving away from already-explored regions with high objective function values. For the latter, we utilize k-d trees with a nearest neighbor search in order to find empty regions more quickly.

We review their observed strengths and drawbacks while discussing scenarios where each method would shine best. Of special importance is the pitfall of underestimating the worst case perturbation of a given point, as it can negatively impact convergence. Both methods yield structures with asymmetric light transmission even in the presence of worst-case implementation errors. However, the robustness of our structures comes with a penalty on their nominal behavior, i.e. absent any error. Interestingly, the robust structures were also more resilient to input wavelength error than the traditionally optimized structures in our earlier work.

The remainder of this chapter consists of an introduction to the electromagnetic theory and optimization tools used later in the manuscript. The following chapters each contain one of the aforementioned papers, with minor changes in formatting and notation. The thesis also contains a technical appendix with elaborated derivations that were omitted from the papers.

1.4 Electromagnetic theory

Here we give a brief reminder of electromagnetic theory and state our working assumptions to lay the foundation for our later mathematical developments. As is well known, classical

electromagnetic fields in and around media can be described using Maxwell's equations, which in differential form state that

$$\nabla \times \mathcal{E} = -\frac{\partial \mathcal{B}}{\partial t}\,, \tag{1.1a}$$

$$\nabla \times \mathcal{H} = \mathcal{J} + \frac{\partial \mathcal{D}}{\partial t}\,, \tag{1.1b}$$

$$\nabla \cdot \mathcal{D} = \rho, \tag{1.1c}$$

$$\nabla \cdot \mathcal{B} = 0, \tag{1.1d}$$

where $\mathcal{E}$, $\mathcal{H}$, $\mathcal{D}$, and $\mathcal{B}$ are the electric field, the magnetic field, the electric flux density, and the magnetic flux density. ρ and $\mathcal{J}$ denote external volume charge and electric current densities.

In this work, we assume piecewise homogeneous isotropic linear materials, as well as $\exp(-i\omega t)$ harmonic time dependence, thereby reducing (1.1) to

$$\nabla \times \boldsymbol{E} = i\omega\mu\boldsymbol{H}, \tag{1.2a}$$

$$\nabla \times \boldsymbol{H} = -i\omega\varepsilon\boldsymbol{E}, \tag{1.2b}$$

$$\nabla \cdot \varepsilon\boldsymbol{E} = 0, \tag{1.2c}$$

$$\nabla \cdot \mu\boldsymbol{H} = 0, \tag{1.2d}$$

in each source-free region, where $\boldsymbol{E}$, $\boldsymbol{H}$ are the time-harmonic analogues of $\mathcal{E}$, $\mathcal{H}$, and ε, μ are the permittivity and permeability of the material. By manipulating these equations and defining the wavenumber $k = \omega\sqrt{\mu\varepsilon}$, we obtain the vector Helmholtz equation

$$(\nabla^2 + k^2)\boldsymbol{E} = 0. \tag{1.3}$$

For a general smooth closed boundary $\partial\Omega$, such as the one between an inclusion and its host medium with differing electromagnetic properties, we denote the unit vector normal to the boundary pointing from medium 1 to medium 2 by $\hat{n}$ and have the boundary conditions [54] given by

$$\hat{n} \times (\boldsymbol{E}^{(2)} - \boldsymbol{E}^{(1)})|_{\partial\Omega} = 0, \tag{1.4a}$$

$$\hat{n} \times (\boldsymbol{H}^{(2)} - \boldsymbol{H}^{(1)})|_{\partial\Omega} = \boldsymbol{J}_s, \tag{1.4b}$$

$$\hat{n} \cdot (\varepsilon^{(2)}\boldsymbol{E}^{(2)} - \varepsilon^{(1)}\boldsymbol{E}^{(1)})|_{\partial\Omega} = \rho_s, \tag{1.4c}$$

$$\hat{n} \cdot (\mu^{(2)}\boldsymbol{H}^{(2)} - \mu^{(1)}\boldsymbol{H}^{(1)})|_{\partial\Omega} = 0. \tag{1.4d}$$

In this work, we focus on perfect dielectrics and thus have no surface charges ρ_s nor surface currents $\boldsymbol{J}_s$. The time-averaged power flow through a surface S can be calculated with the Poynting vector, yielding

$$P = \frac{1}{2}\int_S \mathrm{Re}(\boldsymbol{E} \times \boldsymbol{H}^*) \cdot \mathrm{d}\mathbf{s}. \tag{1.5}$$

This equation will be useful in Chapters 5 and 6, where we optimized a function of the power flow through several surfaces in order to automatically design a diplexer and an asymmetric light transmitter.

In two dimensions, any electromagnetic field can be decomposed into a linear combination of transverse magnetic (TM) and transverse electric (TE) fields with respect to the z axis. This allows us to express the electromagnetic fields in terms of two scalar fields—E_z in the TM case and H_z for TE—thereby replacing (1.3) with two scalar Helmholtz equations that can be solved separately and similarly. For this reason, we focus on solutions to the TM problem in this dissertation, while noting that all of the methods are readily carried over to the TE case with small modifications. Assuming a TM electric field of the form $\boldsymbol{E} = (0, 0, E_z)$, the magnetic field is then given by

$$\boldsymbol{H} = \frac{1}{i\omega\mu}\Big(\frac{\partial E_z}{\partial y}, -\frac{\partial E_z}{\partial x}, 0\Big). \tag{1.6}$$

While Maxwell's equations may be solved directly for the electromagnetic fields in a domain using various numerical methods (e.g. the Finite Element Method or Finite-Difference Time Domain [55]), integral equation techniques solve for the sources that create those fields. The latter approach has two major advantages: it allows us to handle unbounded domains with ease, and reduces the dimensionality of the problem as we are discretizing the surfaces of a given geometry instead of the volumes. Thus the two-dimensional geometries in this work can be discretized using only line integrals. For example, given a single scatterer with boundary $\partial\Omega$, we may assume unknown potential densities σ and μ (not to be confused with the permeability μ above) on $\partial\Omega$ such that the electric field anywhere is given by

$$E_z(\mathbf{r}) = \int_{\partial\Omega} G^k(\mathbf{r}, \mathbf{r}')\sigma(\mathbf{r}') + \hat{n}' \cdot \nabla' G^k(\mathbf{r}, \mathbf{r}')\mu(\mathbf{r}')\, \mathrm{d}\mathbf{r}', \tag{1.7}$$

where $G^k(\mathbf{r}, \mathbf{r}') = \frac{i}{4}H_0^{(1)}(k|\mathbf{r} - \mathbf{r}'|)$ is the corresponding Green's function in a domain with wavenumber k. The densities σ, μ are found by imposing the tangential boundary conditions of (1.4) on E_z and $\boldsymbol{H}$ while taking the appropriate limit [56].

We refer the reader to [54, 56] for in-depth treatments of electromagnetic theory with an emphasis on integral equation methods.

1.5 Optimization methods

We assume the reader has some familiarity with optimization and provide a rudimentary overview of two optimization methods employed in our work. For an overview of optimization methods for photonic structures, see [34].

1.5.1 BFGS

The Broyden–Fletcher–Goldfarb–Shanno (BFGS [57]) algorithm is a quasi-Newton method used for solving unconstrained nonlinear optimization problems. Quasi-Newton methods approximate the inverse Hessian matrix using the gradient, thereby incorporating some second-order information without explicit Hessian calculations. Since BFGS is a local

optimization method, it will not necessarily find the global optimum for non-convex problems, but only the local optimum closest to the initial point. Fig. 1.3(a) shows two BFGS runs on the McCormick function, which is given by

$$f(x, y) = \sin(x + y) + (x - y)^2 - 1.5x + 2.5y + 1. \tag{1.8}$$

While both runs terminate at the nearest local minimum within 6 iterations, only one of them (shown in red) found the global minimum.

One way of extending this algorithm to constrained optimization problems is by incorporating interior-point or barrier methods, which add a penalty to the objective function such that the unconstrained algorithm cannot violate the constraints. Assuming the optimization problem has the form

$$\begin{aligned} \min_{\mathbf{x}} \quad & f(\mathbf{x}) \\ \text{subject to} \quad & \mathbf{c}(\mathbf{x}) \leq 0, \end{aligned} \tag{1.9}$$

we instead minimize the unconstrained objective $f(\mathbf{x}) + \rho b(\mathbf{c}(\mathbf{x}))$, where the barrier function b is smooth, non-negative, and approaches infinity at the constraint boundary. Our choice of barrier function is the log barrier

$$b(\mathbf{c}(\mathbf{x})) = \begin{cases} -\sum_j \log(-c_j(\mathbf{x})), & \text{for } \mathbf{c}(\mathbf{x}) \leq 0 \\ \infty, & \text{else} \end{cases} \tag{1.10}$$

which is combined with a parameter ρ that shrinks every several iterations to reduce the impact of the barrier as the algorithm converges. This barrier method is used to impose bounds on the cylinder radii in Chapters 2 to 5, and is generally dependable. One downside of this method is that an optimum on or near the boundary can only be found once ρ is at or near zero.

Another augmentation of BFGS that supports simple bound constraints of the form $\mathbf{x}_{\min} \leq \mathbf{x} \leq \mathbf{x}_{\max}$ is the L-BFGS-B method [58] which utilizes a gradient projection method. We discovered that this method converged faster than the barrier methods on our examples, as eliminating the inner loop over ρ reduced the number of function evaluations. For this reason, L-BFGS-B was adopted for the gradient-based optimization over cylinder radii in Chapter 6.

1.5.2 Simulated annealing

Simulated annealing [59] is a stochastic global optimization method loosely inspired by the annealing process in metallurgy. In each iteration of this method, a candidate point $\mathbf{x}$ is randomly selected and the objective is computed at that point. A temperature parameter governs the probability that the method will accept a point with a worse objective value, whereas improving points are always accepted. One common choice for the acceptance probability of a new point is the Metropolis criterion

$$P(\mathbf{x} \to \mathbf{x}') = \min\left(1, \exp\left(-\frac{f(\mathbf{x}') - f(\mathbf{x})}{T_i}\right)\right), \tag{1.11}$$

where T_i is the current temperature. T_i starts with a high value such that vast areas of the domain can be explored, but as the temperature drops the algorithm becomes increasingly unlikely to accept a worse value and thus resembles a gradient-free local search. Since simulated annealing is based on a heuristic instead of a precise formula, it is frequently tuned and adapted with various temperature cooling schedules, candidate point distributions, and occasionally separate temperatures for each $x_i \in \mathbf{x}$. A variant of simulated annealing was used for the outer loop of a robust optimization approach in Chapter 6.

Two example runs of simulated annealing on the McCormick function (1.8) are depicted in Fig. 1.3(b), where they take different paths due to the stochastic nature of the algorithm. While both paths eventually arrive at the neighborhood of the global minimum after 1000 iterations, several hundred more iterations pass before the optimum is consistently achieved with the precision of the BFGS method.

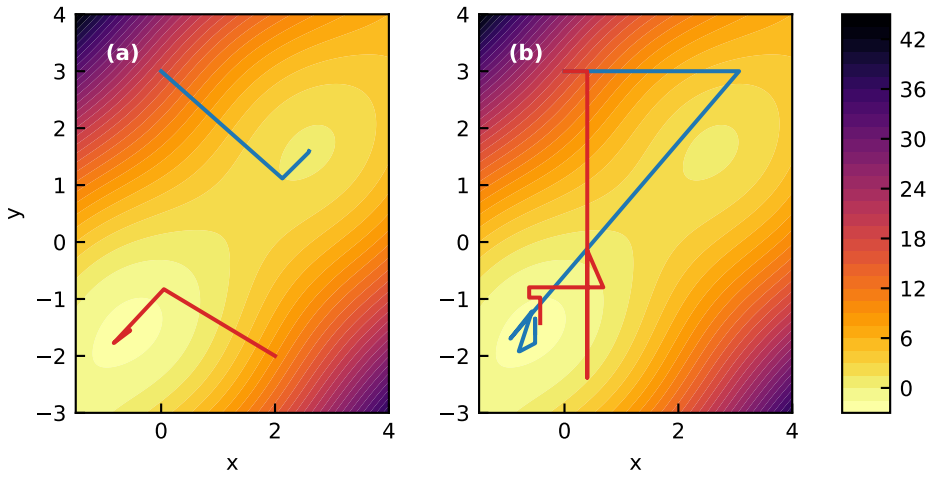

Fig. 1.3: The McCormick function optimized using (a) BFGS and (b) simulated annealing.

1.6 Further research

There are several research avenues that would be interesting to explore in continuation of this work. First and foremost would be an extension to three-dimensional structures. The main impediment to such an extension would be that the multipole expansion spheres surrounding the particles cannot intersect, as explained in Section 2.3.1; nonetheless, such an extension would enable analysis and optimization of real-world metalenses. For the robust-optimization framework, it would be interesting to support radius uncertainty for rotation angle optimization, in order to study the effects of over- and under-etching on these structures. Finally, different robust optimization metrics, such as probabilistic ones, would be worth exploring instead of the worst case considered in Chapter 6.

Bibliography

[1] L. P. Biró, Z. Bálint, K. Kertész, Z. Vértesy, G. I. Márk, Z. E. Horváth, J. Balázs, D. Méhn, I. Kiricsi, V. Lousse, and J.-P. Vigneron, "Role of photonic-crystal-type structures in the thermal regulation of a lycaenid butterfly sister species pair," *Physical Review E*, vol. 67, p. 021907, Feb. 2003.

[2] J. Zi, X. Yu, Y. Li, X. Hu, C. Xu, X. Wang, X. Liu, and R. Fu, "Coloration strategies in peacock feathers," *Proceedings of the National Academy of Sciences*, vol. 100, pp. 12576–12578, Oct. 2003.

[3] D. J. Barber and I. C. Freestone, "An investigation of the origin of the colour of the Lycurgus cup by analytical transmission electron microscopy," *Archaeometry*, vol. 32, no. 1, pp. 33–45, 1990.

[4] L. Rayleigh, "XVII. on the maintenance of vibrations by forces of double frequency, and on the propagation of waves through a medium endowed with a periodic structure," *The London, Edinburgh, and Dublin Philosophical Magazine and Journal of Science*, vol. 24, pp. 145–159, Aug. 1887.

[5] J. C. Bose, "On the rotation of plane of polarisation of electric waves by a twisted structure," *Proceedings of the Royal Society of London*, vol. 63, pp. 146–152, 1898.

[6] V. P. Bykov, "Spontaneous emission from a medium with a band spectrum," *Soviet Journal of Quantum Electronics*, vol. 4, pp. 861–871, July 1975.

[7] E. Yablonovitch, "Inhibited spontaneous emission in solid-state physics and electronics," *Physical Review Letters*, vol. 58, pp. 2059–2062, May 1987.

[8] S. John, "Strong localization of photons in certain disordered dielectric superlattices," *Physical Review Letters*, vol. 58, pp. 2486–2489, June 1987.

[9] E. Yablonovitch, T. J. Gmitter, and K. M. Leung, "Photonic band structure: The face-centered-cubic case employing nonspherical atoms," *Physical Review Letters*, vol. 67, pp. 2295–2298, Oct. 1991.

[10] R. D. Meade, K. D. Brommer, A. M. Rappe, and J. D. Joannopoulos, "Existence of a photonic band gap in two dimensions," *Applied Physics Letters*, vol. 61, no. 4, pp. 495–497, 1992.

[11] T. F. Krauss, R. M. D. L. Rue, and S. Brand, "Two-dimensional photonic-bandgap structures operating at near-infrared wavelengths," *Nature*, vol. 383, pp. 699–702, Oct. 1996.

[12] J. C. M. Garnett, "XII. colours in metal glasses and in metallic films," *Philosophical Transactions of the Royal Society of London. Series A, Containing Papers of a Mathematical or Physical Character*, vol. 203, pp. 385–420, Jan. 1904.

[13] G. Mie, "Beiträge zur Optik trüber Medien, speziell kolloidaler Metallösungen," *Annalen der Physik*, vol. 330, no. 3, pp. 377–445, 1908.

[14] I. V. Lindell, A. H. Sihvola, and J. Kurkijarvi, "Karl F. Lindman: the last Hertzian, and a harbinger of electromagnetic chirality," *IEEE Antennas and Propagation Magazine*, vol. 34, no. 3, pp. 24–30, 1992.

[15] W. E. Kock, "Metallic delay lenses," *Bell System Technical Journal*, vol. 27, pp. 58–82, Jan. 1948.

[16] V. G. Veselago, "The electrodynamics of substances with simultaneously negative values of ϵ and μ," *Soviet Physics Uspekhi*, vol. 10, pp. 509–514, Apr. 1968.

[17] D. R. Smith, W. J. Padilla, D. C. Vier, S. C. Nemat-Nasser, and S. Schultz, "Composite medium with simultaneously negative permeability and permittivity," *Physical Review Letters*, vol. 84, pp. 4184–4187, May 2000.

[18] J. B. Pendry, "Negative refraction makes a perfect lens," *Physical Review Letters*, vol. 85, pp. 3966–3969, Oct. 2000.

[19] J. D. Joannopoulos, S. G. Johnson, J. N. Winn, and R. D. Meade, *Photonic Crystals: Molding the Flow of Light*. Princeton University Press, 2 ed., 2008.

[20] H.-G. Park, C. J. Barrelet, Y. Wu, B. Tian, F. Qian, and C. M. Lieber, "A wavelength-selective photonic-crystal waveguide coupled to a nanowire light source," *Nature Photonics*, vol. 2, pp. 622–626, Sept. 2008.

[21] X. Wang, H. Tian, and Y. Ji, "Photonic crystal slow light Mach-Zehnder interferometer modulator for optical interconnects," *Journal of Optics*, vol. 12, p. 065501, June 2010.

[22] E. Kuramochi, K. Nozaki, A. Shinya, K. Takeda, T. Sato, S. Matsuo, H. Taniyama, H. Sumikura, and M. Notomi, "Large-scale integration of wavelength-addressable all-optical memories on a photonic crystal chip," *Nature Photonics*, vol. 8, pp. 474–481, May 2014.

[23] J. Touch, A.-H. Badawy, and V. J. Sorger, "Optical computing," *Nanophotonics*, vol. 6, no. 3, pp. 503–505, 2017.

[24] S. Esmaeili and A. K. Cherri, "Photonic crystal-based all-optical arithmetic circuits without SOA-based switches," *Optik*, vol. 125, no. 14, pp. 3710–3713, 2014.

[25] Z. Ying, C. Feng, Z. Zhao, S. Dhar, H. Dalir, J. Gu, Y. Cheng, R. Soref, D. Z. Pan, and R. T. Chen, "Electronic-photonic arithmetic logic unit for high-speed computing," *Nature Communications*, vol. 11, May 2020.

[26] H. Liang, A. Martins, B.-H. V. Borges, J. Zhou, E. R. Martins, J. Li, and T. F. Krauss, "High performance metalenses: numerical aperture, aberrations, chromaticity, and trade-offs," *Optica*, vol. 6, pp. 1461–1470, Dec. 2019.

[27] M. Khorasaninejad, W. Chen, A. Zhu, J. Oh, R. Devlin, D. Rousso, and F. Capasso, "Multispectral chiral imaging with a metalens," *Nano Letters*, vol. 16, no. 7, pp. 4595–4600, 2016.

[28] H. Pahlevaninezhad, M. Khorasaninejad, Y.-W. Huang, Z. Shi, L. P. Hariri, D. C. Adams, V. Ding, A. Zhu, C.-W. Qiu, F. Capasso, and M. J. Suter, "Nano-optic endoscope for high-resolution optical coherence tomography in vivo," *Nature Photonics*, vol. 12, pp. 540–547, July 2018.

[29] R. J. Lin, V.-C. Su, S. Wang, M. K. Chen, T. L. Chung, Y. H. Chen, H. Y. Kuo, J.-W. Chen, J. Chen, Y.-T. Huang, J.-H. Wang, C. H. Chu, P. C. Wu, T. Li, Z. Wang, S. Zhu, and D. P. Tsai, "Achromatic metalens array for full-colour light-field imaging," *Nature Nanotechnology*, vol. 14, pp. 227–231, Jan. 2019.

[30] J. Hao, W. Yan, and M. Qiu, "Super-reflection and cloaking based on zero index metamaterial," *Applied Physics Letters*, vol. 96, no. 10, p. 101109, 2010.

[31] A. Alù, M. G. Silveirinha, A. Salandrino, and N. Engheta, "Epsilon-near-zero metamaterials and electromagnetic sources: Tailoring the radiation phase pattern," *Physical Review B*, vol. 75, p. 155410, Apr 2007.

[32] S. Jahani and Z. Jacob, "All-dielectric metamaterials," *Nature Nanotechnology*, vol. 11, pp. 23–36, Jan. 2016.

[33] P. Moitra, Y. Yang, Z. Anderson, I. I. Kravchenko, D. P. Briggs, and J. Valentine, "Realization of an all-dielectric zero-index optical metamaterial," *Nature Photonics*, vol. 7, pp. 791–795, Aug. 2013.

[34] K. Diest, *Numerical Methods for Metamaterial Design*. Dordrecht: Springer, 2013.

[35] K. Yao, R. Unni, and Y. Zheng, "Intelligent nanophotonics: merging photonics and artificial intelligence at the nanoscale," *Nanophotonics*, vol. 8, pp. 339–366, Mar. 2019.

[36] J. S. Jensen and O. Sigmund, "Systematic design of photonic crystal structures using topology optimization: Low-loss waveguide bends," *Applied Physics Letters*, vol. 84, no. 12, pp. 2022–2024, 2004.

[37] A. Y. Piggott, J. Lu, K. G. Lagoudakis, J. Petykiewicz, T. M. Babinec, and J. Vučković, "Inverse design and demonstration of a compact and broadband on-chip wavelength demultiplexer," *Nature Photonics*, vol. 9, no. 6, pp. 374–377, 2015.

[38] J. L. P. Ruiz, A. A. S. Amad, L. H. Gabrielli, and A. A. Novotny, "Optimization of the electromagnetic scattering problem based on the topological derivative method," *Optics Express*, vol. 27, pp. 33586–33605, Nov 2019.

[39] M. Minkov and V. Savona, "Automated optimization of photonic crystal slab cavities," *Scientific Reports*, vol. 4, p. 5124, 2014.

[40] T. Asano and S. Noda, "Optimization of photonic crystal nanocavities based on deep learning," *Optics Express*, vol. 26, pp. 32704–32717, Dec. 2018.

[41] A. Oskooi, A. Mutapcic, S. Noda, J. D. Joannopoulos, S. P. Boyd, and S. G. Johnson, "Robust optimization of adiabatic tapers for coupling to slow-light photonic-crystal waveguides," *Optics Express*, vol. 20, pp. 21558–21575, Sept. 2012.

[42] H.-G. Beyer and B. Sendhoff, "Robust optimization–a comprehensive survey," *Computer Methods in Applied Mechanics and Engineering*, vol. 196, no. 33–34, pp. 3190–3218, 2007.

[43] V. Gabrel, C. Murat, and A. Thiele, "Recent advances in robust optimization: An overview," *European Journal of Operational Research*, vol. 235, pp. 471–483, June 2014.

[44] D. Bertsimas, O. Nohadani, and K. M. Teo, "Robust optimization for unconstrained simulation-based problems," *Operations Research*, vol. 58, no. 1, pp. 161–178, 2010.

[45] D. Bertsimas and O. Nohadani, "Robust optimization with simulated annealing," *Journal of Global Optimization*, vol. 48, no. 2, pp. 323–334, 2010.

[46] M. Menickelly and S. M. Wild, "Derivative-free robust optimization by outer approximations," *Mathematical Programming*, vol. 179, pp. 157–193, Oct. 2018.

[47] S. U. Rehman and M. Langelaar, "Efficient infill sampling for unconstrained robust optimization problems," *Engineering Optimization*, vol. 48, no. 8, pp. 1313–1332, 2016.

[48] M. Hughes, M. Goerigk, and M. Wright, "A largest empty hypersphere metaheuristic for robust optimisation with implementation uncertainty," *Computers & Operations Research*, vol. 103, pp. 64–80, Mar. 2019.

[49] M. Hughes, M. Goerigk, and T. Dokka, "Particle swarm metaheuristics for robust optimisation with implementation uncertainty," *Computers & Operations Research*, vol. 122, p. 104998, Oct. 2020.

[50] F. Wang, J. S. Jensen, and O. Sigmund, "Robust topology optimization of photonic crystal waveguides with tailored dispersion properties," *Journal of the Optical Society of America B*, vol. 28, pp. 387–397, Mar. 2011.

[51] J. Lai, M. Kobayashi, and L. Greengard, "A fast solver for multi-particle scattering in a layered medium," *Optics Express*, vol. 22, pp. 20481–20499, Aug. 2014.

[52] R. Coifman, V. Rokhlin, and S. Wandzura, "The fast multipole method for the wave equation: a pedestrian prescription," *IEEE Antennas and Propagation Magazine*, vol. 35, pp. 7–12, June 1993.

[53] S. G. Johnson, "Notes on adjoint methods for 18.335." `http://math.mit.edu/stevenj/18.336/adjoint.pdf`, 2012.

[54] S. J. Orfanidis, *Electromagnetic Waves and Antennas*. New Brunswick, NJ: Rutgers University, 2002.

[55] T. Rylander, P. Ingelström, and A. Bondeson, *Computational Electromagnetics*. New York: Springer, 2 ed., 2012.

[56] D. Colton and R. Kress, *Integral Equation Methods in Scattering Theory*. New York: Wiley, 1983.

[57] J. Nocedal and S. Wright, *Numerical Optimization*. New York: Springer, 2 ed., 2006.

[58] R. H. Byrd, P. Lu, J. Nocedal, and C. Zhu, "A limited memory algorithm for bound constrained optimization," *SIAM Journal on Scientific Computing*, vol. 16, no. 5, pp. 1190–1208, 1995.

[59] S. Kirkpatrick, C. D. Gelatt, and M. P. Vecchi, "Optimization by simulated annealing," *Science*, vol. 220, no. 4598, pp. 671–680, 1983.

2 Efficient Computational Design and Optimization of Dielectric Metamaterial Structures

Authored by Boaz Blankrot and Clemens Heitzinger.
Published in *IEEE Journal on Multiscale and Multiphysics Computational Techniques*, vol. 4, pp. 234–244, Oct. 2019.
doi: 10.1109/JMMCT.2019.2950569

Abstract: Dielectric structures composed of many inclusions that manipulate light in ways the bulk materials cannot are commonly seen in the field of metamaterials. In these structures, each inclusion depends on a set of parameters such as size and orientation, which are difficult to ascertain. We propose and implement an optimization-based approach for designing such metamaterials in two dimensions by using a fast boundary element method and a multiple-scattering solver for a given set of parameters. This approach provides the backbone of an automated process for the design and analysis of metamaterials that does not rely on analytical approximations. We demonstrate the validity of our approach with simulations that converge to optimal parameter values and result in substantially better performance.

2.1 Introduction

In recent years, interest in dielectric metamaterials has grown considerably, as they have lower power dissipation [1] than their traditional counterparts and are easily fabricated [2, 3]. One prominent example of dielectric nanostructures is dielectric photonic crystals, which have been intensively investigated over the past thirty years [4, 5]. Photonic crystals are composed of a one- to three-dimensional periodic array of nanostructures, in which a small number of cells may be altered or defective. This structure is designed to allow, alter, or prevent the propagation of light for a selected range of wavelengths. These nanostructures can be e.g. round holes [6] or contain a complex network of nano-engineered rods [7, 8]. Thanks to their ability to control light flow, photonic crystals have promising applications in the developing field of optical computing. Replacing electronic components in integrated circuits with their photonic crystal counterparts will reduce the size and latencies of computer processors, while substantially increasing power efficiency [9, 10].

Dielectric metalenses are another class of recently popular all-dielectric metamaterials [11].

These metalenses allow manipulation of light for many practical applications, including chirality imaging [12], imaging with reduced aberrations [13], and optical fiber coupling [14]. Metalenses are typically comprised of numerous sub-wavelength building blocks arranged on a substrate. The properties of these building blocks dictate which effect the overall metalens has on light passing through it. There are many degrees of freedom in designing metalenses; the size, shape, rotation, and material of each individual building block can be adjusted arbitrarily, yielding a large variety of possible metalenses to meet different objectives [15]. Nevertheless, this freedom creates a large search space in choosing these parameters, which may number in the thousands.

Optimization methods have been employed in the past for designing optical structures. For example, dielectric antireflective layers with piecewise constant permittivity were designed with a gradient descent algorithm [16]. Optimization has been combined with the Finite-Difference Time-Domain (FDTD) method for optimizing mode confinement in photonic crystal cavities [17], however from a computational perspective, this approach may suffer from the need to re-solve the entire problem when changes are made to the parameters. Optimization of photonic crystal structures with circular inclusions was performed in [18] by means of transformation optics. Location optimization of circular dielectric rods in the radio-frequency regime was performed in [19, 20] using a finite differences discretization and both gradient-based and gradient-free algorithms. More recently, location optimization based on FDTD was used to design a photonic crystal exhibiting asymmetric light transmission in [21]. Combinatorial optimization, where scatterers in a photonic crystal structure are either present or absent but their shapes and locations remain constant, has been explored in [22] where a multipole expansion was used for round scatterers, and in [23] where the three-dimensional scatterers were discretized by surface elements. While the metaheuristic optimization methods used in those papers are able to escape local minima, they do so at the expense of substantially more function evaluations. Shape and topology optimization for optical structures is fairly established, both in the periodic [24, 25] and non-periodic cases [26]. Although topology optimization usually utilizes finite difference or finite element discretization, optimization of electromagnetic cloaking has been achieved using boundary elements as well [27].

We propose a specialized optimization-based method for analyzing and designing metamaterials in an automated fashion. The class of problems we consider consists of metamaterials with a large number of inclusions, which may be circular, but the number of non-circular prototype inclusions is small relative to the number of inclusions. We say that differently oriented inclusions of the same shape and material have the same prototype. This approach utilizes a multipole expansion and a fast multiple-scattering method [28, 29] to solve the underlying electromagnetic problem, and a gradient-based algorithm for the optimization. Our approach is most appropriate for optimizing radii in case of circular inclusions, and for optimizing rotation angles in case of general inclusions, which corresponds to the design of many photonic crystals and metamaterials. In the context of large-scale, aperiodic metamaterials in the class above, this type of efficient automation of the design process for specified optical properties has not been previously proposed.

The remainder of the paper is organized as follows. Section 2.2 gives the problem description and method overview. The mathematical formulation used for calculating the fields scattered by a collection of inclusions is presented in detail in Section 2.3. Section 2.4

presents our optimization framework for the automated design of metamaterials, which is given as pseudocode in Algorithm 2.1. Numerical results of both rotation angle and radius optimization are shown in Section 2.5, as well as a time complexity analysis of our approach. The results of this work are summarized in Section 2.6.

2.2 Problem and method description

The problems solved in this work consist of a layout of smooth inclusions which may be circular, and an objective function that models a desired electric field distribution at a set of points of interest. Our goal is to simultaneously optimize the radius of each circular inclusion and the rotation angle of each non-circular one to fit some desired behavior.

In this work, problems are restricted to time-harmonic incident fields scattering off a collection of two-dimensional inclusions in free space, where the variation $\exp(-i\omega t)$ is assumed and suppressed. We restrict our treatment to TM waves with respect to z, but the TE formulation is readily available with small modifications to the integral formulation and boundary conditions. We assume M inclusion surfaces Ω_m with smooth boundaries $\partial\Omega_m$, in which the wavenumber $k_m = \omega\sqrt{\mu_0\varepsilon_m}$ is real and constant, and Ω_0 denotes the open free-space domain. Hence the $\hat{\mathbf{z}}$ component of the electric field is the solution of the Helmholtz equation

$$\nabla^2 u + k_m^2 u = 0, \quad u = \begin{cases} u^{\text{inc}} + u^{\text{s}} & \text{in } \Omega_0, \\ u^{\text{s}} & \text{in } \Omega_{m\neq 0}, \end{cases} \tag{2.1}$$

where u^{inc} is the given incident field, u^{s} is the scattered field, and the jump in both u and the normal derivative $\partial u/\partial n$ is zero across all boundaries, corresponding to continuity of the tangential electric field and the normal magnetic flux density. In addition, the scattered field must satisfy the Sommerfeld radiation condition in Ω_0, but this is automatically satisfied due to the integral equation method used here. We assume an objective function that depends on the electric field intensity at multiple points, of the form

$$f_{\text{obj}} := \sum_{i=1}^{I} |u(\mathbf{r}_i)|^2, \tag{2.2}$$

where other functions of the intensity can be optimized via the chain rule. Fig. 2.1 contains a representative example of the optimization problems solved here, where the incident field intensity is to be maximized at a collection of points $\mathbf{r}_i$, by finding optimal rotation angles φ_j for the non-circular inclusions and optimal radii R_l for the circular ones.

We give an overview of our method. First, we use a boundary integral equation [30] to discretize each prototype inclusion once and transform it to a compressed cylindrical harmonics representation. It is straightforward to rotate and move this representation. We then apply a multiple-scattering approach [28, 31] on these representations in order to describe the electromagnetic interactions between the inclusions. Once we solve the arising multiple-scattering problem with the Fast Multipole Method (FMM) [32], we can easily compute the electromagnetic field at any point. This combination of boundary integral equation and multiple-scattering methods was applied to thin strips [33], three-dimensional

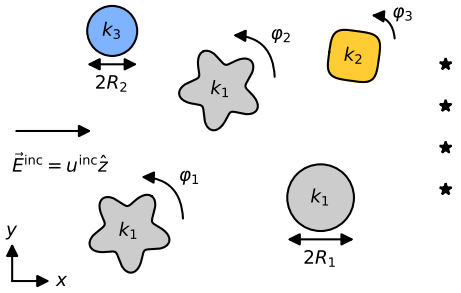

Fig. 2.1: Example optimization problem layout, where we wish to focus the incident plane wave u^{inc} at $\mathbf{r}_i$ (black stars) by optimizing over the rotation angles φ_j and radii R_l. Here, two of the inclusions have the same prototype as they have the same shape and wavenumber k_1.

scattering [34, 35], and two-dimensional multi-layered structures [29]. The computational complexity of this step is sufficiently low for employing optimization methods that require many solutions, as the ability to quickly compute the field at any collection of points makes it simple to define and compute an objective function for minimizing and/or maximizing the field intensity at multiple points. The integral equation approach naturally begets gradient-based optimization, which converges to a locally optimal set of parameters and yields an exact result in each step. We speed up the gradient-based optimization with the adjoint-state method [36] (see also [37]) which significantly decreases the optimization run time.

2.3 Scattering formulation

In this section, we describe the mathematical background used to calculate the field scattered by a collection of inclusions at any point. First, we handle the case of a single inclusion, then we provide the formulation used for multiple scattering, and lastly we apply FMM to accelerate the solution process. The mathematical development of the single inclusion and multiple-scattering formulations follow that of [29], and is repeated here for ease of reading.

2.3.1 Single inclusion formulation

First we apply Nyström discretization to a single prototype inclusion and transform its representation from that of boundary potential densities to cylindrical harmonics. There are three motivations for this transformation. For smooth inclusions, the number of discretization nodes is dramatically larger than the number of cylindrical harmonics, which allows us to precompute the transformation for each inclusion shape once and only deal with the cylindrical harmonics representation without increasing the error in the electric field. This reduces the computational cost of the solution to a multiple-scattering problem by several orders of magnitude, and is particularly helpful when multiple iterations of a scattering problem are required for optimization. The second motivation for this representation is that it enables the use of the multiple-scattering translation that we will apply to accelerate

the solution process. Thirdly, cylindrical harmonics are easily rotated and thus only one transformation needs to be calculated for inclusions that are identical up to rotation. Nonetheless, it is difficult to ascertain *a priori* what the optimal number of cylindrical harmonics is for a given inclusion in a multiple-scattering problem, as this number depends not only on the type and frequency of the incident wave but also on the shape of the inclusion and the distance between it and its closest neighboring inclusion. In the past few years some convergence bounds have been developed [38], but in our examples these proved to be highly shape-dependent and not as accurate in the near field, and therefore we relied on a computational approach to determine the optimal number.

One drawback of this transformation is its inability to handle touching or intersecting scattering disks, which are fictitious circles strictly enclosing the inclusions, even if the inclusions themselves are adequately separated. The worst manifestation of this issue would occur with thin and long inclusions whose scattering disks cover a disproportionately large area. However, one can partially overcome this restriction by grouping multiple inclusions in close proximity into one disk and rotating them in unison.

We utilize a layer potentials formulation [39], wherein a single-layer potential density σ and a double-layer potential density μ are assumed to exist on $\partial\Omega$. For notational simplicity, in this section we assume that the inclusion surface Ω is centered at the origin. Note that although we focus only on smooth shapes, if $\partial\Omega$ is not smooth, the method is still applicable with an appropriate discretization approach [40]. These densities have unknown complex amplitudes and give rise to the potential representation

$$u^{\mathrm{s}} = \begin{cases} \mathcal{S}^{k_1}\sigma + \mathcal{D}^{k_1}\mu & \text{in } \Omega, \\ \mathcal{S}^{k_0}\sigma + \mathcal{D}^{k_0}\mu & \text{otherwise} \end{cases} \tag{2.3}$$

for the $\hat{\mathbf{z}}$ component of the scattered electric field, where the single- and double-layer potential operators for wavenumber k are defined by

$$\begin{aligned} \mathcal{S}^k\sigma(\mathbf{r}) &:= \int_{\partial\Omega} G^k(\mathbf{r},\mathbf{r}')\sigma(\mathbf{r}')\,\mathrm{d}\mathbf{r}', \\ \mathcal{D}^k\mu(\mathbf{r}) &:= \int_{\partial\Omega} \frac{\partial G^k}{\partial n_{\mathbf{r}'}}(\mathbf{r},\mathbf{r}')\mu(\mathbf{r}')\,\mathrm{d}\mathbf{r}' \end{aligned} \tag{2.4}$$

and $G^k(\mathbf{r},\mathbf{r}') = \frac{i}{4}H_0^{(1)}(k|\mathbf{r}-\mathbf{r}'|)$ is the two-dimensional Green's function for the Helmholtz equation in a homogeneous material. For a given incident field u^{inc}, the constant-permeability TM_z boundary conditions are applied to the potential formulation. After accounting for the potential density jump across the boundary [41] we have the system

$$\begin{aligned} \mathcal{S}^{k_0}\sigma - \mathcal{S}^{k_1}\sigma + \mathcal{D}^{k_0}\mu - \mathcal{D}^{k_1}\mu + \mu &= -u^{\mathrm{inc}}, \\ \frac{\partial}{\partial n}\left[\left(\mathcal{S}^{k_0} - \mathcal{S}^{k_1}\right)\sigma + \left(\mathcal{D}^{k_0} - \mathcal{D}^{k_1}\right)\mu\right] - \sigma &= -\frac{\partial u^{\mathrm{inc}}}{\partial n} \end{aligned} \tag{2.5}$$

of integral equations which holds for all points $\mathbf{r} \in \partial\Omega$. This system cannot be solved by directly evaluating the operators on the boundary on account of the singularity in G^k and the hypersingularity in its second-order derivative. Hence we split each integrand into two terms, integrating the first term with the Kussmaul-Martensen quadrature rule

and the other with trapezoidal or Gauss-Legendre quadrature. Many other choices for the quadrature rule exist and can be used interchangeably, such as the more sophisticated QBX [42]. Denote the values of the potential densities σ, μ on $2N$ discretization nodes by $\boldsymbol{\sigma}$, $\boldsymbol{\mu}$ respectively. We obtain the system of equations

$$\mathbf{Z}\begin{pmatrix}\boldsymbol{\sigma}\\ \boldsymbol{\mu}\end{pmatrix} = -\begin{pmatrix}u^{\text{inc}}\\ \frac{\partial u^{\text{inc}}}{\partial n}\end{pmatrix}, \tag{2.6}$$

in which $\mathbf{Z}$ is a $4N \times 4N$ matrix which includes all potential operators[1].

In order to expand the potentials in terms of cylindrical harmonics, the system in (2.6) is solved for $2P+1$ incoming waves sampled on the discretization points of the shape, or $u^{\text{inc}} = J_p(k_0|\mathbf{r}|)e^{ip\angle\mathbf{r}}$ for $p = -P, \dots, P$. This yields the single- and double-layer potential density vectors $\boldsymbol{\sigma}_p$, $\boldsymbol{\mu}_p$ for the p-th incident wave. For this solution method to maintain reasonable time complexity, this system should be factorized (e.g. LU) for successive direct solutions, thus requiring $O(N^3 + (2P+1)N^2)$ computations in total.

Let $\mathbf{r}$ be a point that lies strictly outside the inclusion such that $|\mathbf{r}| > |\mathbf{r}'|$ for any $\mathbf{r}'$ on the boundary. We apply Graf's addition theorem for Hankel functions to the integral operator formula for the scattered field given by (2.3) and obtain the cylindrical harmonics expansion

$$\begin{aligned} u^{\text{s}}(\mathbf{r}) &= \sum_{l=-P}^{P} s_{l,p} H_l^{(1)}(k_0|\mathbf{r}|)e^{il\angle\mathbf{r}},\\ s_{l,p} &:= \frac{i}{4}\int_{\partial\Omega} J_l(k_0|\mathbf{r}'|)e^{-il\angle\mathbf{r}'}\sigma_p(\mathbf{r}') + \hat{\mathbf{n}}_{\mathbf{r}'}\cdot\nabla\left[J_l(k_0|\mathbf{r}'|)e^{-il\angle\mathbf{r}'}\right]\mu_p(\mathbf{r}')\,\mathrm{d}\mathbf{r}' \end{aligned} \tag{2.7}$$

of the potential operators. Notably, this expansion only holds strictly outside the inclusion, and thus we assume a fictitious scattering disk D which strictly encloses the inclusion. Inside this disk, the direct integral equation representation is assumed, while outside of it the expansion in (2.7) holds. In this work the diameter of the scattering disks is chosen to be 10% larger than the inclusion diameter. While the diameter of the scattering disk can be reduced if necessary, this typically leads to a dramatic increase in P. Approximating the integral above with the same boundary discretization yields a formula of the form $s_{l,p} = (\mathbf{A}\boldsymbol{\sigma}_p + \mathbf{B}\boldsymbol{\mu}_p)_l$, which in turn yields the entire scattering matrix $\mathbf{X}^{(m)} = \mathbf{A}\boldsymbol{\Sigma} + \mathbf{B}\mathbf{M}$ for the m-th inclusion, where the p-th column of $\boldsymbol{\Sigma}$ is $\boldsymbol{\sigma}_p$ and similarly for $\mathbf{M}$ and $\boldsymbol{\mu}_p$.

As mentioned earlier, the process above only needs to be carried out once per inclusion, up to rotation. The representation of an inclusion rotated by an angle φ_m is readily available by multiplying the (l,p)-th element of $\mathbf{X}^{(m)}$ by a factor of $e^{-i\varphi_m(l-p)}$, in other words, by replacing the scattering matrix with $\boldsymbol{\Phi}\mathbf{X}^{(m)}\boldsymbol{\Phi}^*$ for the diagonal matrix $\boldsymbol{\Phi}_{p,p} = e^{-ip\varphi_m}$.

Now let Ω_m be centered at $\mathbf{o}^{(m)}$ with a local coordinate system $\mathbf{r}^{(m)} = \mathbf{r} - \mathbf{o}^{(m)}$. In order to use the scattering matrix to solve scattering of an incident field u^{inc} from the single m-th inclusion, we first expand u^{inc} as

$$u^{\text{inc}} = \sum_{p=-P}^{P} \alpha_p^{(m)} J_p(k_0|\mathbf{r}^{(m)}|)e^{ip\angle\mathbf{r}^{(m)}}. \tag{2.8}$$

[1] We refer to Appendix A.1 for a detailed derivation of $\mathbf{Z}$ (not part of the original publication).

Due to the Jacobi-Anger expansion in the particular case of plane-wave incidence $e^{i\mathbf{k}\cdot\mathbf{r}}$ for some $\mathbf{k} = (k\cos\theta_i, k\sin\theta_i)$, we have $\alpha_p = e^{ip\left(\pi/2-\theta_i\right)}$ in the local coordinates up to multiplication by a phase constant. The electric field scattered by the inclusion is given by the outgoing expansion

$$u^{\mathrm{s}} = \sum_{p=-P}^{P} \beta_p^{(m)} H_p^{(1)}(k_0|\mathbf{r}^{(m)}|)e^{ip\angle\mathbf{r}^{(m)}}, \tag{2.9}$$

that is, a linear combination of the scattering matrix columns, where in this case $\beta_p^{(m)} = (\mathbf{X}^{(m)}\boldsymbol{\alpha}^{(m)})_p$. Note that circular inclusions can be analytically represented using a diagonal scattering matrix by utilizing orthogonality of the basis functions on a circle. For such an inclusion with radius R, the scattering matrix components are readily given by

$$\beta_p = -\alpha_p \frac{J_p(k_0R)J_p'(k_1R) - J_p'(k_0R)J_p(k_1R)}{H_p^{(1)}(k_0R)J_p'(k_1R) - H_p^{(1)\prime}(k_0R)J_p(k_1R)}, \tag{2.10}$$

where $Z_p'(kR) = k\left(Z_{p-1}(kR) - (p/kR)Z_p(kR)\right)$ for $Z_p = J_p, H_p^{(1)}$.

Two error mechanisms affect the accuracy of the solution beyond the adjustable FMM truncation and quadrature error discussed later in Section 2.3.3. First we have the discretization error due to the finite number of nodes $2N$ on the inclusion boundary, and the second stemming from the transformation to a cylindrical harmonics formulation. We denote by Δu the normalized RMS errors for these error mechanisms. The discretization error is computed as follows: a fictitious line source is assumed at some point inside the inclusion along with an incident plane wave outside of it. The potential densities $\boldsymbol{\sigma}$, $\boldsymbol{\mu}$ on the boundaries $\partial\Omega$ attained from solving the potential density system of (2.6) induce fields outside the inclusion that are equivalent to those of the line source, up to the error that is measured on the scattering disk D. The cylindrical harmonics transformation error is measured by comparing the field induced by the potential densities to that of the cylindrical harmonics on points distanced $2D$ from the inclusion center. Fig. 2.2 shows an example of the relation between N and P and their respective errors for two inclusion shapes, a squircle with $R = 0.35\lambda_0$ and a rounded star with the parametrization

$$\mathbf{r}(\theta) = \left[R + a\cos(5\theta)\right](\cos\theta, \sin\theta), \tag{2.11}$$

with $R = 0.3\lambda_0$, $a = 0.1\lambda_0$. For both inclusions the inner wavenumber is $k_1 = 1.5k_0$. Note that not only is N substantially larger than P for all values of Δu, but the ratio between them continues to grow as the desired errors diminish.

2.3.2 Multiple-scattering formulation

Here we apply the principles used in the preceding section to a multiple-scattering setting. Previously, the relation between incoming and outgoing coefficients was given by the scattering matrix, however, the incident field of a single inclusion in a multiple-scattering scenario is a combination of the incident field and the fields reflected off all other inclusions. A translation matrix is used to transform the reflected field from the local coordinates of one inclusion to the local coordinates of another [28].

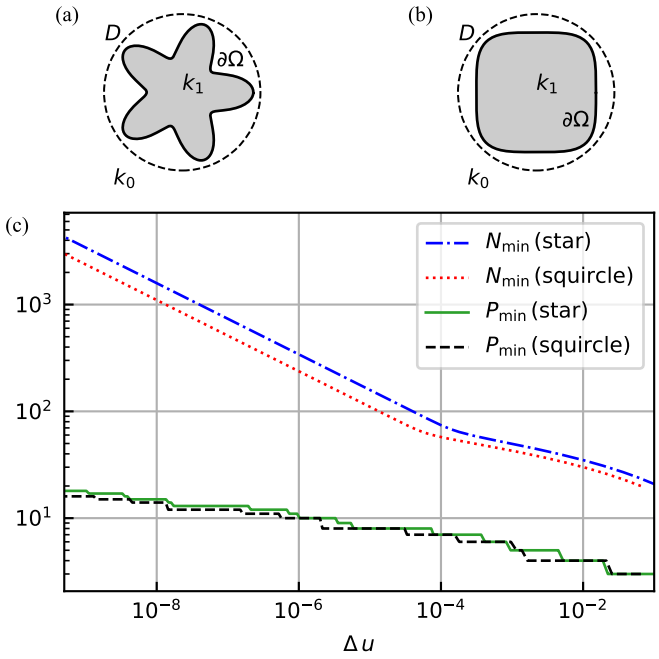

Fig. 2.2: Minimum number of discretization nodes and cylindrical harmonics for two inclusion shapes. (a) Rounded star and its scattering disk D. (b) Squircle and its scattering disk D. (c) Minimum discretization node parameter N and cylindrical harmonics parameter P for given discretization and cylindrical transformation error, respectively, for these two inclusions.

Let $\mathbf{r}^{(m)}$ and $\mathbf{r}^{(m')}$ denote a point in the local coordinates of the m-th and m'-th inclusions, respectively, and let $\mathbf{r}^{(m',m)}$ be the coordinates of the m'-th inclusion with respect to the center of the m-th inclusion. Using Graf's addition formula and truncating the higher-order elements, we obtain the relation between the two local expansions

$$\sum_{p=-P}^{P} \beta_p^{(m)} H_p^{(1)}(k_0|\mathbf{r}^{(m)}|)e^{ip\angle\mathbf{r}^{(m)}} = \sum_{\mu=-P}^{P} J_\mu(k_0|\mathbf{r}^{(m')}|)e^{i\mu\angle\mathbf{r}^{(m')}} \sum_{p=-P}^{P} \beta_p^{(m)} T_{\mu,p}^{(m',m)} \ , \quad (2.12)$$

where $\mathbf{T}^{(m',m)}$ with the elements

$$T_{\mu,p}^{(m',m)} = e^{i(p-\mu)\angle\mathbf{r}^{(m',m)}} H_{p-\mu}^{(1)}(k_0|\mathbf{r}^{(m',m)}|) \quad (2.13)$$

is the translation matrix which translates the outgoing coefficients of one inclusion to the incoming coefficients of another. Summing over the contributions of all the inclusions, we obtain the complete incoming coefficients of the m'-th particle

$$\tilde{\boldsymbol{\alpha}}^{(m')} = \boldsymbol{\alpha}^{(m')} + \sum_{m \neq m'} \mathbf{T}^{(m',m)} \boldsymbol{\beta}^{(m)}. \quad (2.14)$$

Finally, we note that $\boldsymbol{\beta}^{(m')} = \mathbf{X}^{(m')}\tilde{\boldsymbol{\alpha}}^{(m')}$ holds for the complete incoming coefficients, and substitute this relation into (2.14) to obtain

$$\left(\mathbf{X}^{(m')}\right)^{-1}\boldsymbol{\beta}^{(m')} - \sum_{m\neq m'}\mathbf{T}^{(m',m)}\boldsymbol{\beta}^{(m)} = \boldsymbol{\alpha}^{(m')}, \tag{2.15}$$

thus yielding a system of $(2P+1)M$ equations, where M is the number of inclusions. A preconditioned scattering system is obtained when multiplying both sides by the block scattering matrix, which we denote in concatenated form by

$$(\mathbf{I} - \mathbf{X}\mathbf{T})\,\boldsymbol{\beta} = \mathbf{X}\boldsymbol{\alpha}. \tag{2.16}$$

Once the multiple-scattering system in (2.16) is solved, the scattered field at any point outside the scattering disks is readily calculated by summing (2.9) over all inclusions. Strictly inside the inclusions, the field is given by the discretized integral (2.3), where the densities are

$$\boldsymbol{\sigma}^{(m)} = \boldsymbol{\Sigma}\left(\mathbf{X}^{(m)}\right)^{-1}\boldsymbol{\beta}^{(m)} \tag{2.17a}$$

$$\boldsymbol{\mu}^{(m)} = \mathbf{M}\left(\mathbf{X}^{(m)}\right)^{-1}\boldsymbol{\beta}^{(m)}. \tag{2.17b}$$

These are weighted sums of those $\boldsymbol{\sigma}_p$, $\boldsymbol{\mu}_p$ obtained from solving (2.6) for the different incoming waves, as the expansion in (2.9) of the inclusion is not valid inside the scattering disk. Between the m-th inclusion and its disk, the scattered field u^{s} is given by summing (2.9) over all $m' \neq m$ and then adding the direct integral operator for m.

2.3.3 FMM acceleration of the translation

As the computational cost of directly solving (2.16) becomes prohibitively high for a large number of inclusions, this system should be solved iteratively. While applying the block-diagonal scattering matrix $\mathbf{X}$ in each iteration requires only $O(M)$ operations, the translation matrix is almost fully populated and thus requires $O(M^2)$ operations. Therefore, we choose to apply the block translation matrix $\mathbf{T}$ using FMM [32], yielding a lower complexity that will be analyzed in the next section. In this section, we shall succinctly describe the FMM process for this problem. Assume a collection of many inclusions, divided into G non-empty $a \times a$ boxes. The FMM process converts the translation matrix to a sequence of operators. These operators aggregate the translation matrices of multiple inclusions in one box, translate them to a different box and disaggregate them to the inclusions in said box. Note that this process assumes the boxes have some minimal distance between them. For boxes which are closer than this minimal distance, or are the same box, the appropriate blocks of the translation matrix $\mathbf{T}$ are directly applied via a sparse near-interaction matrix. We note that for accurate handling of arbitrarily sized boxes, this approach can be modified to follow the wideband FMM [43]. While the FMM solution of the preconditioned system (2.16) typically converges in reasonable time, this can be accelerated further by using an FMM-based preconditioner [44]. It is also worth remarking that the FMM-accelerated multiple-scattering formulation converges even in the presence of resonant modes [45].

Let the m-, m'-th inclusions which are centered at $\mathbf{o}^{(m)}$, $\mathbf{o}^{(m')}$ be placed in boxes centered at $\mathbf{c}$, $\mathbf{c}'$ respectively. Provided $\mathbf{c}$, $\mathbf{c}'$ are distanced by at least $\sqrt{2}a$, Graf's addition and Bessel's integral theorems are applied to the translation matrix in (2.13), which results in

$$T_{\mu,p}^{(m',m)} = \frac{1}{2\pi}\int_0^{2\pi} e^{i\mathbf{k}\cdot(\mathbf{o}^{(m')}-\mathbf{c}')}\mathcal{F}_\infty(\theta,\mathbf{c}'-\mathbf{c})e^{-i\mathbf{k}\cdot(\mathbf{o}^{(m)}-\mathbf{c})}e^{i(\mu-p)\left(\pi/2-\theta\right)}\,\mathrm{d}\theta, \tag{2.18}$$

where $\mathbf{k} = (k\cos\theta, k\sin\theta)$, and the truncated FMM translation function which transmits plane waves from $\mathbf{c}$ to $\mathbf{c}'$ is defined as

$$\mathcal{F}_{\tilde{P}}(\theta,\mathbf{x}) := \sum_{\xi=-\tilde{P}}^{\tilde{P}} H_\xi^{(1)}(k|\mathbf{x}|)e^{i\xi\left(\angle\mathbf{x}+\pi/2-\theta\right)}. \tag{2.19}$$

Although this translation function must be truncated for practical computations, the series does not converge for small values of $\tilde{P}$ and oscillates for large values, making the optimal choice an extensively-studied, non-trivial problem. Several analytical and empirical formulas have been proposed for this truncation, of which the excess bandwidth formula [46] is used here. Assuming this series truncation, the integral expansion of the Bessel function has finite bandwidth such that a $Q \propto \tilde{P}$-point quadrature of $[0, 2\pi]$ is sufficient. Hence if we define $\mathbf{k}_q := (k\cos\theta_q, k\sin\theta_q)$, the translation matrix is approximated as

$$T_{\mu,n}^{(m',m)} \approx \frac{1}{Q}\sum_{q=1}^{Q} \underbrace{e^{i\mathbf{k}_q\cdot(\mathbf{o}^{(m')}-\mathbf{c}')}e^{i\mu\left(\pi/2-\theta_q\right)}}_{\text{disaggregation}}\mathcal{F}_{\tilde{P}}(\theta_q,\mathbf{c}'-\mathbf{c})\underbrace{e^{-i\mathbf{k}_q\cdot(\mathbf{o}^{(m)}-\mathbf{c})}e^{-in\left(\pi/2-\theta_q\right)}}_{\text{aggregation}}. \tag{2.20}$$

We now construct the FMM matrices used for matrix-vector product acceleration. Denote by M_g the number of inclusions in the g-th box, centered at $\mathbf{c}_g$. We construct a $1 \times M_g$ block aggregation matrix, containing a block for every inclusion, with the m-th block $\mathbf{A}^{(m)}$ given by

$$A_{q,n}^{(m)} := e^{-i\mathbf{k}_q\cdot(\mathbf{o}^{(m)}-\mathbf{c}_g)-in\left(\pi/2-\theta_q\right)}, q = 1,\ldots,Q, \quad n = -P,\ldots,P. \tag{2.21}$$

Since FMM is applied to every box with respect to every other box, we construct the disaggregation matrix by applying the conjugate transpose to the aggregation matrix.

Finally, for each pair (g', g) of sufficiently distant boxes, a diagonal FMM translation matrix $\mathbf{F}^{(g',g)}$ is constructed by

$$F_{q,q}^{(g',g)} := \frac{1}{Q}\mathcal{F}_{\tilde{P}}(\theta_q,\mathbf{c}_{g'}-\mathbf{c}_g), \quad q = 1,\ldots,Q. \tag{2.22}$$

2.3.4 FMM complexity

Complexity analyses for the application of the FMM to various problems are well established, generally leading to a single-level result of $O(N_{\mathrm{dof}}^{1.5})$ and multi-level complexity $O(N_{\mathrm{dof}}\log N_{\mathrm{dof}})$ for N_{dof} degrees of freedom. However, the relationship between the optimal number of boxes and the wavenumber is different in the multiple-scattering approach, and therefore we find it instructive to briefly analyze the complexity of our FMM application.

Since each aggregation matrix is of dimension $Q \times M_g(2P+1)$, performing the aggregation of all G boxes has time complexity $O\left(MQ\,(2P+1)\right)$, and thus so does the total disaggregation. The time complexity of performing all box-to-box FMM translations is $O(QG^2)$, while the number of nonzero elements in the near-interaction matrix is

$$(2P+1)^2\Big[\sum_g M_g(M_g-1)+\sum_g M_g \sum_{(g',g)\text{ near}} M_{g'}\Big]. \tag{2.23}$$

Therefore, applying the near-interaction matrix is expected to require $(2P+1)^2\sum_g[M_g^2+M_g]$ operations. Including the computational cost of applying the scattering and identity matrices, applying the operator $(\mathbf{I}-\mathbf{XT})$ using FMM has time complexity

$$O\Big(MQ(2P+1)+QG^2+M(2P+1)^2+(2P+1)^2\sum_g[M_g^2+M_g]\Big). \tag{2.24}$$

Since the quadrature Q is proportional to the diameter of each box, and in two dimensions the area of a box is inversely proportional to the number of boxes, we have $Q \propto G^{-0.5}$. If we assume an approximately constant distribution of inclusions in boxes such that $M_g \approx M/G$, the FMM time complexity expression is simplified to

$$O\left(G^{1.5}+(2P+1)^2M^2G^{-1}\right). \tag{2.25}$$

We note that while the usual FMM choice $G \propto \sqrt{M}$ yields a complexity of $O(M^{1.5})$, selecting $G = bM^{0.8}$ for a constant b reduces the complexity to $O(M^{1.2})$ per FMM solution with regard to the number of inclusions. In practice, even a choice of $G \propto M$ may be optimal due to the quadratic dependence of the second complexity term on the wavelength. An analogous analysis of a Multi-Level Fast Multipole Algorithm approach will lead to asymptotic complexity of $O(M)$ [29], although this is only beneficial in practice for very large values of M.

2.4 Optimization for multiple-scattering features

We give a description of a general optimization problem that is applicable to various metamaterials, where our aim is to provide a template for applying our framework to different structures. Given an objective function as in (2.2), we develop its gradient, and show how it can be computed in order to find optimal parameters for the overall structure. Our I points of interest $\mathbf{r}_i$ are assumed to lie outside all scattering disks, as points inside them complicate and slow down the optimization procedure. Note that whether we are minimizing or maximizing the objective function is immaterial, as maximization problems can be solved by minimizing the negated objective function and again negating the achieved minimum value. Simultaneously minimizing intensity at several points while maximizing it at others is achieved by appropriately weighting the objective function. For convenience, we rewrite the field values in the objective function in terms of $\boldsymbol{\beta}$ and obtain the column vector $\mathbf{u} = \mathbf{H}^\top\boldsymbol{\beta} + \mathbf{u}^{\text{inc}}$ and the simplified form $f_{\text{obj}} = \|\mathbf{u}\|^2$, where $\mathbf{H}$ relates the coefficient solution to the objective function.

Let $\mathbf{w}$ denote a vector of J inclusion parameters, where we assume each parameter affects the shape of an inclusion, but not the location of its center, and therefore $\mathbf{H}$ remains constant. In order to calculate the gradient ∇f_{obj} with respect to $\mathbf{w}$, we shall use the adjoint-state method [36, 37], as its complexity is less dependent on the number of design variables than a direct approach. Our optimization problem is given by

$$\begin{aligned} \min_{\mathbf{w}} \quad & f_{\text{obj}}(\boldsymbol{\beta}) = \|\mathbf{H}^\top \boldsymbol{\beta} + \mathbf{u}^{\text{inc}}\|^2 \\ \text{s.t.} \quad & \mathbf{c}(\boldsymbol{\beta}, \mathbf{w}) = \left[\mathbf{I} - \mathbf{X}(\mathbf{w})\mathbf{T}\right] \boldsymbol{\beta} - \mathbf{X}(\mathbf{w})\boldsymbol{\alpha} = 0, \end{aligned} \tag{2.26}$$

where the constraint ensures that $\boldsymbol{\beta}$ is a solution to the multiple-scattering problem. To apply the adjoint-state method, we utilize a complex vector $\boldsymbol{\lambda}$ to define the Lagrangian

$$\Lambda = f_{\text{obj}} + \boldsymbol{\lambda}^\top \mathbf{c} + \overline{\boldsymbol{\lambda}^\top \mathbf{c}}, \tag{2.27}$$

equate the complete derivatives of f_{obj} and Λ with respect to $w \in \mathbf{w}$, and have after some algebraic manipulation that

$$\frac{\mathrm{d}f_{\text{obj}}}{\mathrm{d}w} = 2\Re\Big(\Big[\frac{\partial f_{\text{obj}}}{\partial \boldsymbol{\beta}} + \boldsymbol{\lambda}^\top (\mathbf{I} - \mathbf{X}\mathbf{T}) \Big] \frac{\partial \boldsymbol{\beta}}{\partial w} \Big) - 2\Re\Big(\boldsymbol{\lambda}^\top \frac{\partial \mathbf{X}}{\partial w} \mathbf{X}^{-1} \boldsymbol{\beta} \Big). \tag{2.28}$$

The crux of the adjoint-state method resides in setting the first summand to zero by properly solving for $\boldsymbol{\lambda}$. This will allow us to calculate the derivative without explicitly computing $\partial\boldsymbol{\beta}/\partial\mathbf{w}$ which would add significant complexity. Substituting f_{obj} yields the adjoint system

$$\left(\mathbf{I} - \mathbf{T}^\top \mathbf{X}^\top\right) \boldsymbol{\lambda} = -\mathbf{H}\bar{\mathbf{u}}, \tag{2.29}$$

which we solve using a modified FMM procedure with the same complexity, as detailed in the Appendix. Once the system is solved, each element of the gradient can be calculated in $O((2P+1)^2)$ time, yielding $O(M(2P+1)^2) + O(\text{FMM})$ complexity in total if each inclusion is affected by a single parameter. A description of the complete process of automatically designing a structure via our approach is summarized in Algorithm 2.1. The specifics depend on the optimization method used, where additional evaluations of f_{obj} might be necessary for the optimization line search. We note that $\mathbf{X}^{-1}$ was computed in a previous step and its use here is not problematic, and in any event $\mathbf{X}^{-1}\boldsymbol{\beta}$ can be replaced with $\mathbf{T}\boldsymbol{\beta} + \boldsymbol{\alpha}$.

In this work, we optimize inclusion parameters for which $\nabla_{\mathbf{w}}\mathbf{X}$ is analytic, such as the rotation angle of an arbitrary inclusion and the radius of a circular inclusion, which significantly simplifies the computation of the gradient. Attempting to optimize parameters that do change the structure of $\mathbf{X}$ is more involved, and may require numerical differentiation.

2.5 Numerical results

In this section, we demonstrate our approach using three examples. First, we study the run time of the multiple-scattering approach for increasingly numerous inclusions. Additionally, we apply the optimization process in its entirety to two practical examples, resulting in improved designs. In what follows, all values of $2N$, the number of discretization nodes, and P, the cylindrical harmonics parameter, are chosen to be the minimal values for which

Algorithm 2.1 Automated design of dielectric metamaterials

1: $\mathbf{w} \leftarrow (w_1, \ldots, w_J)$ // `optimization starting point`
   `// Precomputation phase`
2: **for** all distinct non-circular inclusions **do**
3: Construct and solve potential density equation (2.6) for $-P, \ldots, P$
4: **end for**
5: Prepare FMM matrices // `using the development in Section 2.3.3`
6: **repeat**
7: Calculate $\mathbf{X}(\mathbf{w})$
8: $\boldsymbol{\beta} \leftarrow$ solution of multiple-scattering equation (2.16) with FMM
9: Calculate $f_{\text{obj}}(\boldsymbol{\beta})$
   `// Construct gradient:`
10: Solve adjoint system of (2.29) for $\boldsymbol{\lambda}$ using transposed FMM
11: **for** $w_j \in \mathbf{w}$ **do**
12: Compute j-th component of ∇f_{obj} using (2.28)
13: **end for**
14: $\mathbf{w} \leftarrow$ next optimization point
15: **until** optimization has converged

an electric field error of 10^{-6} holds, as explained in Section 2.3. All linear systems solved via FMM use GMRES [47] with tolerance 10^{-6} as the underlying iterative method. All simulations were written in the Julia programming language [48], and run on a 3.4GHz Intel Core i7-6700 CPU with 32GB of memory.

2.5.1 Complexity of multiple-scattering approach

We examine the run time of the multiple-scattering algorithm for a square grid of inclusions, and compare it to the theoretical complexity analysis in Section 2.3.4. Fig. 2.3 depicts the run time of solving the multiple-scattering equation (2.16) using FMM for several values of M. Here an incident plane wave is scattered by a $\sqrt{M} \times \sqrt{M}$ grid of identical rounded stars with the parametrization previously seen in (2.11), each randomly rotated. The inclusion parameters are $R = 0.3\lambda_0$, $a = 0.1\lambda_0$ and $k_1 = 1.5k_0$, and are distanced $0.9\lambda_0$. The minimal values of N and P for $\Delta u = 10^{-6}$ and this inclusion are $N = 342$ and $P = 10$. The precomputation of the prototype inclusion for these values was performed once for all simulations and required 0.9 s that were not included in the plot. A single matrix-vector product scales almost linearly with the number of inclusions, in accordance with the complexity analysis. The total solution convergence time has complexity $O(M^{2.3})$, i.e., the number of iterations depends on the number of inclusions, which is not uncommon when solving electromagnetic systems of equations with Krylov subspace methods. Nonetheless, the total solution time is several orders of magnitude below that achievable by a naive method.

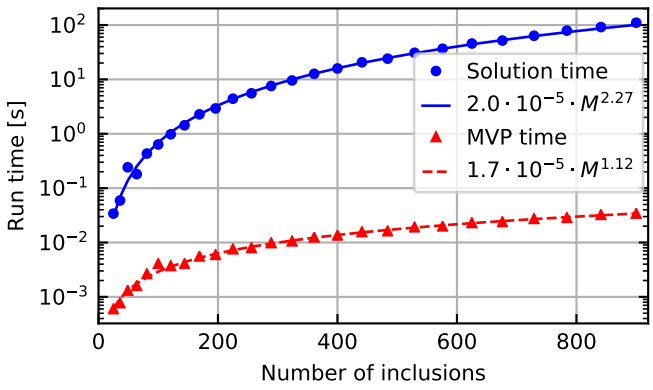

Fig. 2.3: Run time of the multiple-scattering system solution, as well as of a single matrix-vector product, for different numbers of rounded-star inclusions.

2.5.2 Rotation-angle optimization for arbitrary inclusions

For our first optimization example, we apply our framework to the optimization of inclusion rotation. That is, given an incident wave with wavelength λ_0 scattered by a collection of M inclusions, we wish to find the optimal rotation angles $\boldsymbol{\varphi}$ of the inclusions such that the field propagation in some desired direction is maximized.

The derivatives of the scattering matrices with respect to the rotation angles are given by

$$\left(\frac{\partial \mathbf{X}^{(m)}}{\partial \varphi_j}\right)_{u,v} = -i\delta_{m,j}(u-v)\left(\mathbf{X}^{(m)}\right)_{u,v} = \delta_{m,j}\left(\mathbf{D}\mathbf{X}^{(m)} - \mathbf{X}^{(m)}\mathbf{D}\right)_{u,v}, \tag{2.30}$$

where $(\mathbf{D})_{u,v} = -\delta_{u,v} iu$. Since the rotation angles are unconstrained, our choice of optimization method is the Broyden-Fletcher-Goldfarb-Shanno (BFGS) [49] algorithm, which is a quasi-Newton method that locally approximates the objective function as a quadratic. In each iteration, once the descent direction is decided via the gradient, a line search is necessary to determine the step size to the minimum in that direction. The backtracking line search based on the Armijo-Goldstein condition [50], which minimizes gradient evaluations, is used here. In Fig. 2.4, we simulate the case of a $\hat{\mathbf{y}}$-traveling plane wave incident upon a collection of $M = 100$ inclusions, randomly positioned in a $21\lambda_0 \times 7\lambda_0$ rectangle such that the scattering disks do not intersect. Inclusions are rounded stars with the same size as in Fig. 2.2, have wavenumber $k_1 = 3k_0$ (i.e. the refractive index is $n = 3$), and use the minimal parameters $N = 934$, $P = 12$. The objective function is set as in (2.2) for $I = 20$ points of interest $\mathbf{r}_i$ located equidistantly along the top boundary of the rectangle, which are indicated with white dots. The field amplitude at the points of interest $\mathbf{r}_i$ is substantially larger after the optimization process, whose convergence is shown in detail in Fig. 2.5. Specifically, the BFGS method converges to an average field magnitude of 1.43 at $\mathbf{r}_i$ (in the RMS sense), up from the initial value of 0.48 for $\boldsymbol{\varphi} = 0$, a 200% increase. The process required 127 iterations and 664 seconds for the convergence criterion $\Delta f_{\text{obj}} < 10^{-6}$. We note that setting the starting point to $\varphi_i = \pi$ for each inclusion causes the optimization process to converge to a slightly worse result, with an average field magnitude of 1.41, and dramatically different rotation angles at convergence. Complex optimization problems such as those described

here may have several local extrema, leading to a dependence on the starting point for gradient-based methods. This can be overcome by utilizing hybrid methods, which combine a global search with gradient-based local searches [51].

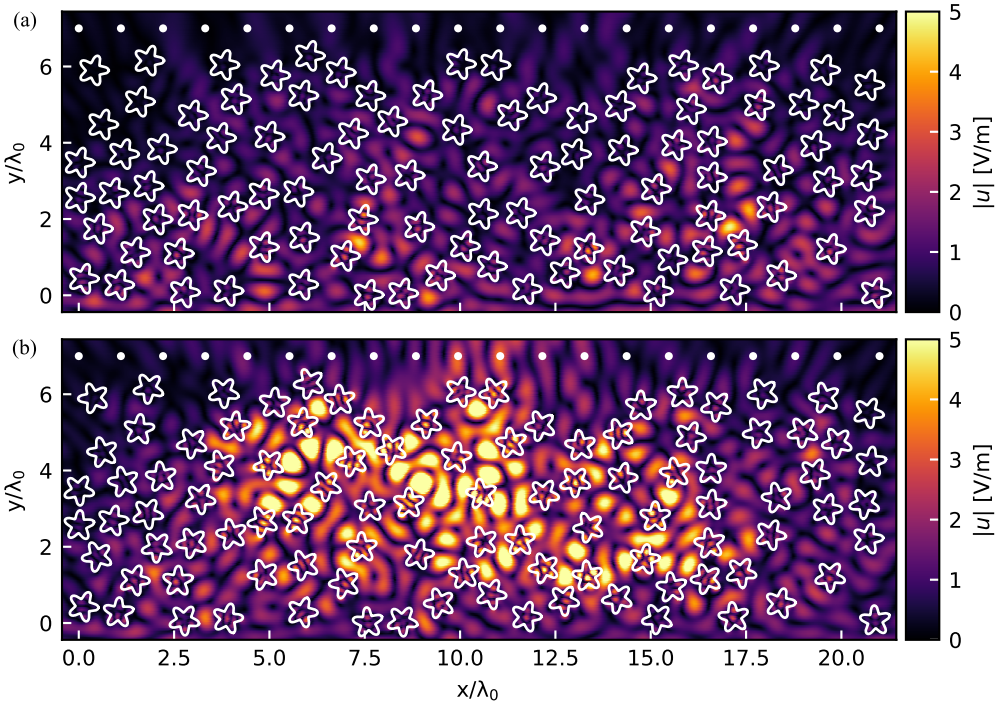

Fig. 2.4: Optimization of rotation angles. (a) Initial electric field amplitude after scattering by $M = 100$ randomly positioned identical rounded stars with zero rotation, which prevent the $\hat{\mathbf{y}}$-traveling plane wave from propagating in its original direction. (b) Electric field amplitude for the same inclusions, with rotation angles optimized to maximize field at 20 points along the top boundary. Markers indicate points where the field is maximized.

2.5.3 Radius optimization for circular inclusions

We now consider optimization of the radii of circular inclusions, where in contrast to the previous example, both the scattering matrices and their derivatives with respect to the inclusion radius are diagonal and have analytical form. This example is motivated by the photonic crystal implementation of the Luneburg lens. The two-dimensional Luneburg lens [52] is a symmetric circular lens designed such that incoming plane waves are focused to a single point on its rim, and no waves are reflected. This property is achieved by a continuously varying refractive index given by the analytic solution $n(r) = \sqrt{2 - (r/R_{\text{lens}})^2}$, where r is the distance from the center of the lens, which has radius R_{lens}. One way of fabricating a Luneburg lens is via long dielectric rods on a glass substrate, which, if long enough, can be assumed to be infinite. Thus the electromagnetic propagation through the device can be treated as a two-dimensional problem. In this setting, the lens is divided into

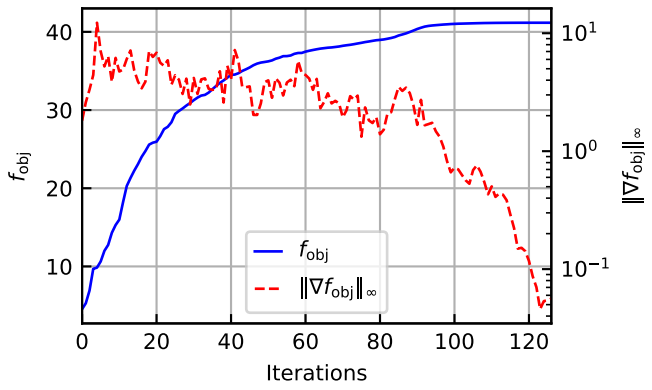

Fig. 2.5: Convergence behavior of the objective function f_{obj} and its gradient ∇f_{obj} for Fig. 2.4.

unit cells on a square grid, each with side length a. Each unit cell m contains a circular inclusion with the same relative permittivity ε_r but differing radius R_m, such that the effective refractive index in the cell can be approximated analytically if a/λ_0 is sufficiently small [53], and thus the radii are set such that the average permittivity approximates the Luneburg solution.

This implementation of the Luneburg lens begs the question whether the electromagnetic focusing could be improved by sacrificing the rotational symmetry of the device, however, note that the restriction to a square grid has already limited this symmetry. To answer this question, we propose optimizing over the radii of the inclusions to maximize the field amplitude at the focal point. Note that since the inclusions are circular, the computation of the gradient is cheaper than in the previous example, as is applying the diagonal scattering matrix in each FMM iteration. Care must be taken to assure that the computed radii are neither below some non-negative lower practical limit $R_{\min}$ nor above the limit $R_{\max}$ at which they are too close for the multiple-scattering approximation in this work, i.e. $0.45a$. Thus unconstrained optimization methods such as BFGS are no longer an option. Fortunately, these so-called box constraints are simple enough to be tackled by the addition of a penalty term which sharpens the constraint from one BFGS run to the next.

In Fig. 2.6, we consider focusing of an $\hat{\mathbf{x}}$-traveling plane wave to the focal point $(R_{\text{lens}}, 0)$ on the lens rim. In this example, there are 316 circular inclusions with relative permittivity $\varepsilon_r = 4.5$, placed on a square grid with lattice constant $a = 0.2\lambda_0$. The total lens radius is $R_{\text{lens}} = 10a$, while the cylindrical harmonics parameter is $P = 5$, and the initial guess is $R_m = a/4$ for all inclusions. The penalized BFGS algorithm converged to a local maximum of $f_{\text{obj}} = 26.36$ after 113 total iterations and 173 seconds, with the convergence criterion $\Delta R < 10^{-6}$, as shown in Fig. 2.7. As this optimization problem is bounds-constrained, convergence of the gradient is not a necessary condition, motivating the use of a step-size convergence criterion instead. Visualization 1 shows the electric field amplitude throughout the optimization process in video form, where the gradual evolution of the optimized device is clearly visible.

The optimization process yields a device that focuses the incoming electric field substantially better than the Luneburg lens, improving upon the Luneburg design by an

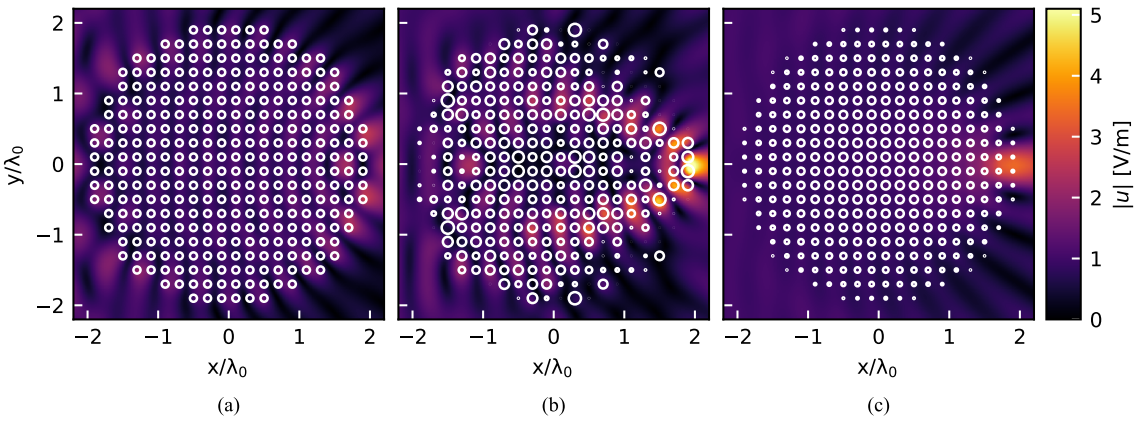

Fig. 2.6: Radius optimization of 316 circular inclusions with $\varepsilon_r = 4.5$ for focusing an $\hat{\mathbf{x}}$-traveling plane wave to a single focal point on the lens rim. Electric field amplitude for (a) starting point, (b) optimized device, and (c) Luneburg lens approximation.

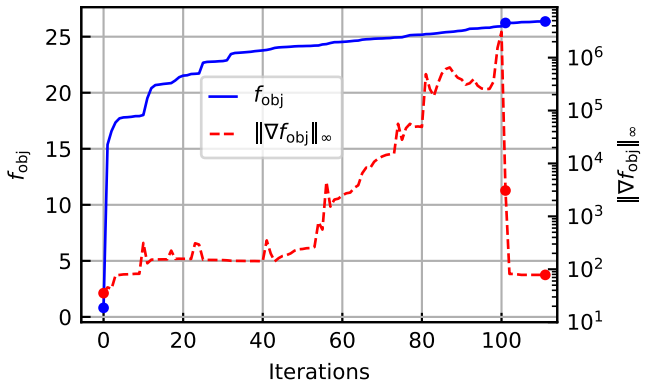

Fig. 2.7: Convergence progress of f_{obj} and its gradient norm for Fig. 2.6 as a function of the penalized BFGS iteration. Markers indicate the beginning of an outer iteration.

amplitude factor of 1.55. Additionally, the optimized design is more intricate than typical intuitive approximations, thus corroborating our promotion of an automated approach. Interestingly, the algorithm produced symmetric radii with respect to the x axis, although this was not an optimization constraint. Applying this constraint, thereby halving the optimization variables, yields a similar result in only 81 seconds, less than half of the time required originally. The optimized device is more susceptible than the Luneburg device to manufacturing variations, with a gradient norm of 78.3, vs. 68.4 for the Luneburg device. However, due to the significant improvement in performance we posit that the optimized device will outperform even with small radius perturbations.

2.6 Conclusion

We proposed and implemented an automated approach for designing dielectric metamaterials with desired electromagnetic properties. Our approach uses gradient-based optimization that provides quick and reliable convergence as well as a fast boundary integral equation solver for precisely computing the field at any point. This method reduces the need for manual trial and error in the design of certain metamaterials by replacing it with rigorous optimization. Our approach should be especially attractive in designing photonic crystals, metalenses, and other devices composed of many substructures whose large number of design parameters would typically render optimal manual design impossible. Although optimization may superficially seem prohibitively expensive for these high-dimensional design problems, our fast solution method makes it practical. The examples in this paper resulted in highly irregular structures, which conforms to observations previously made in [19], where the authors note that aperiodic structures are capable of providing more functionality than their periodic counterparts. In the future, we will extend this approach to objectives containing other functions of the electric field, such as the magnetic field and power flow. Additionally, this approach should be extendable to multi-frequency objectives, such as those necessary for broadband or filtering operations. We implemented the methods described in this paper for the publicly available open-source software package ParticleScattering.jl [54] in the Julia programming language [48], which also includes the examples presented here.

Appendix: Transposed single-level FMM for adjoint method

Let $\mathbf{T} \in \mathbb{C}^{N\times N}$ be the matrix we wish to apply with FMM, divided into G groups or boxes, and let the subscript g denote the section of a vector or matrix pertaining to the g-th group. The double subscript g, g' denotes a matrix operating from the g'-th group to g. Then we can ordinarily write with single-level FMM

$$(\mathbf{T}\mathbf{x})_g = \sum_{g'=1\ldots G} \mathbf{T}_{g,g'}\mathbf{x}_{g'} = (\mathbf{Z}\mathbf{x})_g + \mathbf{D}_g \sum_{g':g,g' \text{ far}} \mathbf{F}_{g,g'}\mathbf{A}_{g'}\mathbf{x}_{g'}, \tag{2.31}$$

where $\mathbf{Z}, \mathbf{D}, \mathbf{F}, \mathbf{A}$ are the near-field, disaggregation, diagonal translation, and aggregation matrices. For the transposed FMM, we can similarly derive

$$\begin{aligned}
(\mathbf{T}^\top\mathbf{x})_g &= \sum_{g'=1\ldots G} (\mathbf{T}^\top)_{g,g'}\mathbf{x}_{g'} = \sum_{g'=1\ldots G} \mathbf{T}^\top_{g',g}\mathbf{x}_{g'} \\
&= \sum_{g':g,g' \text{ near}} \mathbf{Z}^\top_{g',g}\mathbf{x}_{g'} + \sum_{g':g,g' \text{ far}} \left(\mathbf{D}_{g'}\mathbf{F}_{g',g}\mathbf{A}_g\right)^\top \mathbf{x}_{g'} \\
&= (\mathbf{Z}^\top\mathbf{x})_g + \sum_{g':g,g' \text{ far}} \mathbf{A}_g^\top \mathbf{F}_{g',g}\mathbf{D}^\top_{g'}\mathbf{x}_{g'} \\
&= (\mathbf{Z}^\top\mathbf{x})_g + \mathbf{A}_g^\top \sum_{g':g,g' \text{ far}} \mathbf{F}_{g',g}\mathbf{D}^\top_{g'}\mathbf{x}_{g'}.
\end{aligned} \tag{2.32}$$

Since in our case $\mathbf{D}_g = \mathbf{A}_g^H$, applying the transposed FMM is similar to the standard FMM with identical complexity.

Bibliography

[1] S. Jahani and Z. Jacob, "All-dielectric metamaterials," *Nature Nanotechnology*, vol. 11, no. 1, pp. 23–36, 2016.

[2] Y. Yang, W. Wang, P. Moitra, I. I. Kravchenko, D. P. Briggs, and J. Valentine, "Dielectric meta-reflectarray for broadband linear polarization conversion and optical vortex generation," *Nano Letters*, vol. 14, no. 3, pp. 1394–1399, 2014.

[3] P. Moitra, B. A. Slovick, W. Li, I. I. Kravchencko, D. P. Briggs, S. Krishnamurthy, and J. Valentine, "Large-scale all-dielectric metamaterial perfect reflectors," *ACS Photonics*, vol. 2, no. 6, pp. 692–698, 2015.

[4] E. Yablonovitch, "Photonic crystals," *Journal of Modern Optics*, vol. 41, no. 2, pp. 173–194, 1994.

[5] J. D. Joannopoulos, S. G. Johnson, J. N. Winn, and R. D. Meade, *Photonic Crystals: Molding the Flow of Light*. Princeton University Press, 2011.

[6] E. Yablonovitch, T. J. Gmitter, and K. M. Leung, "Photonic band structure: The face-centered-cubic case employing nonspherical atoms," *Physical Review Letters*, vol. 67, pp. 2295–2298, Oct. 1991.

[7] M. D. Turner, M. Saba, Q. Zhang, B. P. Cumming, G. E. Schröder-Turk, and M. Gu, "Miniature chiral beamsplitter based on gyroid photonic crystals," *Nature Photonics*, vol. 7, no. 10, pp. 801–805, 2013.

[8] M. P. C. Taverne, Y.-L. D. Ho, X. Zheng, S. Liu, L.-F. Chen, M. Lopez-Garcia, and J. G. Rarity, "Modelling defect cavities formed in inverse three-dimensional rod-connected diamond photonic crystals," *EPL*, vol. 116, no. 6, p. 64007, 2016.

[9] E. Yablonovitch, "Photonic bandgap based designs for nano-photonic integrated circuits," in *International Electron Devices Meeting (IEDM'02)*, pp. 17–20, IEEE, 2002.

[10] F. Cuesta-Soto, A. Martínez, J. García, F. Ramos, P. Sanchis, J. Blasco, and J. Martí, "All-optical switching structure based on a photonic crystal directional coupler," *Optics Express*, vol. 12, pp. 161–167, Jan. 2004.

[11] M. Khorasaninejad and F. Capasso, "Metalenses: Versatile multifunctional photonic components," *Science*, vol. 358, no. 6367, 2017.

[12] M. Khorasaninejad, W. Chen, A. Zhu, J. Oh, R. Devlin, D. Rousso, and F. Capasso, "Multispectral chiral imaging with a metalens," *Nano Letters*, vol. 16, no. 7, pp. 4595–4600, 2016.

[13] A. Arbabi, E. Arbabi, S. M. Kamali, Y. Horie, S. Han, and A. Faraon, "Miniature optical planar camera based on a wide-angle metasurface doublet corrected for monochromatic aberrations," *Nature Communications*, vol. 7, p. 13682, 2016.

[14] N. Yu and F. Capasso, "Optical metasurfaces and prospect of their applications including fiber optics," *Journal of Lightwave Technology*, vol. 33, pp. 2344–2358, June 2015.

[15] N. Yu and F. Capasso, "Flat optics with designer metasurfaces," *Nature Materials*, vol. 13, pp. 139–150, 2014.

[16] D. C. Dobson, "Optimal design of periodic antireflective structures for the Helmholtz equation," *European Journal of Applied Mathematics*, vol. 4, no. 4, pp. 321–339, 1993.

[17] C. A. Bauer, G. R. Werner, and J. R. Cary, "Truncated photonic crystal cavities with optimized mode confinement," *Journal of Applied Physics*, vol. 104, no. 5, p. 053107, 2008.

[18] Y. Cao, J. Xie, Y. Liu, and Z. Liu, "Modeling and optimization of photonic crystal devices based on transformation optics method," *Optics Express*, vol. 22, no. 3, pp. 2725–2734, 2014.

[19] P. Seliger, M. Mahvash, C. Wang, and A. F. J. Levi, "Optimization of aperiodic dielectric structures," *Journal of Applied Physics*, vol. 100, no. 3, p. 034310, 2006.

[20] D. Bertsimas, O. Nohadani, and K. M. Teo, "Robust optimization in electromagnetic scattering problems," *Journal of Applied Physics*, vol. 101, no. 7, p. 074507, 2007.

[21] E. Bor, M. Turduev, U. G. Yasa, H. Kurt, and K. Staliunas, "Asymmetric light transmission effect based on an evolutionary optimized semi-dirac cone dispersion photonic structure," *Physical Review B*, vol. 98, p. 245112, Dec. 2018.

[22] D. Gagnon, J. Dumont, and L. J. Dubé, "Multiobjective optimization in integrated photonics design," *Optics Letters*, vol. 38, pp. 2181–2184, July 2013.

[23] B. Karaosmanoğlu, H. Eray, and Ö. Ergül, "Full-wave optimization of three-dimensional photonic-crystal structures involving dielectric rods," *Journal of the Optical Society of America A*, vol. 35, pp. 1103–1113, July 2018.

[24] G. Bao and D. C. Dobson, "Modeling and optimal design of diffractive optical structures," *Surveys on Mathematics for Industry*, vol. 8, no. 1, pp. 37–62, 1998.

[25] C. Y. Kao, S. Osher, and E. Yablonovitch, "Maximizing band gaps in two-dimensional photonic crystals by using level set methods," *Applied Physics B*, vol. 81, pp. 235–244, July 2005.

[26] J. Lu and J. Vučković, "Nanophotonic computational design," *Optics Express*, vol. 21, pp. 13351–13367, June 2013.

[27] H. Isakari, K. Nakamoto, T. Kitabayashi, T. Takahashi, and T. Matsumoto, "A multi-objective topology optimisation for 2D electro-magnetic wave problems with the level set method and BEM," *European Journal of Computational Mechanics*, vol. 25, no. 1–2, pp. 165–193, 2016.

[28] N. A. Gumerov and R. Duraiswami, "A scalar potential formulation and translation theory for the time-harmonic Maxwell equations," *Journal of Computational Physics*, vol. 225, no. 1, pp. 206–236, 2007.

[29] J. Lai, M. Kobayashi, and L. Greengard, "A fast solver for multi-particle scattering in a layered medium," *Optics Express*, vol. 22, pp. 20481–20499, Aug. 2014.

[30] D. Colton and R. Kress, *Integral Equation Methods in Scattering Theory*. New York: Wiley, 1983.

[31] M. Lax, "Multiple scattering of waves," *Reviews of Modern Physics*, vol. 23, pp. 287–310, Oct. 1951.

[32] R. Coifman, V. Rokhlin, and S. Wandzura, "The fast multipole method for the wave equation: a pedestrian prescription," *IEEE Antennas and Propagation Magazine*, vol. 35, pp. 7–12, June 1993.

[33] L. Gurel and W. C. Chew, "On the connection of T matrices and integral equations," in *Antennas and Propagation Society Symposium 1991 Digest*, vol. 3, pp. 1624–1627, June 1991.

[34] P. A. Martin, "On connections between boundary integral equations and T-matrix methods," *Engineering Analysis with Boundary Elements*, vol. 27, no. 7, pp. 771–777, 2003.

[35] Z. Gimbutas and L. Greengard, "Fast multi-particle scattering: A hybrid solver for the Maxwell equations in microstructured materials," *Journal of Computational Physics*, vol. 232, no. 1, pp. 22–32, 2013.

[36] G. Chavent, "Identification of functional parameters in partial differential equations," in *Joint Automatic Control Conference*, no. 12, pp. 155–156, 1974.

[37] A. Michaels and E. Yablonovitch, "Leveraging continuous material averaging for inverse electromagnetic design," *Optics Express*, vol. 26, p. 31717, Nov. 2018.

[38] M. Ganesh, S. C. Hawkins, and R. Hiptmair, "Convergence analysis with parameter estimates for a reduced basis acoustic scattering T-matrix method," *IMA Journal of Numerical Analysis*, vol. 32, no. 4, pp. 1348–1374, 2012.

[39] V. Rokhlin, "Solution of acoustic scattering problems by means of second kind integral equations," *Wave Motion*, vol. 5, no. 3, pp. 257–272, 1983.

[40] J. Bremer, V. Rokhlin, and I. Sammis, "Universal quadratures for boundary integral equations on two-dimensional domains with corners," *Journal of Computational Physics*, vol. 229, no. 22, pp. 8259–8280, 2010.

[41] R. Kress, "On the numerical solution of a hypersingular integral equation in scattering theory," *Journal of Computational and Applied Mathematics*, vol. 61, no. 3, pp. 345 – 360, 1995.

[42] A. Klöckner, A. Barnett, L. Greengard, and M. O'Neil, "Quadrature by expansion: A new method for the evaluation of layer potentials," *Journal of Computational Physics*, vol. 252, no. Supplement C, pp. 332–349, 2013.

[43] H. Cheng, W. Crutchfield, Z. Gimbutas, L. Greengard, J. Huang, V. Rokhlin, N. Yarvin, and J. Zhao, "Remarks on the implementation of wideband FMM for the Helmholtz equation in two dimensions," *Contemporary Mathematics*, vol. 408, pp. 99–110, 2006.

[44] N. A. Gumerov and R. Duraiswami, "Computation of scattering from clusters of spheres using the fast multipole method," *The Journal of the Acoustical Society of America*, vol. 117, no. 4, pp. 1744–1761, 2005.

[45] Y. J. Zhang and E. P. Li, "Fast multipole accelerated scattering matrix method for multiple scattering of a large number of cylinders," *Progress in Electromagnetics Research*, vol. 72, pp. 105–126, 2007.

[46] W. C. Chew, E. Michielssen, J. M. Song, and J. M. Jin, *Fast and Efficient Algorithms in Computational Electromagnetics*. Norwood, MA, USA: Artech House, Inc., 2001.

[47] Y. Saad and M. H. Schultz, "GMRES: A generalized minimal residual algorithm for solving nonsymmetric linear systems," *SIAM Journal on Scientific and Statistical Computing*, vol. 7, no. 3, pp. 856–869, 1986.

[48] J. Bezanson, A. Edelman, S. Karpinski, and V. B. Shah, "Julia: A fresh approach to numerical computing," *SIAM Review*, vol. 59, no. 1, pp. 65–98, 2017.

[49] J. Nocedal and S. Wright, *Numerical Optimization*. Springer-Verlag New York, 2 ed., 2006.

[50] L. Armijo, "Minimization of functions having Lipschitz continuous first partial derivatives," *Pacific Journal of Mathematics*, vol. 16, no. 1, pp. 1–3, 1966.

[51] J. Liu, S. Zhang, C. Wu, J. Liang, X. Wang, and K. L. Teo, "A hybrid approach to constrained global optimization," *Applied Soft Computing*, vol. 47, pp. 281–294, 2016.

[52] M. Born and E. Wolf, *Principles of Optics: Electromagnetic Theory of Propagation, Interference and Diffraction of Light*. New York: Pergamon Press, 6 ed., 1980.

[53] S. Takahashi, C.-H. Chang, S. Y. Yang, and G. Barbastathis, "Design and fabrication of dielectric nanostructured Luneburg lens in optical frequencies," in *2010 International Conference on Optical MEMS and Nanophotonics*, pp. 179–180, Aug. 2010.

[54] B. Blankrot and C. Heitzinger, "ParticleScattering: Solving and optimizing multiple-scattering problems in Julia," *Journal of Open Source Software*, vol. 3, p. 691, May 2018.

3 ParticleScattering: Solving and optimizing multiple-scattering problems in Julia

Authored by Boaz Blankrot and Clemens Heitzinger.
Published in *Journal of Open Source Software*, vol. 3, no. 25, p. 691, May 2018. doi: 10.21105/joss.00691

Summary

ParticleScattering (`https://github.com/bblankrot/ParticleScattering.jl`) is a Julia [1] package for computing the electromagnetic fields scattered by a large number of two-dimensional particles, as well as optimizing particle parameters for various applications. Such problems naturally arise in the design and analysis of metamaterials, including photonic crystals [2]. Unlike most solvers for these problems, ours does not require a periodic structure and is scalable to a large number of particles. In particular, this software is designed for scattering problems involving TM plane waves impinging on a collection of homogeneous dielectric particles with arbitrary smooth shapes. Our code performs especially well when the number of particles is substantially larger than the number of distinct shapes, where particles are considered indistinct if they are identical up to rotation.

Solver overview

Given a scattering problem consisting of a collection of penetrable particles in a homogeneous medium, the software performs the following steps to calculate the total electric field:

- For each distinct non-circular shape, a single- and double-layer potential formulation is constructed.
- The potential formulations are transformed to a multipole basis of Hankel functions, reducing the degrees of freedom by at least an order of magnitude.
- Analytical multipole basis is computed for circular particles.
- A multiple-scattering system of equations is constructed, and then solved with the Fast Multipole Method.
- Electric field is computed at any point of interest.

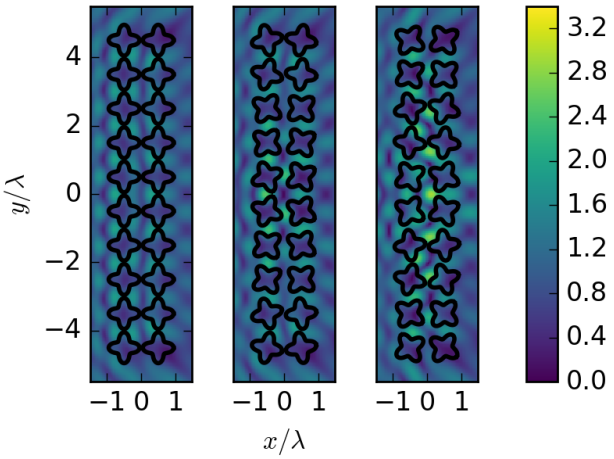

Fig. 3.1: Scattering problem before optimization, after minimization, and after maximization.

In addition, ParticleScattering can plot near- and far-field results using the popular framework PyPlot, create publication-level plots with PGFPlots integration, and compute minimum parameters for a desired error level.

Optimization

ParticleScattering is especially targeted at users who wish to design metamaterials belonging to the class described above. While the large number of variables such metamaterials contain allows for a variety of devices that meet different objectives, it also creates a large search space for choosing them. Therefore, a fast and automated approach can be beneficial for both inventing new designs and improving existing ones. As the results of many ParticleScattering computations can be recycled between optimization iterations, a large number of parameters can be optimized simultaneously in reasonable time. ParticleScattering performs gradient-based optimization of rotation angle for arbitrarily-shaped particles, and radius of circular particles, in conjunction with the Optim optimization package [3], where the objective is to minimize or maximize the electric field intensity at chosen points. Fig. 3.1 shows an example of angle optimization of 20 particles, where the objective is the electric field intensity at the origin. From left to right, we see the electric field before optimization, after minimization, and after maximization. The field intensity at the origin is clearly different in both optimization results, with minimization decreasing the intensity by 95%, and maximization increasing it by over 700%. The total run time for both optimizations and all necessary precomputations was 35 seconds.

For a detailed description of our approach, including several numerical examples generated by ParticleScattering, see our recent publication [4].

Bibliography

[1] J. Bezanson, A. Edelman, S. Karpinski, and V. B. Shah, "Julia: A fresh approach to numerical computing," *SIAM Review*, vol. 59, no. 1, pp. 65–98, 2017.

[2] S. Jahani and Z. Jacob, "All-dielectric metamaterials," *Nature Nanotechnology*, vol. 11, no. 1, pp. 23–36, 2016.

[3] P. K. Mogensen and A. N. Riseth, "Optim: A mathematical optimization package for julia," *Journal of Open Source Software*, vol. 3, p. 615, Apr. 2018.

[4] B. Blankrot and C. Heitzinger, "Efficient computational design and optimization of dielectric metamaterial devices," 2018.

4 Automated Design of Photonic Crystal Demultiplexers

Authored by Boaz Blankrot and Clemens Heitzinger.
Published in *Proc. of the 2018 12th International Congress on Artificial Materials for Novel Wave Phenomena (Metamaterials'2018)*, Espoo, Finland, 27–30 Aug. 2018, pp. 55–57.
doi: 10.1109/MetaMaterials.2018.8534050

Abstract: We describe an approach for the automated design of photonic crystals for various applications. Our approach includes gradient-based optimization for arbitrary objective functions, with the electromagnetic fields calculated by an accurate multiple-scattering approach. An example of a two-color silicon photonic crystal demultiplexer designed by our method is presented, with dozens of parameters chosen automatically in reasonable time. The optimized device exhibits strong focusing with low crosstalk for both frequencies.

4.1 Introduction

Photonic crystals and other metamaterials are integral to recent optical computing efforts, where they may be used to multiplex several signals [1] and replace electronic circuit components [2]. Silicon-based metamaterials are particularly interesting as they exhibit low loss, have a high refractive index, and are compatible with standard fabrication processes [3]. Essentially, the periodic structure of photonic crystals introduces photonic bandgaps that dictate which frequencies can propagate through it in each direction. Therefore, designing photonic crystals for specific applications depends on introducing defects to the structure, such as missing or altered unit cells. The large number of adjustable parameters in practical photonic crystal devices and their multi-scale nature prohibit an exhaustive search of the possible defects. Thus, defects are typically chosen based on a combination of experience, intuition, and simulations.

We designed an optimization-centric approach for modeling these devices [4] based on a multiple-scattering field computation method. In this work we apply this approach to circular rods, and optimize their radii to fit desired device specifications, such as field intensity. Each rod is represented by cylindrical harmonics with incoming and outgoing coefficients describing the incident and scattered fields of that rod, respectively. Next, the electromagnetic interactions between the rods give rise to a multiple-scattering system of equations. Once the system is solved, the fields are given in analytic form which is easily

and accurately computable at any point. Furthermore, the field expression is differentiable which, together with the low computational complexity of our method, allows us to employ gradient-based optimization methods and optimize the radii of some or all of the rods. Notably, our method does not require the rods to be placed in a periodic pattern, such as a grid, in contrast to most large-scale photonic crystal simulators.

4.2 Design Approach

Let us consider a photonic crystal consisting of M circular rods with relative permittivity ε_r in free space, and a TM incident field with respect to the z-axis. Variations involving air holes, dielectric background medium, and/or a TE wave can be handled analogously. Outside the rods, we use a cylindrical harmonics representation of the scattered electric field, and the total field is given by

$$E_z = E_z^{\text{inc}}(\mathbf{r}) + \sum_m \sum_{p=-P}^{P} \beta_p^{(m)} H_p^{(1)} \left(\frac{2\pi}{\lambda} |\mathbf{r} - \mathbf{o}^{(m)}| \right) e^{ip\angle(\mathbf{r}-\mathbf{o}^{(m)})}, \tag{4.1}$$

where for the m-th rod, $\mathbf{o}^{(m)}$ denotes the center coordinates and $\beta_p^{(m)}$ is the (unknown) p-th outgoing coefficient. λ is the free space wavelength, and $H_p^{(1)}$ is the outgoing Hankel function of order p. The relation between incoming and outgoing coefficients for the m-th rod is given analytically as a function of its radius by a diagonal scattering matrix $\mathbf{X}^{(m)}$. If the incident field is also converted to a cylindrical basis with coefficients $\boldsymbol{\alpha}^{(m)}$, we obtain the multiple-scattering equation

$$\boldsymbol{\beta}^{(m)} - \mathbf{X}^{(m)} \sum_{m' \neq m} \mathbf{T}^{(m,m')} \boldsymbol{\beta}^{(m')} = \mathbf{X}^{(m)} \boldsymbol{\alpha}^{(m)}, \quad m = 1, \ldots, M, \tag{4.2}$$

where $\mathbf{T}$ is a dense matrix that translates cylindrical waves from each rod to every other, and depends only on $\mathbf{o}^{(m)}$ but not their radii or material parameters. As the system matrix changes with the radii, it is inefficient to solve this problem directly, and therefore an iterative method is utilized with FMM acceleration. For a detailed description of our approach, see [4].

For our example, we design a device that focuses fields with different wavelengths at different points. Thus we express an optimization objective function capturing this property. Let λ_1, λ_2 be two free-space wavelengths of interest, such that we wish to maximize the intensity of λ_1 and minimize that of λ_2 at a set of points I_1, and vice versa for the points in I_2. A possible objective function for this case is

$$f_{\text{obj}} := \sum_{\mathbf{r} \in I_1} \frac{|E_z(\lambda_2, \mathbf{r})|^2 + 1}{|E_z(\lambda_1, \mathbf{r})|^2} + \sum_{\mathbf{r} \in I_2} \frac{|E_z(\lambda_1, \mathbf{r})|^2 + 1}{|E_z(\lambda_2, \mathbf{r})|^2}, \tag{4.3}$$

where minimization of f_{obj} requires both focusing of the desired field as well as low crosstalk. To compute the j-th component of its gradient $\mathbf{g}_{\text{obj}} := \nabla f_{\text{obj}}$, we first find the partial derivatives of the outgoing coefficients, which in turn requires solving a similar equation

to (4.2) written in concatenated form as

$$(\mathbf{I} - \mathbf{XT})\,\frac{\partial \boldsymbol{\beta}}{\partial R_j} = \frac{\partial \mathbf{X}}{\partial R_j}\mathbf{X}^{-1}\boldsymbol{\beta}, \quad j = 1, \ldots, M. \tag{4.4}$$

Now, the derivative of the electric field (4.1) readily follows and can be plugged in to the derivative of f_{obj}.

4.3 Results

We used the method in Section II to design a two-color demultiplexer, with input free-space wavelengths $\lambda_1 = 560\,\text{nm}$ and $\lambda_2 = 670\,\text{nm}$. Silicon rods were placed on a 7×10 grid with lattice constant $a = 150\,\text{nm}$, where the rods have refractive indices $n = 3.963$ at λ_1 and $n = 3.813$ at λ_2. We assumed the incident field is an $\hat{x}$-traveling, $\hat{z}$-polarized plane wave with unit amplitude. The objective was to focus λ_1 at the bottom right corner of the device, specifically $I_1 = \{(1.5a, -2.9a), (1.5a, -3.1a)\}$, as well as focus the longer wavelength λ_2 at the upper-right corner with $I_2 = \{(1.5a, 2.9a), (1.5a, 3.1a)\}$. The optimization method used to minimize f_{obj} is the Broyden-Fletcher-Goldfarb-Shanno (BFGS) method [5] with the addition of a log-barrier term to prevent rod intersection. The initial radii values for the optimization process are $R_m = a/4$ for all m. Figs. 4.1a and 4.1b depict $|E_z|$ for both wavelengths, where a photonic bandgap prevents the first incident field from penetrating the device, and the second only propagates weakly.

The results of the optimization process are plotted in Figs. 4.1c and 4.1d. For λ_1 we see a region of strong amplification surrounding I_1. Specifically, the field amplitude at I_1 averages at 51.9, while the average amplitude at I_2 is 0.17. We see complementing behavior for λ_2, which was steered towards I_2. There we have average amplitude 39.7, while in I_1 the average field amplitude is only 0.22. In other words, the device amplifies each frequency by a factor of $\approx$40 relative to the incident field amplitude, while maintaining low crosstalk ($-40\,\text{dB}$). As expected, the field intensity is highest inside the high-permittivity rods, but this does not detract from the strong amplification at the chosen points in the air. As shown in Fig. 4.1e, the BFGS algorithm converged within 293 iterations (7.8 hours) under the criterion $\Delta f_{\text{obj}} < 10^{-5}$, where the gradient norm remained large partially due to the log barrier.

4.4 Conclusion

We described our method for automating photonic crystal design to fit given field intensity specifications, particularly by optimizing rod radii. The validity of our approach was demonstrated through a silicon demultiplexer that focuses fields of two frequencies at chosen points. Not only were the fields amplified at the desired locations, but very low crosstalk was observed as well. The irregularity of the resulting structure suggests that this optimal design would not be reached by a non-automatic process. We expect our method to be employable for the automated design of new photonic crystal devices, and for improving existing ones.

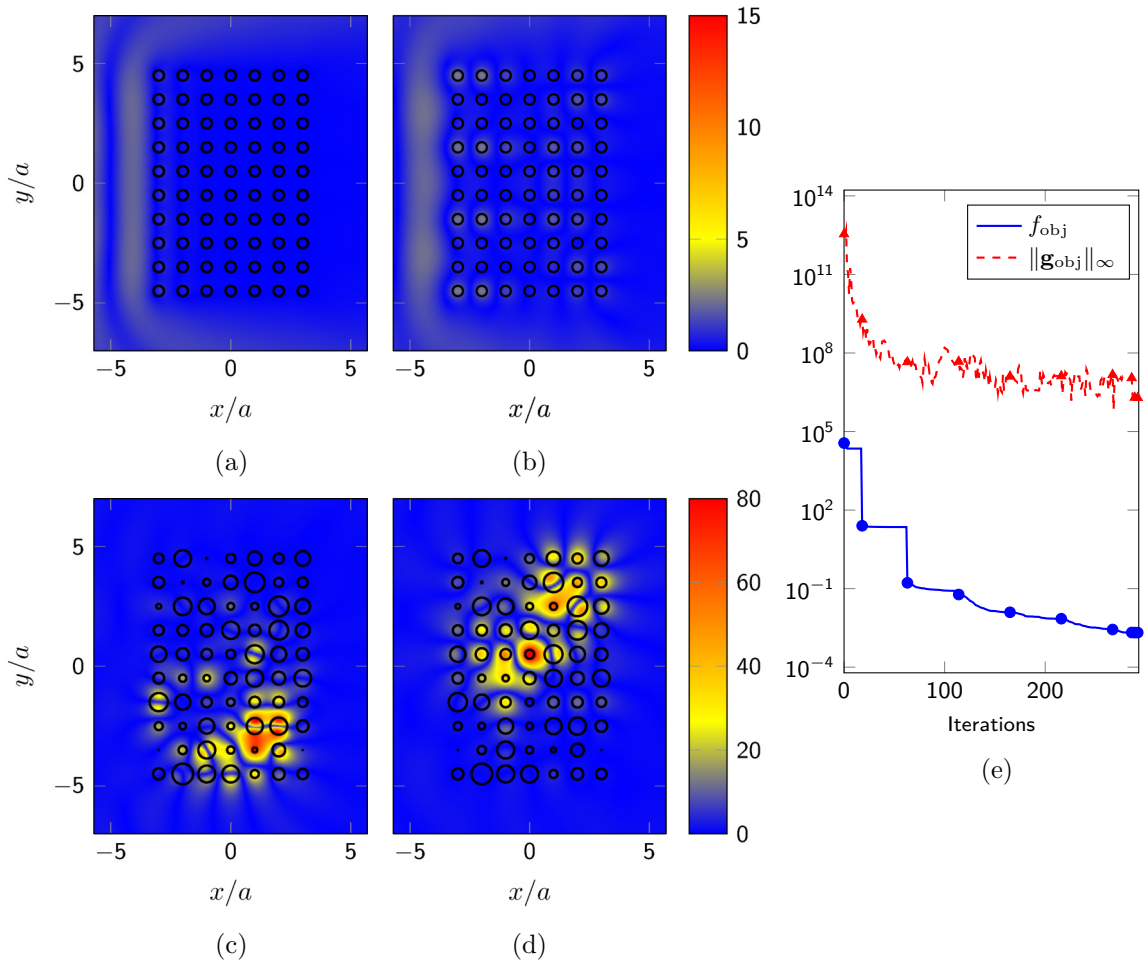

Fig. 4.1: Optimization of photonic crystal device for focusing two wavelengths. $|E_z|$ prior to optimization for (a) $\lambda_1 = 560\,\text{nm}$, and (b) $\lambda_2 = 670\,\text{nm}$. Post-optimization $|E_z|$ for (c) λ_1, and (d) λ_2. (e) Convergence of the objective function f_{obj} and gradient norm $\|\mathbf{g}_{\text{obj}}\|_\infty$. Starting points of outer BFGS iterations are denoted by markers.

Bibliography

[1] M. Y. Tekeste and J. M. Yarrison-Rice, "High efficiency photonic crystal based wavelength demultiplexer," *Optics Express*, vol. 14, no. 17, pp. 7931–7942, 2006.

[2] P. Rani, Y. Kalra, and R. Sinha, "Realization of AND gate in Y shaped photonic crystal waveguide," *Optics Communications*, vol. 298–299, pp. 227–231, 2013.

[3] I. Staude and J. Schilling, "Metamaterial-inspired silicon nanophotonics," *Nature Photonics*, vol. 11, pp. 274–284, 2017.

[4] B. Blankrot and C. Heitzinger, "Efficient computational design and optimization of dielectric metamaterial devices," submitted for publication.

[5] J. Nocedal and S. Wright, *Numerical Optimization*. Springer-Verlag New York, 2 ed., 2006.

5 Design of aperiodic demultiplexers and optical diodes by optimizing photonic crystals

Authored by Boaz Blankrot and Clemens Heitzinger.
Published in *OSA Continuum*, vol. 2, no. 7, pp. 2244–2252, Jul. 2019.
doi: 10.1364/OSAC.2.002244

Abstract: We apply a previously developed approach for the automated design of optical structures to two cases. This approach reduces the basis of the electromagnetic system to obtain fast gradient-based optimization. In the first case, an existing photonic crystal demultiplexer is optimized for higher power transmission and lower crosstalk. In the second, new optical diodes for plane- and cylindrical-wave incidence are designed using a photonic crystal as a starting point. Highly efficient and aperiodic devices are obtained in all cases. These results indicate that aperiodic devices produced by this automated design method can outperform their analytically-obtained counterparts, and encourage its application to other photonic crystal-based devices.

5.1 Introduction

Photonic crystals, metamaterials, and other optical nanostructures have been attracting interest due to their unique and effective light-manipulation abilities. The advent of optical computing has brought the promise of higher bandwidth and lower energy dissipation [1], at the cost of reinventing traditional electrical structures for photonics, such as diodes, logical gates [2, 3], and demultiplexers. Demultiplexers are crucial for splitting optical signals in photonic circuits in general, but particularly for the goal of all-optical computing, and have been designed via e.g. arrayed-waveguide gratings [4], microring resonators [5], shape optimization [6], and photonic crystals [7, 8, 9]. Passive optical diodes, or devices that allow asymmetrical optical transmission, have been of great interest due to their potential as building blocks in optical computing and communication. As such, they have been developed using a variety of methods, including nonlinearity [10], magneto-optical effects [11], metamaterials [12, 13], gratings [14, 15], and photonic crystal-based structures [16, 17, 18]. Photonic crystals for these applications are typically periodic with the exception of defects introduced to the design for specific light localization properties.

However, in [19], the advantage of exploring aperiodic layouts was demonstrated by showing via statistical analysis that their additional degrees of freedom allow better control of the electromagnetic fields. As expected, this phenomenon was more pronounced in the near field, which is the region of interest in photonic crystal design. Previous results in [20] suggest that better focusing of light can be achieved via optimization which yields irregular layouts. The restrictive nature of periodic structures is also apparent when designing multi-frequency photonic crystal devices using bandgap information; often, the range of compatible frequencies is somewhat restricted by the geometry.

In this work, we present aperiodic two-dimensional nanostructures consisting of circular silicon rods in air which were automatically designed for two applications: multiplexing and one-way transmission of transverse magnetic (TM) waves. The work herein builds upon an optimization approach for the design of photonic structures introduced in [20] and later extended to multiple-frequency devices such as demultiplexers in [21]. In this approach, rods are replaced with multipole expansions and the interactions between them are described as a compressed multiple-scattering system [22, 23]. This system is analytically differentiable as a function of the rod radii, facilitating fast gradient-based optimization. We believe these devices are not only useful for the applications outlaid above, but also that the methodology used to design them may be applied to better many other photonic structures.

Prior work on optimizing photonic structures has used e.g. topology optimization [24], with finite differences or finite elements as the underlying electromagnetic solver, which requires computationally expensive and repetitive solutions with many degrees of freedom. Conversely, our method represents each rod with a small multipole expansion, substantially compressing the electromagnetic system of equations. In [25], genetic optimization of a small number of parameters in photonic crystal slab cavities obtained optimal quality factors, though the wave expansion required a large basis which inevitably led to long run times. Recently, a periodic photonic-crystal-based LED structure was optimized for color conversion in [26] where a homogenization technique was applied to the unit cell. In contrast, our approach allows for aperiodic solutions, whether in radii or in location.

5.2 Formulation of our approach

We assume an arbitrary layout of M dielectric circular rods with radii R_m in two-dimensional space. Our goal is to optimize a function $f(P_i(\ell_j))$ where i denotes a specific combination of wavelength, refractive index, and incident field, and ℓ_j is a curve through which power flow is calculated, such that

$$P_i(\ell_j) = \frac{1}{2}\Re \int_{\ell_j} (\boldsymbol{E}_i \times \boldsymbol{H}_i^*) \cdot \hat{\mathbf{n}} \, \mathrm{d}l. \tag{5.1}$$

For each setting $i = 1, \ldots, I$, we use the multiple-scattering formulation to arrive at our system of equations

$$(\mathbf{I} - \mathbf{X}_i \mathbf{T}_i)\boldsymbol{\beta}_i = \mathbf{X}_i \boldsymbol{\alpha}_i, \tag{5.2}$$

where $\mathbf{X}_i$ is a diagonal scattering matrix that additionally depends on the radius of the rods, and $\mathbf{T}_i$ is a translation matrix that depends on the distances between the rods. $\boldsymbol{\alpha}_i$

are the resulting coefficients of expanding the incident field with Bessel functions, $\boldsymbol{\beta}_i$ are the outgoing multipole coefficients, and the residuals of these systems are denoted by $\mathbf{c}_i$. As the multipole expansion yields the representation $E_{i,z}(\mathbf{r}) = \mathbf{e}_{i,z}(\mathbf{r}) \cdot \boldsymbol{\beta}$, and similar representations for $H_{i,x}$, $H_{i,y}$, we can find the derivatives of the power with respect to these coefficients, $\partial P_i / \partial \boldsymbol{\beta}_i$. We can now construct the gradient of f with respect to the radii for our optimization problem using the adjoint method [27]. For complex vectors $\boldsymbol{\zeta}_i$, we define the Lagrangian

$$\Lambda = f + 2\Re \sum_i \boldsymbol{\zeta}_i^\top \mathbf{c}_i, \tag{5.3}$$

whose total derivative with respect to one of the radii R_m can be written as follows using the chain rule,

$$\frac{d\Lambda}{dR_m} = 2\Re \sum_i \left(\boldsymbol{\zeta}_i^\top (\mathbf{I} - \mathbf{X}_i \mathbf{T}_i) + \frac{\partial f}{\partial \boldsymbol{\beta}_i} \right) \frac{\partial \boldsymbol{\beta}_i}{\partial R_m} - \boldsymbol{\zeta}_i^\top \frac{\partial \mathbf{X}_i}{\partial R_m} \mathbf{X}_i^{-1} \boldsymbol{\beta}_i. \tag{5.4}$$

Equating the expression in the parentheses with zero and solving the resulting adjoint systems of equations for $\boldsymbol{\zeta}_i$, which does not depend on m, means that the right-hand side of (5.4) can be computed for all values of m with I system solutions. On the other hand, since we are solving for $\mathbf{c}_i = 0$, we know that the total derivatives of Λ and f are equal. Finally, the derivatives of the scattering matrices are computed analytically as a combination of Bessel and Hankel functions. Thus both f and its gradient can be computed with the runtime complexity of $2I$ system solutions, which in our case are accelerated with the Fast Multipole Method [28].

5.3 Results and discussion

We first consider a two-input demultiplexer, or diplexer, where we take as a reference design the device conceived in [29]. The device consists of a T-junction with a line defect input waveguide where the bulk photonic crystal has rod radius $r/a = 0.18$ and a bandgap for $\omega a / 2\pi c = 0.303 - 0.444$, for unit cell size a. In that work, both the selection of operating frequencies and the design of the output waveguides were tuned manually such that the two dispersion curves exhibited specific characteristics. This reference design was chosen since it was highly efficient to begin with, and therefore any improvements achieved using optimization would lend support to our method. This reference design is depicted in Fig. 5.1, where the unit cell size is $a = 1\,\mu\text{m}$, the refractive index of the rods is $n = 3.4$, and the two normalized input frequencies are $a/\lambda_1 = 0.387$, $a/\lambda_2 = 0.336$. The diplexer is excited by a current filament, and the desired outputs for λ_1, λ_2 are on the left and right sides, respectively.

We simultaneously optimized the radii of the 172 rods in this design to maximize desired power flow while minimizing crosstalk and leakage by minimizing the objective function

$$f = \sum_{i=1,2} \frac{P_{3-i}(\ell_i)}{P_i(\ell_i)} + \frac{P_i(\ell_3)}{P_i(\ell_i)} + \frac{P_i(\ell_{2i+2})}{P_i(\ell_i)} + \frac{P_i(\ell_{2i+3})}{P_i(\ell_i)} + C \max\left(0, 1 - \frac{P_i(\ell_i)}{P_i^*}\right)^2, \tag{5.5}$$

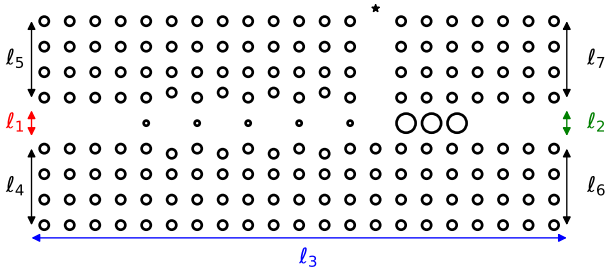

Fig. 5.1: Diplexer before optimization. Unit cell size is $a = 1\,\mu\text{m}$, lines indicate arcs through which the propagated power was calculated for optimization. Black star denotes the input current filament location.

where $P_i(\ell_j)$ is the power flow of the i-th wavelength propagating through the arc ℓ_j; the arcs are shown in Fig. 5.1. For each value of i, the first summand minimizes crosstalk, the last summand penalizes solutions where the output power is smaller than a predetermined quantity, and the other summands represent power leakage through the bottom and sides of the bulk photonic crystal. P_1^*, P_2^* were chosen to be 1.1 times their respective output powers in the reference design, and $C = 1000$ is the penalty factor. Note that in the reference design, some of the rods in the fourth and sixth rows are off the square grid. However, the starting point of our optimization process has these rods on the grid to allow greater flexibility in choice of radii. The entire optimization process took 1.5 hours on a 3.4GHz Intel Core i7-6700 CPU, where each rod was expanded into 21 cylindrical waves and the solver tolerance was 10^{-6}.

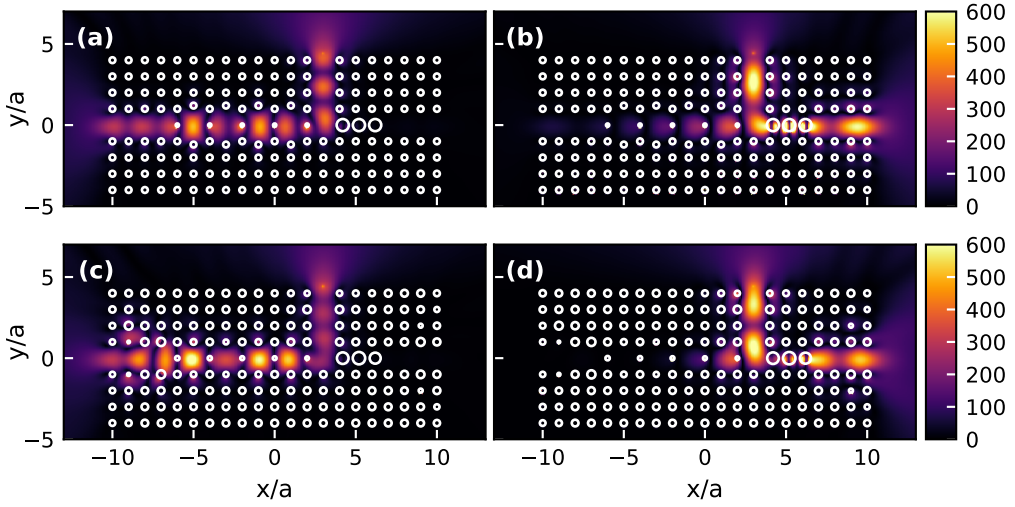

Fig. 5.2: Amplitude of the electric field E_z in the diplexer when excited by a current filament. (a) Reference design with λ_1, (b) reference design with λ_2, (c) optimized design with λ_1, (d) optimized design with λ_2.

Figs. 5.2(a) and 5.2(b) show the electric field amplitude in the reference design when excited by a 1 µA current filament[1] with wavelengths λ_1 and λ_2, while Figs. 5.2(c) and 5.2(d) show the optimized device. The left waveguide in the optimized design exhibits stronger localization for λ_1 and less crosstalk from λ_2. The radii in the optimized device are less regular, with both symmetric and asymmetric deformations surrounding both exit waveguides, for example, on the second column from the left. We also see a gradual tapering of the radii around the input.

In Fig. 5.3 we depict in detail the power density entering through the top of the device and exiting the desired side for each frequency. Visibly more power is launched through the centers of the desired outputs (Figs. 5.3(b,d)), at the expense of slightly larger side lobes. The power entering and exiting the devices is computed as follows: the power density is integrated along the entire top border as well as along each side border. The calculation was performed in this manner to account for all of the power flowing through the device, including through the bulk photonic crystal. For presentation purposes we omitted those parts of Figs. 5.3(a,c) where the power density is essentially zero despite being integrated over. The optimized device has better matching to the source, with total power flow through the top border of $55.48\,\mu\mathrm{W\,m^{-1}}$ vs. $54.39\,\mu\mathrm{W\,m^{-1}}$ in the reference design for λ_1, and $102.07\,\mu\mathrm{W\,m^{-1}}$ vs. $68.55\,\mu\mathrm{W\,m^{-1}}$ for λ_2. This is unsurprising since the reference design was originally simulated with a different source type; however, based on these results we expect the optimization to also match well to other source types.

The ratios between the power exiting the sides and bottom, to the power entering the top of the devices are summarized in Table 5.1, where the power is calculated according to (5.1) using the complete side length. Here we see that for the optimized device, the percentage of the power exiting the desired side is increased for λ_2 and unchanged for λ_1, and that the power at the undesired side is reduced for both frequencies. Accordingly, the crosstalk for λ_1 is $-24.5\,\mathrm{dB}$ before optimization and $-27.4\,\mathrm{dB}$ after, while for λ_2 optimization reduced the crosstalk from $-19.3\,\mathrm{dB}$ to $-44.0\,\mathrm{dB}$. The crosstalk was calculated by dividing the unwanted power transmission ratio by that of the desired wavelength, in order to account for the different total power entering each device for each frequency, as exemplified in Fig. 5.3. We observe that due to our optimization of several objectives simultaneously, power loss through the bottom of the optimized device slightly increased for λ_1.

Table 5.1: **Power Transmission for Diplexer**

	λ_1, left	λ_1, right	λ_1, bottom	λ_2, left	λ_2, right	λ_2, bottom
Reference	99.5%	0.35%	0.12%	1.17%	98.6%	0.24%
Optimized	99.5%	0.18%	0.33%	0.004%	99.8%	0.19%

In Fig. 5.4, we present the power transmission of both reference and optimized designs for a range of different wavelengths. The total power flow in the left and right directions is shown in Fig. 5.4(a), where we observe once again that the power transmitted for λ_2 (left vertical line) is much higher in the optimized design. For $a/\lambda = 0.35 - 0.38$, power flow to both sides drops precipitously in the optimized device, but only on the right-hand side

[1] We refer to Appendix A.2 for a detailed treatment of this electromagnetic source (not part of the original publication).

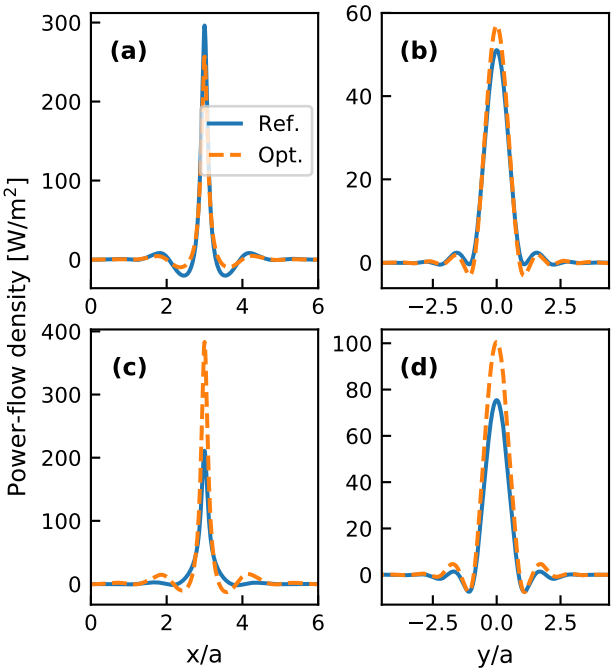

Fig. 5.3: Power density entering the top and exiting the desired sides of the reference and optimized diplexers. (a) λ_1 power entering the top, (b) λ_1 exiting the left, (c) λ_2 entering the top, (d) λ_2 exiting the right.

for the reference. Fig. 5.4(b) shows the same power normalized by the power entering the device for each wavelength. Interestingly, there is a wider range of frequencies surrounding λ_2 where both the power and the normalized transmission to the left are large for the optimized device than for the reference design, despite the optimization being performed at only two wavelengths.

Fig. 5.5 shows the second device we designed, an optical diode structure that permits light propagation in one direction while restricting it in the opposite direction. This device was achieved by optimizing the radii of 67 dielectric rods ordered in a triangular lattice for maximizing left-to-right power propagation from a plane wave while minimizing right-to-left propagation. In this case, the optimization required 20 minutes before convergence. Each rod was expanded into 21 cylindrical waves and a relative tolerance of 10^{-6} for the electromagnetic solver.

The optimization starting point had $r/a = 0.2$ for all rods, where the cell size is $a = 600\,\text{nm}$ and the desired operating wavelength is $\lambda = 1500\,\text{nm}$, both of which correspond to a normalized frequency of $\omega a/2\pi c = 0.4$, and we used a wavelength-dependent refractive index for the silicon ($n = 3.48$ at $\lambda = 1500\,\text{nm}$) [30].

The objective in this case was maximizing the power P_r propagating through the right side for plane waves originating from the left, while minimizing the power P_l on the left side from plane waves propagating in the $x = -\infty$ direction. P_r, P_l were computed by integrating the $\hat{x}$-directed power flow density along the dotted lines in Fig. 5.5. This objective is expressed

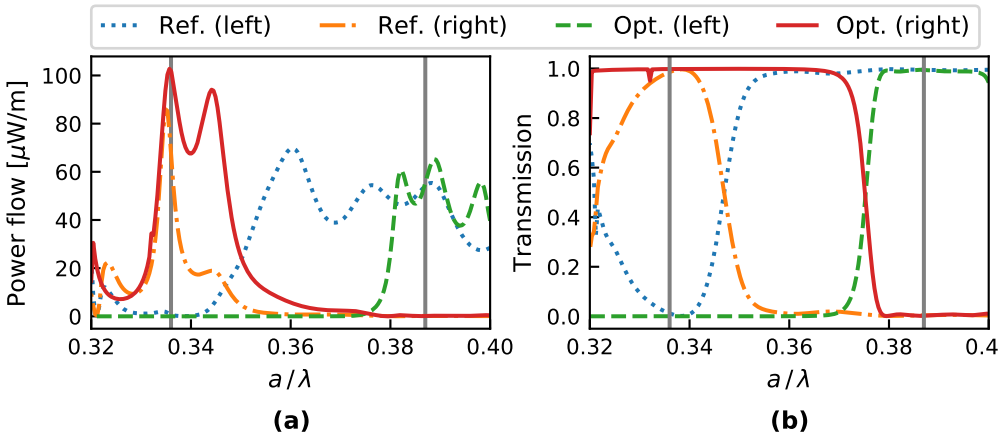

Fig. 5.4: Power flow to the left and right sides of the reference and optimized diplexers. (a) Absolute. (b) Normalized by power entering the device. Vertical lines indicate the frequencies of interest λ_1, λ_2.

by minimizing the function

$$f = \frac{1}{P_r}\left(1 + C\frac{|P_l|}{P_r}\right), \tag{5.6}$$

where $C = 1000$ was chosen as the transmission ratio penalty factor.

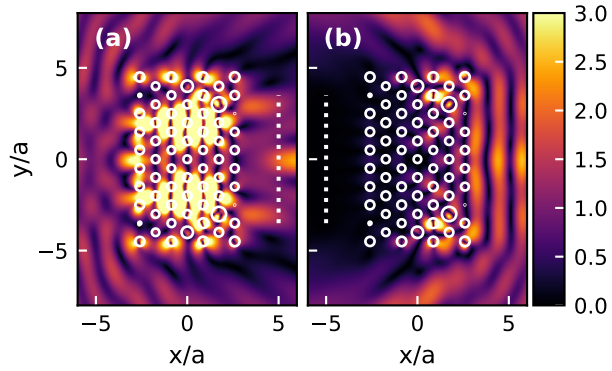

Fig. 5.5: Amplitude of E_z for the designed optical diode in response to a unit plane wave. (a) Left-to-right propagation. (b) Right-to-left propagation. Dotted line indicates where power flow was optimized and calculated.

Setting the optimization starting point of $r/a = 0.2$ for all rods places λ in a complete photonic bandgap, as depicted in Fig. 5.6, which shows the band structure for the infinitely periodic version of the device. This initial structure does not allow propagation of $\pm\hat{x}$-directed plane waves, despite having only 7 cells in the x direction. The choice of the initial device was such that the bandgap would prevent propagation in both directions, and the optimization process would tweak the device to permit one-directional propagation. Indeed, we can see in Fig. 5.5(a) that the electric field originating from the left propagates through

the device, and is magnified in certain regions on the right. On the other hand, when the field originates from the right as in Fig. 5.5(b), the device creates a shaded area on the left with near-zero electric field amplitude. Due to the optimization, all of the radii changed by at least 2.5%, with the most radical changes at the corners of the structure, where a few rods have been nearly eliminated from the structure and others have doubled in size.

We also investigated the performance of this device for a range of wavelengths surrounding λ, namely 1400 to 1600 nm. In Fig. 5.7(a), we have the power flow measured in both directions, normalized by the power flow in the absence of the device, P_0. At 1500 nm, we have $P_r = 1.37P_0$ and $P_l = 2.06 \times 10^{-6} P_0$, as well as a FWHM of 9.65 nm for P_r. We may have P_r/P_0 greater than unity, partially because the height of the device exceeds the length of the line on which the power is measured. The ratio between right- and left-propagating power is depicted with a solid line in Fig. 5.7(b), where a transmission ratio of 58.2 dB is achieved. The stark narrowbandedness exhibited in both plots is expected since the optimization was performed for a single frequency.

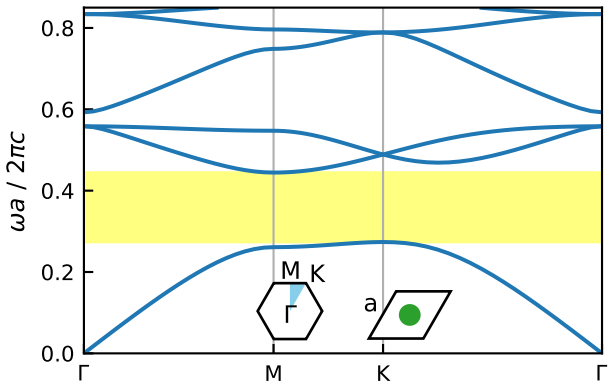

Fig. 5.6: Photonic band structure for a triangular array of dielectric ($n = 3.48$) rods of radius $r/a = 0.2$ in air, for TM polarization. The insets depict the irreducible Brillouin zone in light blue as well as the unit cell.

Lastly, we optimized the same initial triangular lattice for one-way transmission in the presence of current filament excitation, placed at $(\pm 5a, 0)$. The minimization process in this case required 19 minutes. This device had a transmission ratio of 46 dB at $\lambda = 1500$ nm, as plotted with a dashed line in Fig. 5.7(b). The resulting structure, shown in Fig. 5.8, is irregular as well, with a large variance of the radii present in the structure. In this case, the power density distribution after optimization is concentrated in two lobes, as opposed to the strong central lobe in the plane-wave case. Similarly to the optimized diplexer, there is tapering of the radii in the vicinity of the source on the left. The high transmission ratios for both types of excitation suggest that our method may find optimal devices for different incident fields.

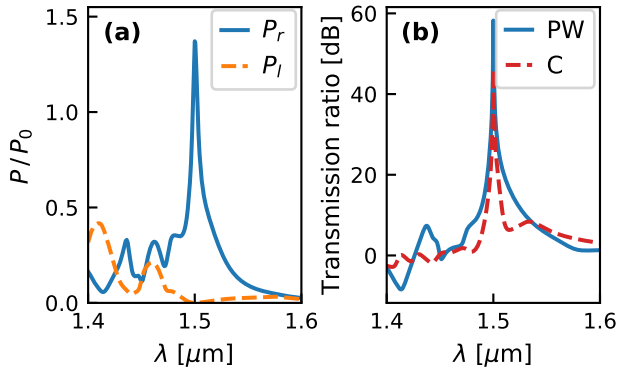

Fig. 5.7: (a) Power transmission spectrum in both directions, normalized by the power flow without the device. (b) Transmission ratio between right- and left-propagating light for the device that was optimized for excitation by plane wave (solid line) and current filament (dashed).

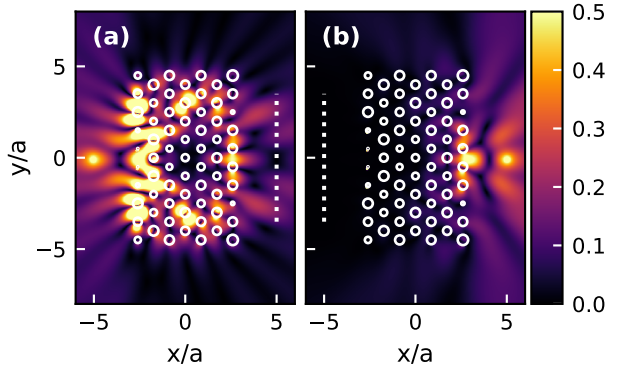

Fig. 5.8: Amplitude of E_z for the designed optical diode in response to a 1 nA current filament. (a) Left-to-right propagation. (b) Right-to-left propagation. Dotted line indicates where power flow was optimized and calculated.

5.4 Conclusion

In summary, we designed two aperiodic devices, each consisting of a collection of dielectric rods, using optimization. The first device, a diplexer, was the result of optimizing an existing design and yielded better performance in our simulations. Next, we designed an optical diode to realize passive one-way transmission. Here we began with a uniform structure based on the photonic bandgap and obtained a device with a high transmission ratio. In both cases, the resulting optimized devices had rather irregular and unintuitive radius distributions, which agrees with the suggestion that irregular structures introduce additional degrees of freedom which may be exploited for precise electromagnetic field control. These devices can find potential use in optical computing, and the method we employed in this work shows promise for designing other dielectric photonic devices.

Bibliography

[1] H. J. Caulfield and S. Dolev, "Why future supercomputing requires optics," *Nature Photonics*, vol. 4, no. 5, p. 261, 2010.

[2] Y. Liu, F. Qin, Z.-M. Meng, F. Zhou, Q.-H. Mao, and Z.-Y. Li, "All-optical logic gates based on two-dimensional low-refractive-index nonlinear photonic crystal slabs," *Optics Express*, vol. 19, pp. 1945–1953, Jan 2011.

[3] V. Jandieri, R. Khomeriki, and D. Erni, "Realization of true all-optical AND logic gate based on nonlinear coupled air-hole type photonic crystal waveguides," *Optics Express*, vol. 26, pp. 19845–19853, Aug 2018.

[4] H. Takahashi, S. Suzuki, K. Kato, and I. Nishi, "Arrayed-waveguide grating for wavelength division multi/demultiplexer with nanometre resolution," *Electronics Letters*, vol. 26, no. 2, pp. 87–88, 1990.

[5] Y. Tan, H. Wu, S. Wang, C. Li, and D. Dai, "Silicon-based hybrid demultiplexer for wavelength- and mode-division multiplexing," *Optics Letters*, vol. 43, pp. 1962–1965, May 2018.

[6] A. Y. Piggott, J. Lu, K. G. Lagoudakis, J. Petykiewicz, T. M. Babinec, and J. Vučković, "Inverse design and demonstration of a compact and broadband on-chip wavelength demultiplexer," *Nature Photonics*, vol. 9, no. 6, pp. 374–377, 2015.

[7] E. Centeno, B. Guizal, and D. Felbacq, "Multiplexing and demultiplexing with photonic crystals," *Journal of Optics A: Pure and Applied Optics*, vol. 1, no. 5, p. L10, 1999.

[8] A. Sharkawy, S. Shi, and D. W. Prather, "Multichannel wavelength division multiplexing with photonic crystals," *Applied Optics*, vol. 40, pp. 2247–2252, May 2001.

[9] V. Liu, Y. Jiao, D. A. B. Miller, and S. Fan, "Design methodology for compact photonic-crystal-based wavelength division multiplexers," *Optics Letters*, vol. 36, pp. 591–593, Feb 2011.

[10] R. Philip, M. Anija, C. S. Yelleswarapu, and D. V. G. L. N. Rao, "Passive all-optical diode using asymmetric nonlinear absorption," *Applied Physics Letters*, vol. 91, no. 14, p. 141118, 2007.

[11] M. Vanwolleghem, X. Checoury, W. Śmigaj, B. Gralak, L. Magdenko, K. Postava, B. Dagens, P. Beauvillain, and J.-M. Lourtioz, "Unidirectional band gaps in uniformly magnetized two-dimensional magnetophotonic crystals," *Physical Review B*, vol. 80, p. 121102, Sep 2009.

[12] C. Menzel, C. Helgert, C. Rockstuhl, E.-B. Kley, A. Tünnermann, T. Pertsch, and F. Lederer, "Asymmetric transmission of linearly polarized light at optical metamaterials," *Physical Review Letters*, vol. 104, p. 253902, Jun 2010.

[13] Y. Xu, C. Gu, B. Hou, Y. Lai, J. Li, and H. Chen, "Broadband asymmetric waveguiding of light without polarization limitations," *Nature Communications*, vol. 4, no. 2561, 2013.

[14] M. Stolarek, D. Yavorskiy, R. Kotyński, C. J. Z. Rodríguez, J. Łusakowski, and T. Szoplik, "Asymmetric transmission of terahertz radiation through a double grating," *Optics Letters*, vol. 38, pp. 839–841, Mar 2013.

[15] P. Xu, X. Lv, J. Chen, Y. Li, J. Qian, Z. Chen, J. Qi, Q. Sun, and J. Xu, "Dichroic optical diode transmission in two dislocated parallel metallic gratings," *Nanoscale Research Letters*, vol. 13, p. 392, Dec 2018.

[16] Y. Zhang, Q. Kan, and G. P. Wang, "One-way optical transmission in silicon grating-photonic crystal structures," *Optics Letters*, vol. 39, pp. 4934–4937, Aug 2014.

[17] D. Liu, S. Hu, and Y. Gao, "One-way optical transmission in silicon photonic crystal heterojunction with circular and square scatterers," *Physics Letters A*, vol. 381, no. 25, pp. 2131–2135, 2017.

[18] E. Bor, M. Turduev, U. G. Yasa, H. Kurt, and K. Staliunas, "Asymmetric light transmission effect based on an evolutionary optimized semi-dirac cone dispersion photonic structure," *Physical Review B*, vol. 98, p. 245112, Dec 2018.

[19] Y.-C. Hsueh and K. J. Webb, "Electromagnetic field control with binary aperiodic nanostructures," *Journal of the Optical Society of America B*, vol. 34, pp. 2059–2071, Oct 2017.

[20] B. Blankrot and C. Heitzinger, "Efficient computational design and optimization of dielectric metamaterial devices." `http://arxiv.org/abs/1804.09489`, 2018. *Submitted for publication.*

[21] B. Blankrot and C. Heitzinger, "Automated design of photonic crystal demultiplexers," in *2018 12th International Congress on Artificial Materials for Novel Wave Phenomena (Metamaterials)*, (Espoo, Finland), pp. 55–57, August 2018.

[22] N. A. Gumerov and R. Duraiswami, "A scalar potential formulation and translation theory for the time-harmonic Maxwell equations," *Journal of Computational Physics*, vol. 225, no. 1, pp. 206–236, 2007.

[23] J. Lai, M. Kobayashi, and L. Greengard, "A fast solver for multi-particle scattering in a layered medium," *Optics Express*, vol. 22, pp. 20481–20499, Aug 2014.

[24] J. S. Jensen and O. Sigmund, "Systematic design of photonic crystal structures using topology optimization: Low-loss waveguide bends," *Applied Physics Letters*, vol. 84, no. 12, pp. 2022–2024, 2004.

[25] M. Minkov and V. Savona, "Automated optimization of photonic crystal slab cavities," *Scientific Reports*, vol. 4, p. 5124, 2014.

[26] C. Valagiannopoulos and P. G. Lagoudakis, "Photonic crystals for optimal color conversion in light-emitting diodes: a semi-analytical approach," *Journal of the Optical Society of America B*, vol. 35, pp. 1105–1112, May 2018.

[27] P. Seliger, M. Mahvash, C. Wang, and A. F. J. Levi, "Optimization of aperiodic dielectric structures," *Journal of Applied Physics*, vol. 100, no. 3, p. 034310, 2006.

[28] R. Coifman, V. Rokhlin, and S. Wandzura, "The fast multipole method for the wave equation: a pedestrian prescription," *IEEE Antennas and Propagation Magazine*, vol. 35, pp. 7–12, June 1993.

[29] J. Smajic, C. Hafner, and D. Erni, "On the design of photonic crystal multiplexers," *Optics Express*, vol. 11, pp. 566–571, Mar 2003.

[30] H. H. Li, "Refractive index of silicon and germanium and its wavelength and temperature derivatives," *Journal of Physical and Chemical Reference Data*, vol. 9, no. 3, pp. 561–658, 1980.

6 On the robust optimization of photonic structures for asymmetric light transmission

Authored by Boaz Blankrot and Clemens Heitzinger.
Submitted for publication, Jul. 2020.

Abstract: Optimization of nanophotonic structures has become increasingly common in recent years, yet these optimized devices can be very sensitive to manufacturing variations, to the point where small perturbations render them ineffective. Robust optimization aims to solve this issue by taking the worst-case perturbation of a design into account. We implement and utilize two methods for robust optimization of two-dimensional photonic crystals to achieve asymmetric light transmission. By optimizing the radii in a photonic crystal consisting of 53 dielectric rods, we achieve a structure with this effect, with a transmission ratio of 14.6 dB in the worst case. Nevertheless, the price of robustness is that this structure can achieve a transmission ratio of 55 dB and higher transmission in the forward direction with traditional optimization. This work can be generalized to other photonic crystal-based structures as well as other error sources such as frequency or refractive index variations.

6.1 Introduction

Optical devices that exhibit asymmetric light transmission (ALT) are attracting considerable interest due to their potential role in future optical computing and communication systems [1]. These devices feature large transmission ratios between forward- and backward-propagating light, not unlike electrical diodes. In the past, asymmetric light transmitters were developed using nonlinearity [2], magneto-optical effects [3], gratings [4, 5], metamaterials [6, 7], and photonic crystal structures [8, 9]. These photonic crystal-based structures with an ALT effect are typically periodic, with the exception of defects that are manually introduced to the structure in order to effect specific light manipulation properties. Recently, the use of optimization for designing these devices has been explored [10, 11], yielding devices with large transmission ratios. One of the reasons why optimization and inverse design are attractive is that they allow aperiodic layouts with many degrees of freedom, thus allowing better control of the electromagnetic fields [12]. However, a major downside is that devices optimized by these procedures are often highly sensitive to the underlying geometric

parameters. Concurrently, due to inevitable manufacturing variations these devices cannot be implemented precisely, but only with random perturbations which can cancel out the optimized performance [13]. The focus thus shifts from nominal optimization to *robust* optimization, which takes this uncertainty into account and finds a design with a minimal worst-case perturbation.

Despite the large body of work on robust optimization [14], its application to photonics has been far more limited, perhaps due to the scale and nonconvexity of the problems common in the field. In [15], five geometrical parameters of plasmonic waveguides were optimized where robustness was measured by the gradient index. A Kriging-based method for robust optimization was proposed in [16] and applied to the width, lengths, and gaps of ring resonator-based optical filters. Robust topology optimization was applied to various photonic structures in [17, 18], where robustness was formulated in response to under- and over-etching, and in [19] this was extended to random edge perturbations. Robust topology optimization was also applied in [20, 21] to photonic bandgap maximization. In [13], adiabatic tapers were robustly optimized where the worst case was approximated by a step in the direction of the gradient. Bertsimas et. al introduced methods for robust optimization of dielectric rod locations involving many parameters using a nested approach, where an inner loop was a gradient-based search for the local worst case and the outer loop was either based on Simulated Annealing (Robust Simulated Annealing [22]) or another local search [23].

In this paper, we investigate two methods for robust optimization of the radii in photonic crystals to achieve ALT that is resistant to implementation error. We motivate this with an example showing that even a minute implementation error in a structure can cause a total loss of desired behavior. The first method we explore is based on the aforementioned Robust Simulated Annealing (RSA), where we utilize the Generalized Simulated Annealing [24] algorithm for the outer loop. For the second method, we employ a recent approach based on a metaheuristic for avoiding non-robust areas, Largest Empty Hypersphere (LEH [25]), which also utilizes a local search in the inner loop, but reduces the number of function evaluations. With both methods, we achieve asymmetric light transmitters that maintain performance in the worst case. To our knowledge, robust optimization of radii in photonic structures has not been previously performed, and a secondary goal of this paper is to demonstrate the issues one will experience when applying robust optimization to similar structures, and possible resolutions. Despite the necessarily large number of function evaluations, our approach is feasible due to the fast underlying electromagnetic solver [26] based on multiple scattering [27].

The remainder of the paper is organized as follows. Section 6.2 gives the mathematical formulation used for calculating the fields scattered by a collection of inclusions, as well as further background on asymmetric light transmission. In Section 6.3, we discuss robust optimization in general and as it pertains to our ALT problem, and describe the two robust optimization strategies utilized in this paper. Section 6.4 presents our numerical results, for both a simple two-dimensional problem and the ALT problem, and a discussion in which we compare and contrast the two strategies. Finally, the results of this work are summarized in Section 6.5.

6.2 Electromagnetic preliminaries

6.2.1 Formulation and electromagnetic field solver

The structures considered herein consist of M homogeneous dielectric circular inclusions embedded in air. This is in order to continue the line of work in [11], however, we note that one could apply the following treatment to the opposite case of air holes in a dielectric slab. When this structure is periodic, it is typically referred to as a two-dimensional photonic crystal. However, the radii of our inclusions are not periodic and although the inclusion locations are periodic in our examples, this is merely for simplicity and will not constrain the formulation below.

In two dimensions, the electromagnetic fields can be decoupled into two field patterns, transverse electric (TE) and transverse magnetic (TM) modes, with respect to the z axis. For TE modes, the electric field does not have a z component and the magnetic field can be written as $\boldsymbol{H} = H_z\hat{z}$; conversely, for TM modes the magnetic field does not have a z component and the electric field is given by $\boldsymbol{E} = E_z\hat{z}$. Thus, while assuming time-harmonic electromagnetic fields, Maxwell's equations in each medium can be reduced to the two scalar Helmholtz equations

$$\big(\nabla^2 + k(\mathbf{r})^2\big)H_z(\mathbf{r}) = 0 \quad \text{for TE modes,} \tag{6.1a}$$

$$\big(\nabla^2 + k(\mathbf{r})^2\big)E_z(\mathbf{r}) = 0 \quad \text{for TM modes,} \tag{6.1b}$$

where $k \coloneqq \omega\sqrt{\mu\varepsilon}$ is the wavenumber for angular frequency ω and medium permittivity and permeability ε, μ. Specifically, we denote the wavenumber outside and inside the inclusions by k_0 and k_1, respectively. In the sequel we consider only TM modes, but this work can be readily extended to TE fields with small modifications.

To solve for the electromagnetic fields, we utilize a multiple-scattering technique [28] and describe the electric field incident to each inclusion with Bessel functions, and similarly with its scattered field using Hankel functions. Given a single inclusion with radius R_m centered at $\mathbf{o}^{(m)}$, we first expand the incident and scattered electric fields E_z^{inc}, E_z^{s} as

$$E_z^{\text{inc}} = \sum_{p=-P}^{P} \alpha_p^{(m)} J_p(k_0|\mathbf{r} - \mathbf{o}^{(m)}|)\exp(ip\angle(\mathbf{r} - \mathbf{o}^{(m)})), \tag{6.2a}$$

$$E_z^{\text{s}} = \sum_{p=-P}^{P} \beta_p^{(m)} H_p^{(1)}(k_0|\mathbf{r} - \mathbf{o}^{(m)}|)\exp(ip\angle(\mathbf{r} - \mathbf{o}^{(m)})), \tag{6.2b}$$

where P is a truncation parameter for which some desired error tolerance is achieved. Applying tangential boundary conditions to the inclusion surface yields a diagonal relationship between these expansions, expressed as $\boldsymbol{\beta}^{(m)} = \mathbf{X}^{(m)}\boldsymbol{\alpha}^{(m)}$, where the scattering matrix is given by

$$X_{p,p'}^{(m)} = -\delta_{p,p'}\frac{J_p(k_0R_m)J_p'(k_1R_m) - J_p'(k_0R_m)J_p(k_1R_m)}{H_p^{(1)}(k_0R_m)J_p'(k_1R_m) - H_p^{(1)\prime}(k_0R_m)J_p(k_1R_m)}. \tag{6.3}$$

We now consider M inclusions, and utilize Graf's addition theorem outside the inclusions to translate the outgoing Hankel expansion of one inclusion to the incoming Bessel expansion of another. This gives the total incoming coefficients of the m'-th inclusion

$$\tilde{\boldsymbol{\alpha}}^{(m')} = \boldsymbol{\alpha}^{(m')} + \sum_{m \neq m'} \mathbf{T}^{(m',m)} \boldsymbol{\beta}^{(m)}, \tag{6.4}$$

with the translation matrix from m to m' defined by

$$T_{\mu,p}^{(m',m)} = \exp\left(i(p-\mu)\angle(\mathbf{o}^{(m')} - \mathbf{o}^{(m)})\right) H_{p-\mu}^{(1)}(k_0 |\mathbf{o}^{(m')} - \mathbf{o}^{(m)}|). \tag{6.5}$$

Substituting the scattering matrix and concatenating over all inclusions finally yields our multiple-scattering system of equations

$$[\mathbf{I} - \mathbf{X}(\mathbf{R})\mathbf{T}]\boldsymbol{\beta} = \mathbf{X}(\mathbf{R})\boldsymbol{\alpha}, \tag{6.6}$$

where we emphasize that only the diagonal scattering matrix depends on $\mathbf{R}$, whereas $\mathbf{T}$ is solely location-dependent. Once this system is solved, the scattered electric field at any point outside the inclusions can be computed by summing (6.2b) over all inclusions. Many design problems, such as the ones considered here, contain more than one electromagnetic setting – i.e., a combination of incident field frequency, and permittivity – so we will use the subscript i to denote the components of (6.6) that depend on the setting. Additionally, we will denote the residuals of those systems by $\mathbf{c}_i$. In our case, we have forward and backward incident fields with the same wavelength and thus only the expansion coefficients will change between settings.

Our objective is a function of electromagnetic power flow through curves ℓ, which we calculate by quadrature over the Poynting vector

$$P_i(\ell) = \frac{1}{2} \operatorname{Re} \int_\ell (\boldsymbol{E}(\boldsymbol{\beta}_i) \times \boldsymbol{H}(\boldsymbol{\beta}_i)) \cdot \hat{n} \, \mathrm{d}l, \tag{6.7}$$

where $\boldsymbol{E}$, $\boldsymbol{H}$ can be calculated by matrix-vector products with pre-computed matrices in $O(M)$ time.

6.2.2 Asymmetric light transmission

Asymmetric light transmission has been a heavily researched topic in the photonics community, partially due to its applications in optical communication and optical computing. This effect has been achieved in many differing ways that can be broadly classified into two classes, non-reciprocal and reciprocal devices. A special case of ALT which strictly blocks all light in one direction while allowing propagation in the other requires one to break Lorentz reciprocity [29]. Such non-reciprocal devices, also named optical isolators, are enabled by materials that break reciprocity such as nonlinear media [2] where the permittivity is a function of the electric field. Magneto-optical materials [3], where the permittivity is an asymmetric tensor, and those with time-dependent ε and μ, are other examples of media that could allow optical isolators. However, such devices can be impractical, due to both fabrication and operation concerns [10].

These shortcomings generated interest in passive and reciprocal devices with an ALT effect that do not break Lorentz reciprocity. For example, in [10], the authors achieved ALT by setting a photonic crystal with a semi-Dirac cone at the operating frequency adjacent to an optimized photonic structure. For the most part, the photonic crystal with the semi-Dirac cone only allows light propagation in the $\pm x$ directions, such that light passing through it first is unaffected and then somewhat disturbed by the optimized section. In the other direction, light passes through the optimized section first then enters the semi-Dirac cone section at oblique angles and is thus reflected. A similar idea was demonstrated in [8], where a photonic crystal with a partial gap – i.e., one that allowed only oblique incident waves through for a range of frequencies – was combined with a silicon grating for the forward-traveling light that changed its direction. In recent work [11], the authors of this paper utilized radius optimization on a photonic crystal to achieve significant ALT in a structure less than 2.5λ wide, and showed that the optimal ALT structure depended heavily on the incident field type. Indeed, the behaviors of these reciprocal structures share a dependence on the spatial properties of the incoming field, and one could in principle construct a field with high backwards propagation. The ALT effect is thus given by a mode conversion – into those that can and cannot propagate deeper in the structure, for the forward and backward directions, respectively.

6.3 Robust optimization

Robust optimization differs from nominal (or traditional) optimization in that it assumes that the objective is impacted by uncertainties or errors in the decision variables, problem parameters, or both. A relevant example of the former could be the inclusion radii, while the latter class includes the incident field frequency, angle, and material parameters. These uncertainties may not only dramatically affect the value of the objective function, but may also make a certain optimum unfeasible. Thus robust optimization is of utmost significance to any real-world application where precision cannot be guaranteed, and especially to those devices whose behavior is sensitive to small changes in their variables and environmental parameters. However, robust optimization carries with it two notable penalties: first, the optimization problem is more complex and must be solved by specialized methods; second, by definition, the robust optimum cannot exceed the nominal one, and often has worse nominal performance, i.e. absent any error. While certain combinations of objectives and uncertainty sets allow the reformulation of robust optimization problems as tractable problems [30], this is not possible for most robust optimization problems. Specifically, nonlinear robust optimization problems such as those arising in computational physics are far less studied than their linear counterparts. See the review [14] for a survey of robust optimization and [31] for a discussion on nonlinear robust optimization.

There are different robustness metrics, some deterministic and some stochastic, that aim to capture the sensitivity of the objective function to these uncertainties. In this work, we consider worst-case implementation uncertainty, i.e. uncertainty in the design variables where the robust objective at a point is the highest value attained by the function in the neighborhood of that point. For a given function f, we define a robust function

$f_\mathrm{w}(\mathbf{R}) = \max_{\Delta\mathbf{R}} f(\mathbf{R}+\Delta\mathbf{R})$ and aim to solve a robust optimization problem of the form

$$\min_{\mathbf{R}} f_\mathrm{w}(\mathbf{R}) \;\text{ subject to }\; \begin{cases} R_\mathrm{min} \le \mathbf{R}+\Delta\mathbf{R} \le R_\mathrm{max}, \\ \|\Delta\mathbf{R}\|_\infty \le \Delta_\mathrm{max}, \end{cases} \tag{6.8}$$

where the inner maximization over $\Delta\mathbf{R}$ is essentially the aforementioned worst-case analysis of the Δ_max-neighborhood of a given set of radii $\mathbf{R}$. We emphasize that the bound constraints on $\mathbf{R}+\Delta\mathbf{R}$ guarantee the feasibility of any perturbed structure. Since the perturbation $\Delta\mathbf{R}$ is a vector, we can account not only for the systematic dilation or erosion of all inclusions by a given scalar amount, but also for random independent perturbations in each radius up to a prescribed limit Δ_max.

Both methods used here share a common step, namely, an inner maximizer that strives to find these worst-case perturbations for a given $\mathbf{R}$ in each outer iteration. Since inner maximization is a global optimization problem, and thus would present significant computational difficulties, these inner global optimizations are replaced by a sequence of local gradient-based searches. The lengths of these sequences vary by method, but in any case the number of local searches necessary to find the global optima with high probability undoubtedly depends on the local complexity of the function relative to Δ_max.

In order to perform this neighborhood exploration efficiently, we calculate the gradient of f using an adjoint approach [32]. This allows us to reduce the asymptotic complexity of the gradient calculation to that of computing f. For each setting i of scattering problems in f, we utilize an arbitrary complex vector $\boldsymbol{\zeta}_i$ and define the Lagrangian

$$\Lambda = f + 2\,\mathrm{Re}\sum_i \boldsymbol{\zeta}_i^\top \mathbf{c}_i, \tag{6.9}$$

whose total derivative with respect to one of the radii R_m is obtained by using the chain rule,

$$\frac{\mathrm{d}\Lambda}{\mathrm{d}R_m} = 2\,\mathrm{Re}\sum_i \left(\boldsymbol{\zeta}_i^\top(\mathbf{I}-\mathbf{X}\mathbf{T}) + \frac{\partial f}{\partial \boldsymbol{\beta}_i}\right)\frac{\partial \boldsymbol{\beta}_i}{\partial R_m} - \boldsymbol{\zeta}_i^\top \frac{\partial \mathbf{X}}{\partial R_m}\mathbf{X}^{-1}\boldsymbol{\beta}_i. \tag{6.10}$$

By solving the system of equations in the parenthesis for $\boldsymbol{\zeta}_i$, we eliminate the costly and m-dependent calculation of $\partial\boldsymbol{\beta}_i/\partial R_m$. Since we are already solving (6.6) for $\mathbf{c}_i = 0$, we know that the total derivatives of Λ and f are equal. Therefore, we have both f and its gradient with respect to $\mathbf{R}$ with the time complexity of 4 system solutions.

6.3.1 Robust Simulated Annealing

The first robust optimization approach we investigate is the RSA approach [22], modified to use a Generalized Simulated Annealing [24] outer loop. Recall that with Simulated Annealing, we randomly select a point from a given distribution, and probabilistically decide whether to move to it. While this initially allows the acceptance of points with higher objective values in order to avoid local minima, as the algorithm progresses and the artificial temperature is reduced, this becomes increasingly less likely. In the RSA

approach, instead of minimizing f_{w}, we minimize a function g_{w} of the high cost points in the $\Delta_{\max}$-neighborhood, given by

$$g_{\mathrm{w}}(\mathbf{R}, T) = T \log \sum_{\hat{\mathbf{R}} \in \mathcal{M}(\mathbf{R})} e^{f(\hat{\mathbf{R}}/T)}, \tag{6.11}$$

where T is the current temperature of the annealing process and $\mathcal{M}(\mathbf{R})$ is the set of high cost points in the neighborhood of $\mathbf{R}$. Notably, g_{w} approaches f_{w} as T diminishes. The cooling schedule of T is expressed as

$$T(t) = T(0) \frac{2^{q_v - 1} - 1}{(2 + t)^{q_v - 1} - 1}, \tag{6.12}$$

where the visiting parameter q_v is a tunable parameter that also governs the trial point distribution. At point $\mathbf{R}$, the probability of accepting a candidate point $\mathbf{R}'$ is calculated using

$$P(\mathbf{R} \to \mathbf{R}') = \begin{cases} 0, & \tilde{P} \leq 0, \\ \tilde{P}^{1/(1-q_a)}, & \text{else}, \end{cases} \tag{6.13}$$

where q_a is the tunable acceptance parameter and $\tilde{P}$ is shorthand for

$$\tilde{P} = 1 + \frac{1 + t}{T(t)} (q_a - 1)[g_{\mathrm{w}}(\mathbf{R}', T(t)) - g_{\mathrm{w}}(\mathbf{R}, T(t))]. \tag{6.14}$$

Therefore, each iteration contains two main steps: generating a random trial point and an inner maximizer for estimating the high-cost points in its neighborhood via a set of $M + 1$ gradient ascents, which are started at predetermined points. One gradient ascent begins at $\mathbf{R}$, while the others begin at $\mathbf{R} \pm \mathbf{e}_m \Delta_{\max}/3$, depending on the sign of the derivative $\partial f / \partial R_m$. Notably, the number of function evaluations in each iteration scales quadratically with M, severely limiting the number of possible iterations for computationally expensive objective functions. As with other Simulated Annealing algorithms, this approach has the benefit of high tunability: annealing, re-annealing, and reheating schedules can all be tweaked, as can the trial point distributions. However, tuned parameters do not always transfer from one optimization problem to another, requiring costly re-tuning. The RSA approach using Generalized Simulated Annealing for the annealing process is summarized in Algorithm 6.2.

6.3.2 Largest Empty Hypercube

The second robust optimization approach we utilize is LEH [25], which operates as follows: it keeps track of the minimal value of f_{w} encountered thus far, denoted τ, and a set of high-cost points H_τ. Here, high-cost points are defined as those points encountered so far where $f \geq \tau$. In each iteration, we look for the largest hypercube in the problem domain that does not contain points from H_τ. Once a hypercube is found, we explore the $\Delta_{\max}$-neighborhood surrounding its center $\mathbf{R}_{\mathrm{c}}$ in order to ascertain if $f_{\mathrm{w}}(\mathbf{R}_{\mathrm{c}})$ is less than τ. This local worst-case search is performed using multiple L-BFGS-B [33] searches from

Algorithm 6.2 Robust Simulated Annealing with Generalized Simulated Annealing

function RSA($\mathbf{R}_0$)
  $T(0) \leftarrow$ initial temperature, $t \leftarrow 0$, $\mathbf{R} \leftarrow \mathbf{R}_0$
  Construct worst-case set $\mathcal{M}(\mathbf{R})$ using $M+1$ local searches
  Calculate $g_{\mathrm{w}}(\mathbf{R}, T(0))$ using (6.11)
  $g_{\mathrm{w}}^* \leftarrow g_{\mathrm{w}}(\mathbf{R}, T(0))$, $\mathbf{R}^* \leftarrow \mathbf{R}$
  repeat
    Calculate temperature $T(t)$ according to (6.12)
    if $T(t) < T_{\min}$ **then**
      Re-anneal, $t \leftarrow 0$
      continue
    end if
    for $j \in 1, \ldots, 2M$ **do**
      Generate trial point $\mathbf{R}'$ from distorted Cauchy-Lorentz distribution
      Construct worst-case set $\mathcal{M}(\mathbf{R}')$ using $M+1$ local searches
      Calculate $g_{\mathrm{w}}(\mathbf{R}', T(t))$ using (6.11)
      Acceptance probability $P(\mathbf{R} \to \mathbf{R}')$ is calculated with (6.13)
      $p \leftarrow$ random number in $[0, 1]$
      if $p \leq P(\mathbf{R} \to \mathbf{R}')$ **then**
        $\mathbf{R}'$ is accepted, $\mathbf{R} \leftarrow \mathbf{R}'$
        if $g_{\mathrm{w}}(\mathbf{R}, T(t)) < g_{\mathrm{w}}^*$ **then**
          $g_{\mathrm{w}}^* \leftarrow g_{\mathrm{w}}(\mathbf{R}, T(t))$, $\mathbf{R}^* \leftarrow \mathbf{R}$
        end if
      end if
    end for
    $t \leftarrow t + 1$
  until maximum iterations or f evaluations are exceeded
  return $\mathbf{R}^*$, g_{w}^*
end function

random points where the number of searches is a tunable parameter which depends on the properties of f. If at any point during this local search we encounter a point where $f > \tau$, we abandon the local search as $f_{\mathrm{w}}(\mathbf{R}_{\mathrm{c}})$ is surely greater than τ. Otherwise, we have $f_{\mathrm{w}}(\mathbf{R}_{\mathrm{c}}) < \tau$, and a new robust minimum is found. Note that the search for the next hypercube will be stricter as τ has decreased and H_τ now contains more points, both ones from the current iteration as well as from previous iterations. The optimization process continues until either the side length of the maximal hypercube is less than $2\Delta_{\max}$ or the prescribed maximum number of function evaluations is exceeded. At this point, we return the robust minimum value τ and the point $\mathbf{R}^*$ at which it was achieved.

In our implementation, the search for the largest hypercube begins by constructing a k-d tree [34] T_τ which contains all of the points in H_τ. Then, we can frame this search as the maximization of the hypercube radius objective

$$r_{\mathrm{LEH}}(\mathbf{R}, T_\tau) = \min\left(\min_i(R_{\max} - R_i), \min_i(R_i - R_{\min}), \|\mathbf{R} - \mathrm{NN}(\mathbf{R}, T_\tau)\|_\infty\right), \tag{6.15}$$

where $\mathrm{NN}(\mathbf{R}, T_\tau)$ is the nearest neighbor of $\mathbf{R}$ in T_τ in the maximum metric sense. The use of radius, i.e. half of the side length, is for notational consistency with the original hypersphere approach. Thanks to the k-d tree representation of H_τ, which allows a fast nearest neighbor search, r_{LEH} can be computed efficiently. An evolutionary algorithm (DXNES [35]) with a population of 100 first finds the point $\mathbf{R}_\mathrm{c}$ which maximizes the radius $r^* = r_{\mathrm{LEH}}(\mathbf{R}_\mathrm{c}, T_\tau)$ within a predetermined amount of time t_{LEH}. Then, the same search is run over in the reduced domain $[R_{\min} + r^*, R_{\max} - r^*]^M$ as a refining step for $t_{\mathrm{LEH}}/2$. In our simulations, the search with refinement was far more capable on average than a single optimization with a time budget of $1.5t_{\mathrm{LEH}}$. Thus the nominal M-dimensional optimization problem is transformed into a two-step process: searching for an area without any known high cost points and an inner maximizer. Pseudocode for the LEH approach can be found in [25], and a description of our largest empty hypercube search is presented in Algorithm 6.3.

Algorithm 6.3 Finding largest empty hypercube

1: **function** FIND_LEH($H_\tau, \Delta_{\max}, R_{\min}, R_{\max}, t_{\mathrm{LEH}}$)
2: $\quad T_\tau \leftarrow \mathrm{KDTREE}(H_\tau)$
3: $\quad \mathbf{R}_\mathrm{c} \leftarrow \arg\max_{\mathbf{R}} r_{\mathrm{LEH}}(\mathbf{R}, T_\tau)$
$\qquad$ s.t. $R_{\min} + \Delta_{\max} \leq \mathbf{R} \leq R_{\max} - \Delta_{\max}$ ▷ In t_{LEH}
4: $\quad \mathbf{R}_\mathrm{c} \leftarrow \arg\max_{\mathbf{R}} r_{\mathrm{LEH}}(\mathbf{R}, T_\tau)$
$\qquad$ s.t. $R_{\min} + r_{\mathrm{LEH}}(\mathbf{R}_\mathrm{c}, T_\tau) \leq \mathbf{R} \leq R_{\max} - r_{\mathrm{LEH}}(\mathbf{R}_\mathrm{c}, T_\tau)$ ▷ In $t_{\mathrm{LEH}}/2$
5: $\quad$ **return** $\mathbf{R}_\mathrm{c}$
6: **end function**

This approach has two obvious run-time advantages over nested robust optimization approaches. First, we avoid a problem common to nested min-max approaches where overlapping $\Delta_{\max}$-neighborhoods lead to unnecessary and expensive computations. Second, we abandon computation of f_w at $\mathbf{R}_\mathrm{c}$ when we know it is not the robust minimum. In fact, in our simulations, most iterations involve only a small number of function evaluations before a candidate point is abandoned. However, the majority of the run time is spent finding the largest hypercube, which is long enough to limit the number of iterations we can reasonably perform. This would not be the limiting factor with objective functions more expensive than the ones considered here. Our implementation diverges from the one in [25] in that we consider hypercubes rather than hyperspheres, as they allow independent perturbations and are thus more relevant to our problem, and we employ the k-d tree approach to accelerate the largest hypercube calculation.

6.4 Numerical results and discussion

In this section, we apply the RSA and LEH algorithms to a photonic crystal structure, in order to achieve robustly optimized structures with ALT. We begin by analyzing these algorithms with the two-dimensional problem presented in Fig. 6.1(a) in order to provide some intuition on robust optimization of inclusion radii. This problem consists of two dielectric rods with radii R_1 and R_2 that are distanced λ with refractive index $n = 2.25$. The incident field is an x-traveling transverse magnetic plane wave, and we wish to maximize

the x-directed power flow P through the dotted line stretching from $(2\lambda, -0.5\lambda)$ to $(2\lambda, 0.5\lambda)$, considering each rod may have a radius error of up to $\pm 0.02\lambda$. For this problem, we define the nominal objective $f_1 = 1.25 - P/P_0$, whose contours are depicted in Fig. 6.1(c). In Fig. 6.1(d–e), we see the contours of the robust objective $f_{1,\mathrm{w}}$, which are generated by calculating the worst-case objective around every point on a fine grid. The contours of the robust plot are noticeably deformed, with local minima contracting or disappearing altogether. In particular, the global minimum for the nominal objective, located at $(0.21, 0.21)$, is not the global minimum of the robust problem as it is closely surrounded by points with worse performance, but it remains a *local* minimum of $f_{1,\mathrm{w}}$. The global minimum of the robust objective is located at $(0.229, 0.091)$ with a value of 0.0709.

Fig. 6.1(b) illustrates the nominal function for this problem around $(0.348, 0.216)$, as well as the $\Delta_{\max}$-neighborhood surrounding that point. This point is given as an example where the worst-case search of the RSA method will fail, as its predetermined searches cannot reach the upper-right corner of the neighborhood where f_1 is maximal. To be precise, this issue can arise when a local minimum of some objective f lies between the sampled point $\mathbf{R}$ and the worst case perturbation around it, causing an underestimation of f_{w}. We will revisit this issue and its consequences in further detail in Section 6.4.4.

We ran the RSA algorithm 50 times on this two-dimensional problem, with 100 iterations in each run. The mean robust minimum $f_{1,\mathrm{w}}$ attained by this algorithm was 0.0832, with runs split into those where the algorithm reached the neighborhood of the correct robust minimum, and those where it settled on a minimum of the nominal objective. Two sample runs of the RSA method are shown in Fig. 6.1(d), where only points accepted by the algorithm are shown. One of the runs, plotted in blue, passes in close proximity to the robust minimum before converging to an inferior point. Since many of the failed runs are at least partially due to the underestimation problem, with 13 runs underestimating the attained robust minimum by 5 % or more, we ran the LEH algorithm on the same problem with an increased maximum number of 9 local searches in each iteration, while restricting the run time to that of RSA. Here, the mean objective was 0.077 and the mean value of r_{LEH} in the final iteration of each run was $1.3\Delta_{\max}$, indicating the algorithm was usually close to convergence. The accepted points of two LEH runs are presented in Fig. 6.1(e), where one of the runs (in blue) is less successful as it stays away from its last accepted point, which is near the robust minimum.

Now that we have established some familiarity with RSA and LEH, we move on to setting up the main problem solved in this paper. The proposed geometry of our initial ALT structure consists of $M = 53$ round silicon rods with refractive index $n = 3.48$, placed on a triangular lattice with lattice constant $a = 600\,\mathrm{nm}$. The perturbation limit $\Delta_{\max}$ is set to 3 nm, or approximately 1.1 % of $R_{\max}$. The operating wavelength is $\lambda = 1.5\,\mu\mathrm{m}$, which was chosen in conjunction with a in order to allow for a wide bandgap. Previous results already confirmed this layout is capable of producing significant ALT [11]. We imposed horizontal symmetry on the inclusion radii and their perturbations in order to allow for timely calculations, which yields an effective $M = 28$. On the one hand, this means that we do not cover the whole space of detrimental perturbations; on the other hand, the asymmetric design space potentially contains better-performing devices. Thus we believe that the trade-off between coverage and run time is reasonable.

The structure which serves as a starting point along with the lines through which we

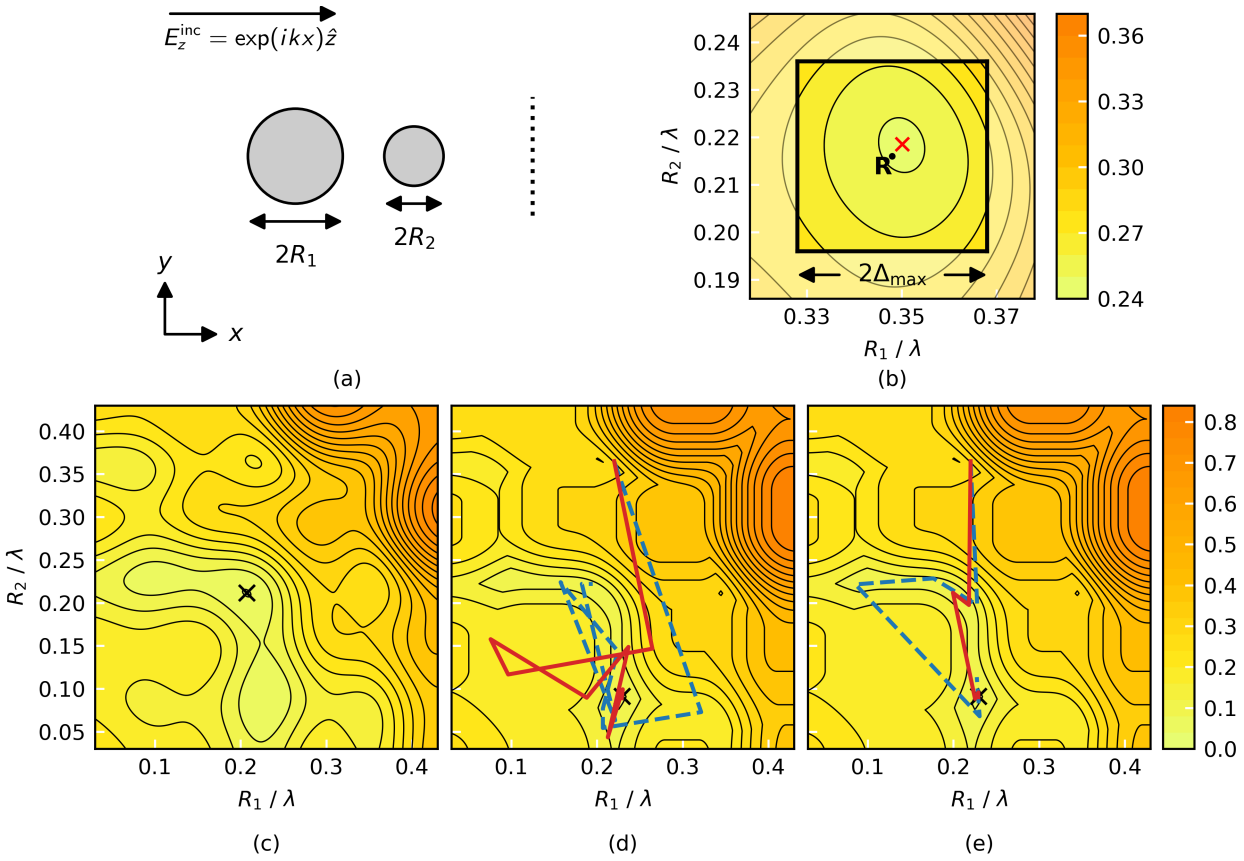

Fig. 6.1: Two-dimensional robust optimization problem, where power from a plane wave propagating through a line is maximized by optimizing the radii of two rods. (a) Geometry of the problem. (b) Contour plot of f_1 around $\mathbf{R} = (0.348, 0.216)$, where the box encloses the area searched for the worst-case perturbation, $f_{1,\text{w}}(\mathbf{R})$. Red cross denotes local minimum. (c) Contour plot of f_1. (d-e) Contours of corresponding robust function $f_{1,\text{w}}$, with paths taken by RSA and LEH, respectively. Black crosses denote global minima.

calculate the power flow $P_{\rightarrow}$ and $P_{\leftarrow}$ are depicted in Fig. 6.2(e). $P_{\rightarrow}$ measures the power in the forward direction (i.e. the power through the right curve $\ell_{\rightarrow}$ from an incident plane wave propagating left-to-right), and $P_{\leftarrow}$ is the power propagating in the backward direction through $\ell_{\leftarrow}$. The objective we wish to robustly optimize to obtain ALT is given by

$$f = -c\frac{P_{\rightarrow}}{P_0} + (1-c)\frac{P_{\leftarrow}}{P_{\rightarrow}}, \tag{6.16}$$

which is a weighted sum of our two objectives – minimizing the ratio between $P_{\leftarrow}$ and $P_{\rightarrow}$ while also maximizing $P_{\rightarrow}$ outright. P_0 denotes the power flowing through the same curve in the absence of the structure, and the weighting factor is $c = 0.01$. Another possible choice for the objective function would be $P_{\leftarrow} - P_{\rightarrow}$ as in [10], but this produced worse results in our simulations. In what follows, the number of wave expansions $2P + 1$, as well as the

tolerance of the solver, were chosen for an error tolerance of 10^{-6}. All simulations were run on an Intel Xeon E7-8867 CPU with a nominal frequency of 2.5 GHz. Some portions of the optimization algorithms were computed in parallel – the neighborhood exploration of the RSA method was run on 28 cores such that each core computed a single gradient ascent in each iteration. Since the LEH neighborhood search is sequential, it was run on a single core, but the evolutionary algorithm search for the largest hypercube ran on 28 cores as well.

6.4.1 Sensitivity of non-robust structures

Before we apply RSA and LEH to the ALT structure, we show how striking the degradation in device behavior can be in the presence of small implementation errors. We first nominally minimize f in order to achieve a nominal optimum for the aforementioned geometry. Fig. 6.2(a–b) show the norm of the electric field in response to right- and left-propagating plane waves incident upon this optimal structure. Particularly, the structure has normalized transmission efficiencies $T_{\rightarrow} = 1.86$ and $T_{\leftarrow} = 6 \times 10^{-6}$, where we normalize T_i as P_i/P_0. We stress that the extent of the curve ℓ is smaller than the height of the structure in order to avoid edge effects from the infinite plane wave. Thus, the structure can focus incoming power, creating normalized efficiencies greater than unity. This issue can be circumvented by utilizing a spatially-limited source, such as Gaussian beams, or through mode matching [36], but these were not considered here for the sake of simplicity. In contrast, Fig. 6.2(c–d) show the electric field norm when the same plane waves are incident upon the worst-case perturbation of the nominally optimal structure. Although the radius differences between these two structures are too small to be perceptible in the figures, the desired ALT properties have completely disappeared. In fact, the perturbed structure exhibits weak ALT in the *opposite* direction, with $T_{\rightarrow} = 6.5 \times 10^{-3}$ and $T_{\leftarrow} = 8.1 \times 10^{-2}$.

Further insight into the ALT effect created by this structure under nominal conditions can be gleaned from Fig. 6.3, which shows the real part of the electric field for forward and backward illumination. This snapshot shows that the forward-propagating plane wave is converted to a higher mode roughly consisting of two diagonal waves at the output, while the backward wave does not propagate beyond the leftmost column due to a sequence of complex interactions with the rods.

6.4.2 Robust Simulated Annealing

Applying the RSA method to our structure results in one that is substantially more resistant to perturbations than the nominally optimized version. The optimization process consisted of 60 outer iterations (3360 total iterations) with a run time of 58 hours, 3361 computations of g_{w}, and approximately 7×10^6 computations of f and ∇f. Fig. 6.4 shows the electric field norm after plane-wave incidence to both the robust structure and its worst-case perturbation, similarly to Fig. 6.2. This robust structure has normalized transmission efficiencies $T_{\rightarrow} = 0.112$ and $T_{\leftarrow} = 1.5 \times 10^{-3}$ (i.e. a transmission ratio of 18.7 dB). In contrast to the nominally optimized structure, here the worst-case perturbation continues to show ALT with normalized transmissions $T_{\rightarrow} = 7.91 \times 10^{-2}$ and $T_{\leftarrow} = 2.77 \times 10^{-3}$ (i.e. a ratio of 14.6 dB). The so-called price of robustness is noticeable here, as this structure underperforms the nominally-optimized one absent any perturbations, particularly with

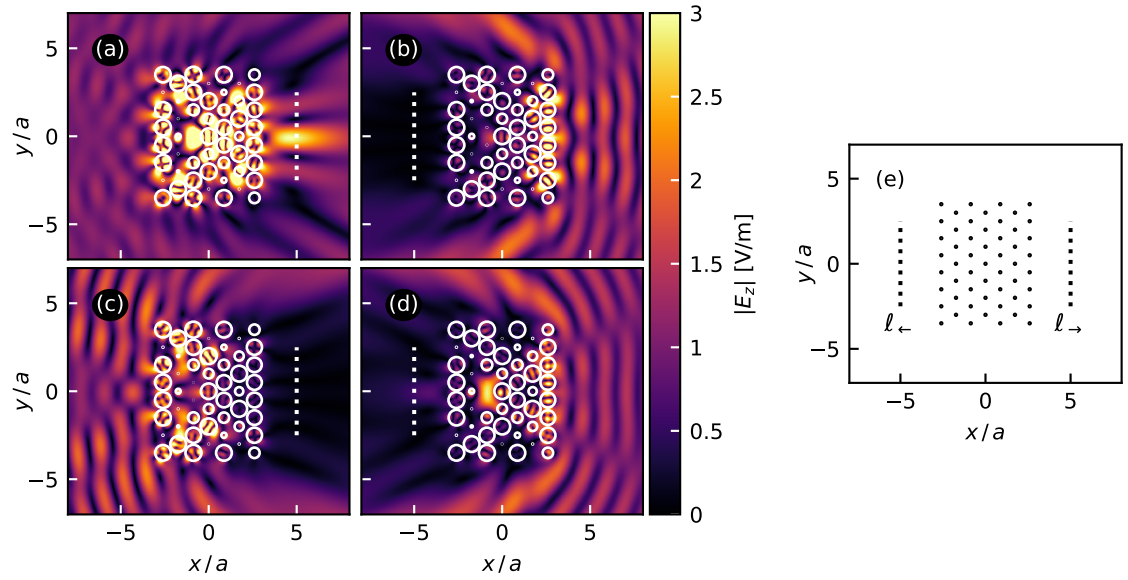

Fig. 6.2: ALT structure under consideration after optimizing radii for nominal performance with electric field norm after plane-wave incidence from both directions. (a) Forward propagation (→), (b) backward propagation (←), (c) → with worst-case perturbation of optimal structure, (d) ← with worst-case perturbation of optimal structure. (e) Structure before optimization process. Dotted lines indicate arcs through which the transmitted power was calculated.

respect to forward transmission, but far outperforms it in their presence. A detailed look at the convergence process is shown in Fig. 6.5, where we plot the value of g_{w} estimated by the algorithm in each accepted iteration. As the algorithm converges, it is less likely to accept points with significantly higher values of f_{w}. We also computed the actual value of f_{w} for each accepted point using 300 L-BFGS-B searches in the $\Delta_{\max}$-neighborhood, and found many accepted points where RSA substantially underestimated it. Since f_{w} is a lower bound on g_{w}, there are iterations where f_{w} is smaller as well.

6.4.3 Largest Empty Hypercube

We applied the LEH method to the same structure, while limiting the run time to 58 hours for a proper comparison to RSA, which resulted in approximately 37 500 iterations. This robust optimization procedure obtained the structure in Fig. 6.6, shown along with the electric field norm for both the robust structure and its worst-case perturbation. As with the RSA result, the optimized structure is robust to errors in the radii. This robust structure has normalized transmission efficiencies $T_{\rightarrow} = 8.67 \times 10^{-2}$ and $T_{\leftarrow} = 1.35 \times 10^{-3}$ (i.e. a transmission ratio of 18.1 dB). Also here, the worst-case perturbation continues to show ALT with normalized transmissions $T_{\rightarrow} = 7.39 \times 10^{-2}$ and $T_{\leftarrow} = 3.36 \times 10^{-3}$ (i.e. a ratio of 13.4 dB). We show the first 25 000 iterations of the LEH approach in Fig. 6.7, with the estimated value of f_{w} in each iteration as well as that verified with 300 L-BFGS-B searches in the $\Delta_{\max}$-neighborhood. The remaining iterations are omitted from the figure since LEH

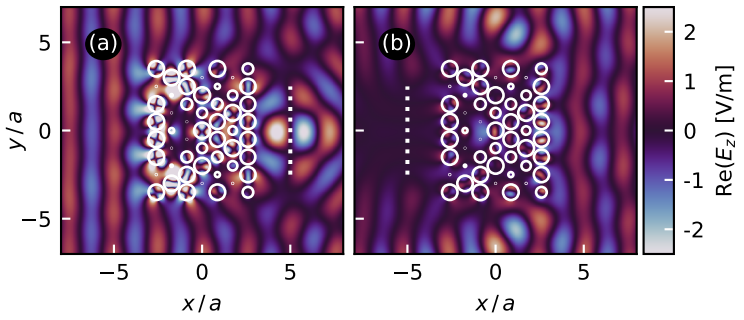

Fig. 6.3: $\mathrm{Re}(E_z)$ for the nominally-optimized structure under nominal conditions. (a) Forward illumination, (b) backward illumination.

failed to improve in them. Although the estimation process only utilized a maximum of 15 local searches, the neighborhood global maximum was found in all but one iteration, where it was inaccurate by 4.7 %. In addition, we show the side length of the largest empty hypercube found in each iteration. Since we limited the run time of each hypercube search to $1.5t_{\mathrm{LEH}} = 5\,\mathrm{s}$, it often failed to return the largest one, even though approximately 90 % of the total algorithm run time was spent on these searches. Extending this time further allowed the procedure to find the largest hypercube more often, but this did not appreciably improve f_{w}. However, reducing this time to the point where the largest hypercube was no longer found in most iterations did harm the optimization process.

6.4.4 Discussion

We now compare some of the results of the two robust optimization strategies. First, Fig. 6.8 illustrates the dependence of the normalized transmission efficiencies on the wavelength for both optimized structures, where frequency-dependent refractive index of the rods is that of silicon [37]. For RSA, surrounding our frequency of interest 1.5 µm, the worst-case perturbation shifts both transmission spectra backward by 25 nm while for LEH, they are shifted forward by 23 nm. Absent any perturbations, $T_{\rightarrow}$ is fairly wideband for both robustly optimized structures – with FWHM of 105 nm and 75 nm – in comparison to the 8 nm FWHM for the nominally-optimized structure in Fig. 6.2 (not depicted in Fig. 6.8). Therefore, it seems that the robustly-optimized structures also exhibit higher resilience to input wavelength error. We summarize the nominal and worst-case normalized transmission efficiencies calculated for each structure at $\lambda = 1.5\,\mu\mathrm{m}$ in Table 6.1.

Table 6.1: Normalized transmission efficiencies for each optimized structure

	Nominal optimization	RSA	LEH
Nominal, $\rightarrow$	1.86	1.12×10^{-1}	8.67×10^{-2}
Nominal, $\leftarrow$	6.04×10^{-6}	1.50×10^{-3}	1.35×10^{-3}
Worst case, $\rightarrow$	6.47×10^{-3}	7.91×10^{-2}	7.39×10^{-2}
Worst case, $\leftarrow$	8.14×10^{-2}	2.77×10^{-3}	3.36×10^{-3}

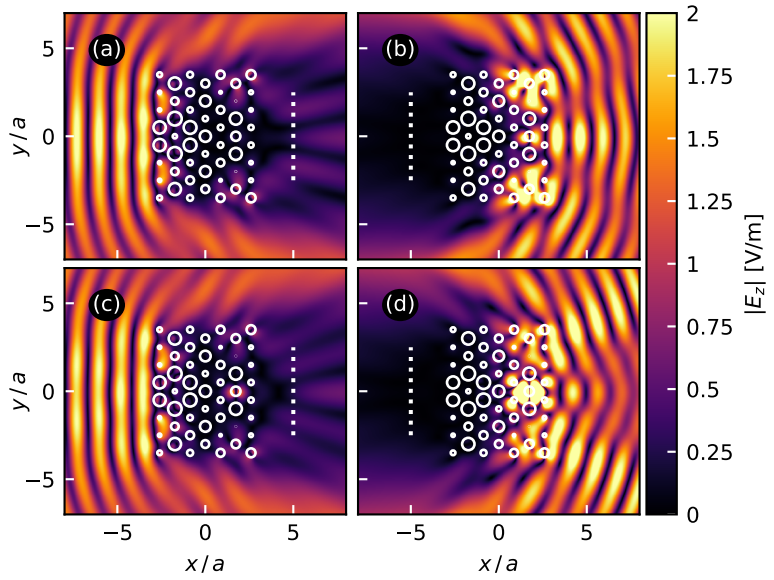

Fig. 6.4: ALT structure after robust optimization with the RSA approach, where the panels follow the template of Fig. 6.2(a–d).

We now revisit the underestimation issue alluded to in Section 6.3. Any robust optimization method that contains an inner loop that searches for the local worst case, such as the two considered here, can suffer from underestimating f_{w} (or g_{w}) in any given iteration. This issue is substantially more important than not finding the global optimum in a traditional optimization problem – once the worst-case perturbation is underestimated, the outer method may not only avoid robust minima but also "converge" to points that are not minima at all. We found the effect of this issue to be more pronounced on RSA, especially once the annealing temperature is low enough. The method may become trapped at a point where g_{w} is higher than estimated, since surrounding candidate points (when correctly estimated) are then perceived to have higher cost and thus avoided. On the other hand, once LEH calculates $\tau = f_{\mathrm{w}}$ at some point, it avoids all points with $f \geq \tau$. Thus even if f_{w} is underestimated, the algorithm will continue searching for an optimum in other regions of the domain. Of course, LEH might continue searching long after landing close to the robust optimum, instead of converging with successively smaller steps, as is common with global optimization methods. Therefore, the choice of method also depends how accurately f_{w} can be computed in reasonable time, which in turn depends on the number of maxima in any given $\Delta_{\max}$-neighborhood. It is worth noting that these local searches can fail even for very simple functions.

Nonetheless, it is clear from Figs. 6.5 and 6.7 that LEH was more accurate than RSA in finding the worst-case perturbation, even though it utilized fewer local searches, which merits a closer look. As mentioned earlier, one reason for this phenomenon is the starting point selection for the local searches in RSA. As an example, looking at iteration 155 (marked in Fig. 6.5 with a cross), none of the RSA local searches found a value of f over 13.2. Conversely, when we conducted 100 local searches from random starting points in

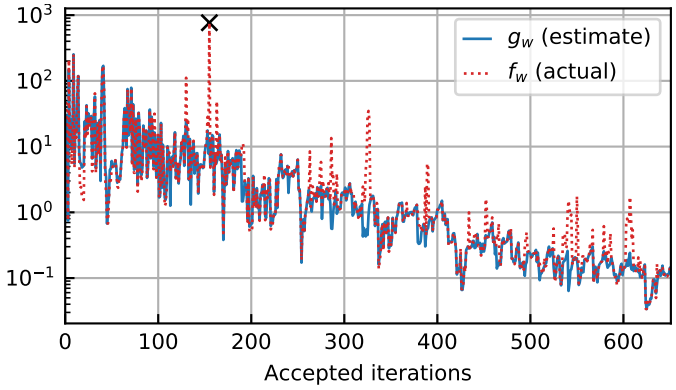

Fig. 6.5: Convergence process of RSA, showing the robust objective g_{w} and the actual worst case f_{w} surrounding each accepted point.

the $\Delta_{\max}$-neighborhood, in over half of them we found points whose values are an order of magnitude larger than 13.2. Another aspect of LEH which impacts this issue is the early abandonment of non-robust points. In a way, LEH has fewer opportunities to adversely underestimate f_{w}. As long as LEH does not underestimate the best point found so far (which is then assigned to τ), it is immaterial whether or how much other points are underestimated, so long as the local searches find any point in the neighborhood where $f > \tau$.

6.5 Conclusion

This work demonstrated the importance of robustness to implementation errors for photonic structures via a motivating example of asymmetric light transmission. We presented the robust optimization of this device using two conceptually different methods, obtaining structures which continued to exhibit asymmetric light transmission with worst-case errors. This work provided an overview of the benefits of each method, and discussed the circumstances in which they each shine. Namely, RSA was more susceptible to errors in the robust function, but was faster overall as long as f and g_{w} could be computed quickly and accurately; LEH is simpler to use as it does not require tuning beyond the number of local searches, and significantly reduces expensive f evaluations. Robust optimization is a powerful tool for preserving performance in the presence of fabrication variations, and can be applied to other devices based on aperiodic photonic crystals.

Bibliography

[1] C. Lu, X. Hu, H. Yang, and Q. Gong, "Ultrahigh-contrast and wideband nanoscale photonic crystal all-optical diode," *Optics Letters*, vol. 36, pp. 4668–4670, Dec. 2011.

[2] R. Philip, M. Anija, C. S. Yelleswarapu, and D. V. G. L. N. Rao, "Passive all-optical diode using asymmetric nonlinear absorption," *Applied Physics Letters*, vol. 91, no. 14, p. 141118, 2007.

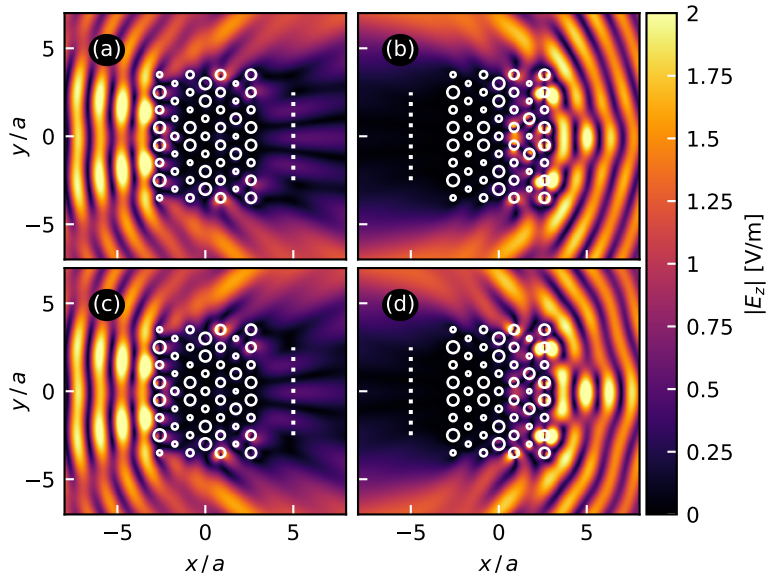

Fig. 6.6: ALT structure after robust optimization with the LEH approach, where the panels follow the template of Fig. 6.2(a–d).

[3] M. Vanwolleghem, X. Checoury, W. Śmigaj, B. Gralak, L. Magdenko, K. Postava, B. Dagens, P. Beauvillain, and J.-M. Lourtioz, "Unidirectional band gaps in uniformly magnetized two-dimensional magnetophotonic crystals," *Physical Review B*, vol. 80, p. 121102, Sept. 2009.

[4] M. Stolarek, D. Yavorskiy, R. Kotyński, C. J. Z. Rodríguez, J. Łusakowski, and T. Szoplik, "Asymmetric transmission of terahertz radiation through a double grating," *Optics Letters*, vol. 38, pp. 839–841, Mar. 2013.

[5] P. Xu, X. Lv, J. Chen, Y. Li, J. Qian, Z. Chen, J. Qi, Q. Sun, and J. Xu, "Dichroic optical diode transmission in two dislocated parallel metallic gratings," *Nanoscale Research Letters*, vol. 13, p. 392, Dec 2018.

[6] C. Menzel, C. Helgert, C. Rockstuhl, E.-B. Kley, A. Tünnermann, T. Pertsch, and F. Lederer, "Asymmetric transmission of linearly polarized light at optical metamaterials," *Physical Review Letters*, vol. 104, p. 253902, Jun 2010.

[7] Y. Xu, C. Gu, B. Hou, Y. Lai, J. Li, and H. Chen, "Broadband asymmetric waveguiding of light without polarization limitations," *Nature Communications*, vol. 4, no. 2561, 2013.

[8] Y. Zhang, Q. Kan, and G. P. Wang, "One-way optical transmission in silicon grating-photonic crystal structures," *Optics Letters*, vol. 39, pp. 4934–4937, Aug. 2014.

[9] D. Liu, S. Hu, and Y. Gao, "One-way optical transmission in silicon photonic crystal heterojunction with circular and square scatterers," *Physics Letters A*, vol. 381, no. 25, pp. 2131–2135, 2017.

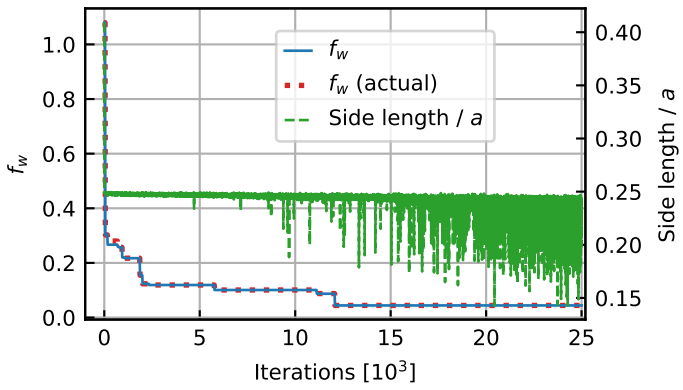

Fig. 6.7: Convergence process of LEH, showing the robust objective f_w and the side length of the largest empty hypercube for the first 25 000 iterations.

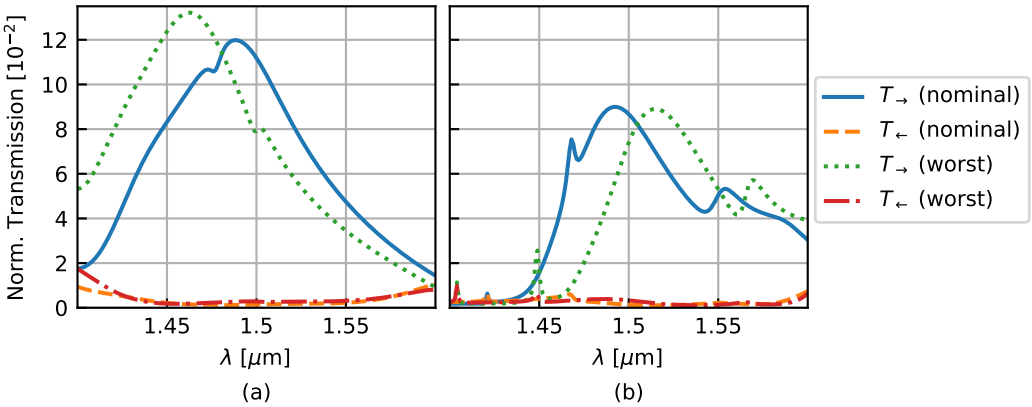

Fig. 6.8: Normalized transmission efficiencies vs. wavelength, in both directions and for both nominal and worst cases. (a) RSA-optimized structure, (b) LEH-optimized structure.

[10] E. Bor, M. Turduev, U. G. Yasa, H. Kurt, and K. Staliunas, "Asymmetric light transmission effect based on an evolutionary optimized semi-dirac cone dispersion photonic structure," *Physical Review B*, vol. 98, p. 245112, Dec. 2018.

[11] B. Blankrot and C. Heitzinger, "Design of aperiodic demultiplexers and optical diodes by optimizing photonic crystals," *OSA Continuum*, vol. 2, p. 2244, July 2019.

[12] Y.-C. Hsueh and K. J. Webb, "Electromagnetic field control with binary aperiodic nanostructures," *Journal of the Optical Society of America B*, vol. 34, pp. 2059–2071, Oct. 2017.

[13] A. Oskooi, A. Mutapcic, S. Noda, J. D. Joannopoulos, S. P. Boyd, and S. G. Johnson, "Robust optimization of adiabatic tapers for coupling to slow-light photonic-crystal waveguides," *Optics Express*, vol. 20, p. 21558, Sept. 2012.

[14] V. Gabrel, C. Murat, and A. Thiele, "Recent advances in robust optimization: An overview," *European Journal of Operational Research*, vol. 235, pp. 471–483, June 2014.

[15] J. Jung, "Robust design of plasmonic waveguide using gradient index and multiobjective optimization," *IEEE Photonics Technology Letters*, vol. 28, pp. 756–758, Apr. 2016.

[16] S. U. Rehman and M. Langelaar, "System robust optimization of ring resonator-based optical filters," *Journal of Lightwave Technology*, vol. 34, no. 15, pp. 3653–3660, 2016.

[17] F. Wang, J. S. Jensen, and O. Sigmund, "Robust topology optimization of photonic crystal waveguides with tailored dispersion properties," *Journal of the Optical Society of America B*, vol. 28, p. 387, Feb. 2011.

[18] N. Lebbe, C. Dapogny, E. Oudet, K. Hassan, and A. Gliere, "Robust shape and topology optimization of nanophotonic devices using the level set method," *Journal of Computational Physics*, vol. 395, pp. 710–746, Oct. 2019.

[19] E. W. Wang, D. Sell, T. Phan, and J. A. Fan, "Robust design of topology-optimized metasurfaces," *Optical Materials Express*, vol. 9, p. 469, Jan. 2019.

[20] H. Men, R. M. Freund, N. C. Nguyen, J. Saa-Seoane, and J. Peraire, "Fabrication-adaptive optimization with an application to photonic crystal design," *Operations Research*, vol. 62, pp. 418–434, Apr. 2014.

[21] H. Men, K. Y. K. Lee, R. M. Freund, J. Peraire, and S. G. Johnson, "Robust topology optimization of three-dimensional photonic-crystal band-gap structures," *Optics Express*, vol. 22, p. 22632, Sept. 2014.

[22] D. Bertsimas and O. Nohadani, "Robust optimization with simulated annealing," *Journal of Global Optimization*, vol. 48, no. 2, pp. 323–334, 2010.

[23] D. Bertsimas, O. Nohadani, and K. M. Teo, "Robust optimization for unconstrained simulation-based problems," *Operations Research*, vol. 58, no. 1, pp. 161–178, 2010.

[24] Y. Xiang, D. Sun, W. Fan, and X. Gong, "Generalized simulated annealing algorithm and its application to the Thomson model," *Physics Letters A*, vol. 233, no. 3, pp. 216–220, 1997.

[25] M. Hughes, M. Goerigk, and M. Wright, "A largest empty hypersphere metaheuristic for robust optimisation with implementation uncertainty," *Computers & Operations Research*, vol. 103, pp. 64–80, Mar. 2019.

[26] B. Blankrot and C. Heitzinger, "Efficient computational design and optimization of dielectric metamaterial structures," *IEEE Journal on Multiscale and Multiphysics Computational Techniques*, vol. 4, pp. 234–444, Oct. 2019.

[27] N. A. Gumerov and R. Duraiswami, "A scalar potential formulation and translation theory for the time-harmonic Maxwell equations," *Journal of Computational Physics*, vol. 225, pp. 206–236, July 2007.

[28] A. Z. Elsherbeni and A. A. Kishk, "Modeling of cylindrical objects by circular dielectric and conducting cylinders," *IEEE Transactions on Antennas and Propagation*, vol. 40, no. 1, pp. 96–99, 1992.

[29] D. Jalas, A. Petrov, M. Eich, W. Freude, S. Fan, Z. Yu, R. Baets, M. Popović, A. Melloni, J. D. Joannopoulos, M. Vanwolleghem, C. R. Doerr, and H. Renner, "What is — and what is not — an optical isolator," *Nature Photonics*, vol. 7, pp. 579–582, July 2013.

[30] A. Ben-Tal, D. Den Hertog, and J.-P. Vial, "Deriving robust counterparts of nonlinear uncertain inequalities," *Mathematical Programming*, vol. 149, no. 1–2, pp. 265–299, 2015.

[31] S. Leyffer, M. Menickelly, T. Munson, C. Vanaret, and S. M. Wild, "A survey of nonlinear robust optimization," *INFOR: Information Systems and Operational Research*, vol. 58, no. 2, pp. 342–373, 2020.

[32] S. G. Johnson, "Notes on adjoint methods for 18.335." `http://math.mit.edu/stevenj/18.336/adjoint.pdf`, 2012.

[33] R. H. Byrd, P. Lu, J. Nocedal, and C. Zhu, "A limited memory algorithm for bound constrained optimization," *SIAM Journal on Scientific Computing*, vol. 16, no. 5, pp. 1190–1208, 1995.

[34] J. L. Bentley, "Multidimensional binary search trees used for associative searching," *Communications of the ACM*, vol. 18, pp. 509–517, Sept. 1975.

[35] N. Fukushima, Y. Nagata, S. Kobayashi, and I. Ono, "Distance-weighted exponential natural evolution strategy and its performance evaluation," *Transaction of the Japanese Society for Evolutionary Computation*, vol. 4, no. 2, pp. 57–73, 2013.

[36] E. Moreno, D. Erni, and C. Hafner, "Modeling of discontinuities in photonic crystal waveguides with the multiple multipole method," *Physical Review E*, vol. 66, no. 3, p. 036618, 2002.

[37] H. H. Li, "Refractive index of silicon and germanium and its wavelength and temperature derivatives," *Journal of Physical and Chemical Reference Data*, vol. 9, no. 3, pp. 561–658, 1980.

Appendix

A.1 Discretization of the integral equations

Here we provide a detailed construction of the system matrix $\mathbf{Z}$ in (2.6), for which we must discretize the operators $\mathcal{S}$, $\mathcal{D}$, as well as their normal derivatives $\mathcal{N}$, $\mathcal{T}$. We note that $\mathcal{S}$ has a logarithmic singularity, $\mathcal{D}$, $\mathcal{N}$ are defined in the principal value sense, and $\mathcal{T}$ is hypersingular. We split each operator, using Kussmaul-Martensen quadrature for the singular portion and trapezoidal quadrature for the remainder, as prescribed in [1]. Let $\mathbf{x}(t) = (x_1(t), x_2(t))$, $t \in [0, 2\pi]$ denote the parametrization of the curve $\partial\Omega$ and $\hat{n}(t)$ be the outward-pointing normal at $\mathbf{x}(t)$. We lightly abuse prior notation and use $\mathbf{x}'$ to denote the derivative of $\mathbf{x}$, and $\mathbf{r}(t,\tau) = \mathbf{x}(t) - \mathbf{x}(\tau)$. We can write all four operators as

$$(\mathcal{S}^{(k)}\sigma)(\mathbf{x}(t)) = \int_0^{2\pi} \frac{i}{4} H_0^{(1)}(k|\mathbf{r}(t,\tau)|)|\mathbf{x}'(\tau)|\sigma(\tau)\,\mathrm{d}\tau, \tag{A.1a}$$

$$(\mathcal{D}^{(k)}\mu)(\mathbf{x}(t)) = \int_0^{2\pi} \frac{ik}{4} H_1^{(1)}(k|\mathbf{r}(t,\tau)|)\frac{\hat{n}(\tau)\cdot\mathbf{r}(t,\tau)}{|\mathbf{r}(t,\tau)|}\mu(\tau)\,\mathrm{d}\tau, \tag{A.1b}$$

$$(\mathcal{N}^{(k)}\sigma)(\mathbf{x}(t)) = \int_0^{2\pi} \frac{-ik}{4} H_1^{(1)}(k|\mathbf{r}(t,\tau)|)\frac{\hat{n}(t)\cdot\mathbf{r}(t,\tau)}{|\mathbf{x}'(t)||\mathbf{r}(t,\tau)|}|\mathbf{x}'(\tau)|\sigma(\tau)\,\mathrm{d}\tau, \tag{A.1c}$$

$$\begin{aligned}(\mathcal{T}^{(k)}\mu)(\mathbf{x}(t)) = \frac{1}{|\mathbf{x}'(t)|}\int_0^{2\pi} \Bigg[&\frac{1}{4\pi}\cot\left(\frac{t-\tau}{2}\right)\mu'(\tau) \\ &+ (P(k,t,\tau) - Q(k,t,\tau))\mu(\tau)\Bigg]\,\mathrm{d}\tau.\end{aligned} \tag{A.1d}$$

(A.1a) to (A.1c) are easily derived, while the derivation of (A.1d) is more involved, but can be found in [1]. We postpone the definitions of P and Q, and first split the kernel of the single-layer potential operator $\mathcal{S}$ as

$$\frac{i}{4}H_0^{(1)}(k|\mathbf{r}(t,\tau)|)|\mathbf{x}'(\tau)| = M_1(k,t,\tau)\log\left[4\sin^2\left(\frac{t-\tau}{2}\right)\right] + M_2(k,t,\tau), \tag{A.2}$$

where $M_1(k,t,\tau) = -\frac{1}{4\pi}J_0(k|\mathbf{r}(t,\tau)|)|\mathbf{x}'(\tau)|$. The functions M_1, M_2 are analytic with the diagonal terms

$$M_1(k,t,t) = -\frac{|\mathbf{x}'(t)|}{4\pi}, \quad M_2(k,t,t) = \left[\frac{i}{4} - \frac{\gamma}{2\pi} - \frac{1}{2\pi}\log\left(\frac{k}{2}|\mathbf{x}'(t)|\right)\right]|\mathbf{x}'(t)|. \tag{A.3}$$

Likewise, the kernel of $\mathcal{D}$ is split into two terms with analytic functions L_1, L_2, giving

$$L_1(k,t,\tau) = \frac{k}{4\pi}J_1(k|\mathbf{r}(t,\tau)|)\frac{\hat{n}(\tau)\cdot\mathbf{r}(t,\tau)}{|\mathbf{r}(t,\tau)|}, \tag{A.4a}$$

$$L_2(k,t,\tau) = \frac{ik}{4}H_1^{(1)}(k|\mathbf{r}(t,\tau)|)\frac{\hat{n}(\tau)\cdot\mathbf{r}(t,\tau)}{|\mathbf{r}(t,\tau)|} - L_1(k,t,\tau)\log\left[4\sin^2\left(\frac{t-\tau}{2}\right)\right] \tag{A.4b}$$

with the diagonal terms

$$L_1(k,t,t) = 0, \quad L_2(k,t,t) = \frac{1}{4\pi}\frac{x_1'(t)x_2''(t) - x_1''(t)x_2'(t)}{|\mathbf{x}'(t)|^2}. \tag{A.5}$$

Clearly, $\mathcal{N}$ can be split and computed similarly to $\mathcal{D}$ with small adjustments. Recall from (2.5) that we are interested in computing the operator differences. Ergo, any term that is independent from k vanishes and in particular, the cotangent term in $\mathcal{T}$ as well as some of the diagonal terms above.

It still remain to split P and Q from (A.1d), which are given by

$$P(k,t,\tau) = \frac{ik^2}{4}(\mathbf{x}'(t)\cdot\mathbf{x}'(\tau))H_0^{(1)}(k|\mathbf{r}(t,\tau)|), \tag{A.6a}$$

$$\begin{aligned} Q(k,t,\tau) =& \frac{i}{4}\tilde{Q}\Big[k^2 H_0^{(1)}(k|\mathbf{r}(t,\tau)|) - \frac{2kH_1^{(1)}(k|\mathbf{r}(t,\tau)|)}{|\mathbf{r}(t,\tau)|}\Big] \\ &+ (\mathbf{x}'(t)\cdot\mathbf{x}'(\tau))\frac{ikH_1^{(1)}(k|\mathbf{r}(t,\tau)|)}{4|\mathbf{r}(t,\tau)|} + \frac{1}{8\pi\sin^2(\frac{t-\tau}{2})}, \end{aligned} \tag{A.6b}$$

where P is split in the same fashion as the kernel of $\mathcal{S}$, up to a multiplicative term, and $\tilde{Q}$ is set as

$$\tilde{Q} = \frac{(\mathbf{x}'(t)\cdot\mathbf{r}(t,\tau))(\mathbf{x}'(t)\cdot\mathbf{r}(t,\tau))}{|\mathbf{r}(t,\tau)|^2}. \tag{A.7}$$

We can now split Q analogously to the previous functions,

$$\begin{aligned} Q_1(k,t,\tau) =& -\frac{1}{4\pi}\tilde{Q}\left[k^2 J_0(k|\mathbf{r}(t,\tau)|) - \frac{2kJ_1(k|\mathbf{r}(t,\tau)|)}{|\mathbf{r}(t,\tau)|}\right] \\ &- (\mathbf{x}'(t)\cdot\mathbf{x}'(\tau))\frac{kJ_1(k|\mathbf{r}(t,\tau)|)}{4\pi|\mathbf{r}(t,\tau)|}, \end{aligned} \tag{A.8a}$$

$$Q_2(k,t,\tau) = Q(k,t,\tau) - Q_1(k,t,\tau)\log[4\sin^2(\frac{t-\tau}{2})], \tag{A.8b}$$

thereby giving us the means to calculate the rest of the diagonal values. After dropping the terms which do not depend on k, we have

$$P_1(k,t,t) - Q_1(k,t,t) = -\frac{k^2|\mathbf{x}'(t)|^2}{8\pi}, \tag{A.9a}$$

$$P_2(k,t,t) - Q_2(k,t,t) = \frac{k^2|\mathbf{x}'(t)|^2}{8\pi}\left[\pi i + 1 - 2\gamma - 2\log(\frac{k}{2}|\mathbf{x}'(t)|)\right]. \tag{A.9b}$$

Finally, we discuss the quadrature of these operators using equidistant points $t_n = n\pi/N$. For the smooth operators M_2, L_2, P_2, Q_2, we use simple trapezoidal quadrature, i.e.,

$$\int_0^{2\pi} M_2(k,t,\tau)\sigma(\tau)\,\mathrm{d}\tau \approx \frac{\pi}{N}\sum_{n=0}^{2N-1} M_2(k,t,t_n)\sigma_n, \tag{A.10}$$

while the logarithmic terms use the same points but with weights

$$R_n(t) = -\frac{2\pi}{N}\sum_{m=1}^{N-1}\frac{\cos[m(t-t_n)]}{m} - \frac{\pi\cos[N(t-t_n)]}{N^2}. \tag{A.11}$$

Now that we can calculate approximations of all operators at any point on the curve, all entries of the system matrix $\mathbf{Z}$ are readily available. For example, using the relation $R_{|j-n|}(0) = R_n(t_j)$, the upper left block is computed with

$$\begin{aligned} S_{j,n}^{(k_0)} - S_{j,n}^{(k_1)} =& R_{|j-n|}(0)[M_1(k_0,t_j,t_n) - M_1(k_1,t_j,t_n)] \\ &+ \frac{\pi}{N}[M_2(k_0,t_j,t_n) - M_2(k_1,t_j,t_n)]. \end{aligned} \tag{A.12}$$

A.2 Current filament excitation

Here we explain how the scattering theory presented in Section 2.3.1 allows the expansion of incident fields created by current filaments of infinite length. Without loss of generality, assume a single inclusion centered at $\mathbf{o}$ and a current filament at $\mathbf{r}'$ with current I. The incident electric field [2] is thus given by

$$u^{\text{inc}}(\mathbf{r}) = -\frac{kI\eta}{4}H_0^{(1)}(k|\mathbf{r}-\mathbf{r}'|), \tag{A.13}$$

where η is the wave impedance, and we can expand the Hankel function with Graf's addition theorem, yielding

$$H_0^{(1)}(k|\mathbf{r}-\mathbf{r}'|) = \sum_{p=-\infty}^{\infty} H_p^{(1)}(k|\mathbf{o}-\mathbf{r}'|)J_p(k|\mathbf{r}-\mathbf{o}|)e^{ip[\angle(\mathbf{r}-\mathbf{o})-\angle(\mathbf{o}-\mathbf{r}')-\pi]}. \tag{A.14}$$

By equating this series with the incident field expansion in (2.8), we have an expression for the incoming coefficients of the inclusion,

$$\alpha_p = -\frac{k^2 I\eta}{4}H_p^{(1)}(k|\mathbf{o}-\mathbf{r}'|)e^{-ip[\angle(\mathbf{o}-\mathbf{r}')+\pi]}. \tag{A.15}$$

Bibliography

[1] R. Kress, "On the numerical solution of a hypersingular integral equation in scattering theory," *Journal of Computational and Applied Mathematics*, vol. 61, no. 3, pp. 345–360, 1995.

[2] R. F. Harrington, *Time-Harmonic Electromagnetic Fields*. New York, NY: McGraw-Hill, 1961.

Curriculum Vitae

Personal Data

Name	Boaz Blankrot
Email	`boaz.blankrot@tuwien.ac.at`
Webpage	`https://bblankrot.github.io`

Education

04/2016–09/2020 (expected)	**TU Wien, Vienna, Austria** Dr. techn. (Ph.D.) in Technical Mathematics, supervised by Prof. Clemens Heitzinger
10/2012–03/2016	**Technion—Israel Institute of Technology, Haifa, Israel** M.Sc. in Electrical Engineering, supervised by Prof. Yehuda Leviatan
10/2008–01/2013	**Technion—Israel Institute of Technology, Haifa, Israel** B.Sc. in Electrical Engineering (cum laude)

Publications (articles and peer-reviewed proceedings)

- B. Blankrot and C. Heitzinger, "On the robust optimization of photonic structures for asymmetric light transmission," *Submitted for publication*, Jul. 2020.
- B. Blankrot and C. Heitzinger, "Efficient Computational Design and Optimization of Dielectric Metamaterial Structures," *IEEE Journal on Multiscale and Multiphysics Computational Techniques*, vol. 4, pp. 234–244, Oct. 2019.
- B. Blankrot and C. Heitzinger, "Design of aperiodic demultiplexers and optical diodes by optimizing photonic crystals," *OSA Continuum*, vol. 2, no. 7, pp. 2244–2252, Jul. 2019.
- B. Blankrot and C. Heitzinger, "Automated Design of Photonic Crystal Demultiplexers," *Proc. of the 2018 12th International Congress on Artificial Materials for Novel Wave Phenomena (Metamaterials'2018)*, Espoo, Finland, 27–30 Aug. 2018, pp. 55–57.

- B. Blankrot and C. Heitzinger, "ParticleScattering: Solving and optimizing multiple-scattering problems in Julia," *Journal of Open Source Software*, vol. 3, no. 25, p. 691, May 2018.
- B. Blankrot and Y. Leviatan, "FMM-Accelerated Source-Model Technique for Many-Scatterer Problems," *IEEE Transactions on Antennas and Propagation*, vol. 65, no. 8, pp. 4379–4384, Aug. 2017.

Conference Presentations

- B. Blankrot and C. Heitzinger, "Efficiently optimizing inclusion rotation angle for maximal power flow," presented at the 14th International Conference on Mathematical and Numerical Aspects of Wave Propagation (WAVES), Vienna, Austria, Aug. 26–30, 2019.
- B. Blankrot and C. Heitzinger, "Optimization-centric Approach for Electromagnetic Scattering from Metamaterials," presented at the SIAM Annual Meeting, Portland, OR, USA, Jul. 9–13, 2018.
- B. Blankrot and C. Heitzinger, "Multiple scattering approach for dielectric metamaterial analysis," presented at the Austrian Numerical Analysis Day, Salzburg, Austria, May 4–5, 2017.
- B. Blankrot and C. Heitzinger, "Integral Equation Solver for Metamaterial Design," presented at the SIAM Conference on Computational Science and Engineering, Atlanta, GA, USA, Feb. 27–Mar. 3, 2017.